

Microwave Shielding Structures with Applications to Ground-Penetrating
Radar

by

David James Sawyer

A thesis submitted in partial fulfillment of the requirements for the degree of

Master of Science

in

Electromagnetics and Microwaves

Department of Electrical and Computer Engineering
University of Alberta

© David James Sawyer, 2018

Abstract

This thesis contains an overview and theory for a variety of antenna shielding structures, for the purpose of reducing interference and multipath issues due to the antenna's surrounding environment. Though such structures are relevant to a variety of applications, particular focus is given to ground-penetrating radar (GPR). For a GPR system, due to the high degree of loss an electromagnetic (EM) signal experiences as it travels underground, extraneous coupling due to multipath signals, such as those reflected from above-ground targets, can potentially overwhelm any measured signal of interest. Though this can be mitigated using metallic shields, any practical finite shield structure is going to suffer from diffraction effects, which cause additional back and sidelobes. Additionally, the shield itself will alter the antenna's time-domain response, which can affect GPR system performance. To solve these issues, this work considers radar absorbing materials, which can be used to prevent reflection and dampen currents on a metal surface. This work also considers a variety of metallic shields, such as ground planes, cavities, and high-impedance or electromagnetic bandgap (EBG) surfaces, and mechanisms which either cause or suppress diffraction on these structures. These structures are also studied in the time domain, to elucidate how these shields perturb an antenna's response

when excited by a broadband pulse. Generally, the excitation of surface waves is found to play a prominent role in diffraction around these shields, and the Sommerfeld half-space problem is considered as an analytical solution for the excitation of surface waves by a dipolar source. This solution can also readily be extended for dipoles above multilayer absorbing materials. Finally, this work presents the in-depth study of a choke ring shield, together with the fabrication and measurement of a choke ring shield loaded with an absorber to suppress ringing effects within the shield's central cavity. Some potential further designs based off the principles from this thesis are also presented.

Preface

This thesis includes contributions from two other publications. The first is titled “Investigation of choke-ring structures for ground-penetrating radar”, and is published in the *IEEE 2017 Antennas and Propagation Society and URSI USNC International Symposium Digest*, with the full reference as given in the bibliography [1]. This was a collaborative work between Sensors & Software and the University of Alberta. Some of the background material on time-domain signal issues for GPR systems as written in Chap. 1 was first published in this work. This work also introduces the relative forward power (RFP) metric, which is described in this thesis in Chap. 3. I am the primary author of this work in terms of design, concept, and writing, with additional guidance and expertise on GPR provided by our colleagues with Sensors & Software.

The second publication this thesis draws from is titled “Choke Rings for Pattern Shaping of a GPR Dipole Antenna” for publication in *IEEE Transactions on Antennas and Propagation*. This work describes the Kaiser pulse used in Chap. 3, one of the parametric studies described in Chap. 5, and makes up the large majority of Chap. 6. I am similarly the primary author of this work.

The work in this thesis has also influenced a third publication, “Miniaturization of a Folded Dipole Antenna for Narrowband Sensing Applications” for publication in *IEEE Transactions on Antennas and Propagation* (under review), though none of the material is reproduced in this thesis. My contribution in this work included balun layout and modeling, assistance with the measurement setup, as well as editing and organization of the paper.

Acknowledgments

This work was supported by the Natural Sciences and Engineering Research Council (NSERC) of Canada through a Collaborative Research and Development (CRD) grant with Sensors & Software, Inc. (Mississauga, Ontario, Canada). The authors would also like to acknowledge the simulation tools provided by CMC Microsystems and experimental facilities acquired through the support of the Canada Foundation for Innovation (CFI) and the Province of Alberta.

I would also like to thank my supervisor Dr. Ashwin Iyer for his hard work and help in editing this thesis. I would also like to thank my research colleagues, who have been very helpful in a variety of ways, including but not limited to the maintenance of lab equipment, assisting in measurement setups, proofreading publications, and helping with software issues. Finally, I would like to thank Dr. Peter Annan and Dr. Nectaria Diamanti for providing their expertise and guidance on practical issues related to GPR systems and antenna time-domain behaviour.

Contents

| | | |
|----------|---|-----------|
| 1 | Introduction | 1 |
| 1.1 | Ground-Penetrating Radar | 1 |
| 1.2 | Other Applications | 4 |
| 1.3 | Scope & Organization | 4 |
| 1.4 | Simulation Details | 5 |
| 2 | Absorbers | 6 |
| 2.1 | Salisbury Screen | 7 |
| 2.2 | Jaumann Absorber | 8 |
| 2.3 | High-Impedance Surface Absorbers | 10 |
| 2.4 | Dielectric Absorbers | 12 |
| 2.5 | Ferrite & Magnetic Absorbers | 13 |
| 2.6 | Metamaterial Absorbers | 14 |
| 2.7 | Thickness-Bandwidth Limitations | 15 |
| 3 | Ground-Plane Shields | 18 |
| 3.1 | Finite Ground Planes | 18 |
| 3.1.1 | Diffraction Effects | 19 |
| 3.1.2 | Small Ground Planes | 20 |
| 3.1.3 | Cavities | 21 |
| 3.1.4 | Electromagnetic Band-Gap Structures | 22 |
| 3.2 | Diffraction Formulations | 23 |

| | | |
|----------|---|-----------|
| 3.2.1 | Scattering Solutions | 23 |
| 3.2.2 | Edge Diffraction | 25 |
| 3.3 | Shielded Dipole | 27 |
| 3.3.1 | Disc | 27 |
| 3.3.2 | Cavity | 30 |
| 4 | Surface Waves and Impedance Surfaces | 37 |
| 4.1 | Surface Wave Solutions | 38 |
| 4.1.1 | Field Components | 40 |
| 4.1.2 | PEC and PMC Surfaces | 42 |
| 4.2 | Corrugated Surface | 42 |
| 4.2.1 | Dispersion Diagram | 43 |
| 4.2.2 | Soft Surface Property | 44 |
| 4.3 | Dipole Above an Impedance Surface | 46 |
| 4.3.1 | Vertical Dipole | 46 |
| 4.3.2 | Horizontal Dipole | 49 |
| 5 | Choke Ring Simulation and Analysis | 52 |
| 5.1 | Choke Ring Design | 53 |
| 5.1.1 | Coaxial Modes | 54 |
| 5.2 | Cavity Absorber | 55 |
| 5.3 | Parametric Studies | 56 |
| 5.3.1 | Number of Rings | 57 |
| 5.3.2 | Total Size | 58 |
| 5.3.3 | Corrugation Width | 59 |
| 6 | Choke-Ring Shield for GPR | 61 |
| 6.1 | Design | 62 |
| 6.1.1 | Choke Rings | 62 |
| 6.1.2 | Small Dipole Antenna | 62 |

| | | |
|----------|---|-----------|
| 6.1.3 | Absorber | 63 |
| 6.2 | Simulation & Analysis | 63 |
| 6.3 | Fabrication | 69 |
| 6.4 | Measurement | 72 |
| 6.5 | Results | 73 |
| 7 | Conclusion | 76 |
| 7.1 | Summary | 76 |
| 7.2 | Future Work | 80 |
| 7.2.1 | Multiple Disc Reflectors | 81 |
| 7.2.2 | Anisotropic Resistive Ground Planes | 83 |
| 7.2.3 | Absorber-Loaded Choke Rings | 84 |
| A | Signal Processing & Time-Domain Properties | 85 |
| A.1 | Antenna Transfer Function Approach | 85 |
| A.2 | Short Dipole | 87 |
| A.2.1 | Ground-Plane-Backed Dipole | 87 |
| A.3 | Pulse Characteristics | 88 |
| A.3.1 | Gaussian Pulse | 88 |
| A.3.2 | Hilbert Transform | 89 |
| A.3.3 | Windowed Pulses | 89 |
| | Bibliography | 93 |

List of Tables

- 3.1 Comparison of calculated resonant frequencies and frequencies for observed (simulated) resonant dips in RFP, for the two lowest order waveguide modes in the cavity. 34

- 6.1 Conductivity and permittivity values for each of the layers in the absorber simulation model. Each layer is 2 cm thick. 65

List of Figures

| | | |
|-----|---|----|
| 1.1 | How GPR images are generated by the above-ground scanning of a GPR system [2]. | 3 |
| 2.1 | Geometry of the classic Salisbury screen, which achieves absorption by spacing the resistive sheet a resonant length away from the backing metallic plane. | 7 |
| 2.2 | Example of a three-layer Jaumann absorber, which uses multiple resistive sheets spaced at lengths that are approximately resonant. | 9 |
| 2.3 | The Sievenpiper high-impedance surface [3]. | 10 |
| 3.1 | Normalized scattering cross section of a disc versus its electrical size [4]. Disc radius is given by a , wave number by k , and scattering cross section by σ . Comparison to GTD and Rayleigh scattering is shown. | 24 |
| 3.2 | Field magnitudes for plane waves incident at 30° from the z axis, diffracted by a PEC half plane. The two perpendicular field polarizations are shown [5]. | 26 |
| 3.3 | Front-to-back ratio for a horizontal dipole spaced 4 cm above a disc of radius 11.72 cm. | 28 |
| 3.4 | Radiated pulse amplitude for a dipole above a circular ground plane with parametrically varied radius. | 29 |
| 3.5 | Normalized radiated pulse envelope for a dipole above a circular ground plane with a parametrically varied radius. | 30 |

| | | |
|------|--|----|
| 3.6 | Maximum amplitude of the radiated pulse envelope as a function of ground plane radius, for a dipole above the ground plane. | 31 |
| 3.7 | Transverse electric fields of the two lowest-order cylindrical waveguide modes, given a symmetrical excitation. | 32 |
| 3.8 | RFP vs frequency for different cavity depths. | 33 |
| 3.9 | Radiated pulse for a cavity excited by a lossy dipole, and the Gaussian window that is used to find the spectrum of the pulse's ringing. | 35 |
| 3.10 | Frequency spectrum of the cavity's ringing. | 36 |
| 4.1 | Fields of the TM and TE surface waves. | 39 |
| 4.2 | Corrugated surface, where d is the corrugation height, g the corrugation width, and t the metallic thickness. Directions of propagation for TM and TE surface waves are marked. | 43 |
| 4.3 | Dispersion diagram of the corrugated surface with depth of 7.5 cm, with a period of 3 cm. | 45 |
| 4.4 | Electric field magnitudes for an infinitesimal dipole above various surfaces. The dipole is $\lambda/10$ above the surface in each case. For the capacitive, inductive, and resistive surfaces, a surface impedance of magnitude $377\ \Omega$ was used. | 50 |
| 5.1 | Cross-section of a typical choke-ring structure backing a printed dipole antenna, where d is the choke-ring height, g the corrugation width, t the ring thickness, a the cavity radius, and b the total radius. | 53 |
| 5.2 | Cross sections of the cylindrical cavity and choke-ring structures, where λ is the free-space wavelength at the $\lambda/4$ design frequency [1]. | 56 |
| 5.3 | RFP for different numbers of choke rings. | 57 |

| | | |
|-----|---|----|
| 5.4 | RFP versus radial size, for the different choke or cavity shields with or without absorber | 59 |
| 5.5 | Normalized E- and H-plane patterns of the choke ring with absorber at 1.4 GHz, for various filling factors. | 60 |
| 6.1 | Exciting Kaiser pulse and simulated far-field radiated response of the cavity-backed antenna, with and without the absorber. The two radiated pulses use the same normalization factor such that amplitudes can be meaningfully compared. | 65 |
| 6.2 | Measured vs. simulated RFP, comparing the simple cavity to choke-ring shields, with and without the absorber. | 66 |
| 6.3 | Normalized measured and simulated averaged E- and H-plane patterns of cavity and choke structures for a Kaiser exciting pulse, as determined by (6.2). | 67 |
| 6.4 | Normalized measured and simulated pulse shapes (left) and their envelopes (right). | 70 |
| 6.5 | The fabricated cavity shield with the antenna inside, and the outer ring used to convert it into a choke-ring shield. | 71 |
| 6.6 | The fabricated antenna, consisting of a resistively loaded strip dipole, balun, feed network and MMCX connector. | 71 |
| 6.7 | The choke-ring antenna mounted in the anechoic chamber. | 72 |
| 6.8 | Measured S_{11} of the dipole backed by the different cavity/choke shields, compared to the unshielded dipole. | 74 |
| 7.1 | Horizontal choke structure. The symmetry plane is marked as the dashed line. | 81 |
| 7.2 | Front-to-back ratio of a single disc versus the two-disc choke design. | 81 |

| | | |
|-----|--|----|
| 7.3 | Front-to-back ratio at 0.75 GHz as the radii of the two discs backing a dipole are varied. Radius1 is for the disc closer to the dipole. | 82 |
| 7.4 | Depiction of an anisotropic resistive surface inspired by the soft-surface principle used in choke ring designs. | 83 |
| A.1 | Block model for different components in an antenna system, with transfer functions labeled [6]. | 86 |
| A.2 | Different representations of the normalized Kaiser pulse, based on the a Kaiser window in the frequency domain between 0.75 GHz and 2.5 GHz. | 91 |

List of Abbreviations

| | |
|-----|-----------------------------------|
| GPR | Ground-Penetrating Radar |
| EM | ElectroMagnetic |
| RF | Radio Frequency |
| EBG | Electromagnetic Band-Gap |
| Tx | Transmit |
| Rx | Receive |
| GPS | Global Positioning System |
| FSS | Frequency Selective Surface |
| GTD | Geometrical Theory of Diffraction |
| UTD | Uniform Theory of Diffraction |
| RFP | Relative Forward Power |
| TM | Transverse Magnetic |
| TE | Transverse Electric |
| TEM | Transverse ElectroMagnetic |
| PEC | Perfect Electric Conductor |
| PMC | Perfect Magnetic Conductor |
| PML | Perfectly Matched Layer |
| VNA | Vector Network Analyzer |

Chapter 1

Introduction

The long-standing interest in microwave or radio frequency (RF) research can ultimately be attributed to the value of wireless technologies that are possible at these frequencies. The term microwave frequency is somewhat vaguely defined, but typically includes frequencies from around single-digit gigahertz frequencies up to tens of gigahertz, while lower frequencies from tens to hundreds of megahertz are usually considered RF. Though this thesis is titled “Microwave Shielding Structures with Applications to Ground-Penetrating Radar”, devices can generally be scaled to any frequency range desired, and this work applies to both frequency ranges.

1.1 Ground-Penetrating Radar

Though this work is applicable to a variety of communications or radar applications, special attention is paid to ground-penetrating radar (GPR). Though some systems use frequency modulation, most GPR systems operate in the time domain, using short electromagnetic (EM) pulses to image underground objects. Due to material mismatch between an object and the surrounding medium, a buried object will reflect incident radiation. By measuring the resulting time delay, the object’s depth underground can be inferred. This has

a variety of academic and commercial applications; for example, it is widely used to study geological features including bedrock depth, soil composition, ice-sheet thickness, and ground water levels, with applications towards environmental studies, geophysics, construction, and natural resource exploration.

GPR systems usually use a bistatic setup, with transmit (Tx) and receive (Rx) antennas a fixed distance from each other. To create an image, GPR systems are scanned along the ground surface. As the GPR system's above-ground position varies, the distance from the underground object of interest will vary. Thus, the time-delay of the reflected pulse will vary, and the underground object's "apparent" depth will vary. The scanning of the GPR system over position creates an apparent depth that varies as a function of position, resulting in a hyperbolic arc for each underground reflecting object. An example of this is shown in Fig. 1.1. Since each arc can be related to a single reflecting target, the arc's apex reveals the target's overall depth. The shape of the arc is determined by the speed of light underground, which is used to infer the target's depth from the time delay of the reflected signal.

Though GPR is considered a fairly mature technology, it faces considerable technological difficulty. For accurate resolution, GPR systems need extremely large bandwidths, which can range from 2–3 octaves, up to even a decade of bandwidth. Due to the loss characteristics of common ground materials such as clay or soil, and the effect of moisture on these loss characteristics, the upper operating frequencies of GPR systems are limited [7]. Operating frequencies range from as low as 10 MHz, up to roughly 2 or 3 GHz. Since a GPR system is scanned over the measurement area, system size and weight is a major constraint, especially for systems operating at lower frequencies.

Due to the high degree of attenuation experienced by signals propagating underground (as an example, wet clay has an attenuation as high as 100 dB/m [8]), signals reflected from an underground target can be easily overwhelmed by other stray signals, such as those coupled directly from Tx to Rx antennas, ex-

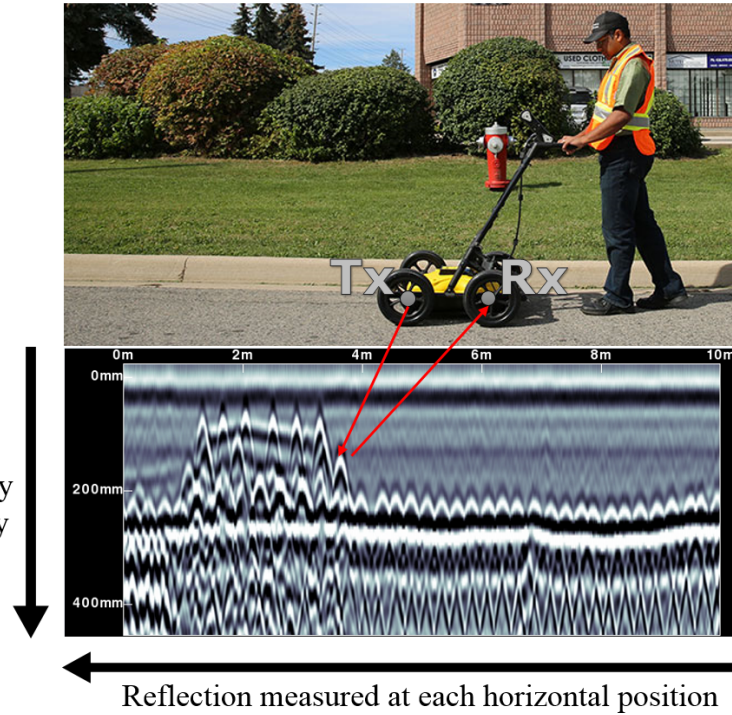


Figure 1.1: How GPR images are generated by the above-ground scanning of a GPR system [2].

ternal interference noise, or reflected from above-ground obstacles. Multipath signals reflected from unwanted targets are specifically referred to as clutter. Since noise can often be averaged out of a measurement, clutter signals are the major limiting factor in a GPR system measurement. Other late-time signals, such as due to resonant ringing phenomena, are similarly detrimental to a GPR system. Late-time ringing—also known as ringdown in the context of GPR—is especially problematic, in that if the rate of decay of the ringing is less than the rate of decay of signals as they propagate underground, then the ringing will generally obscure all underground signals below some particular depth, depending on the amplitude of the ringing [9].

To avoid clutter and above-ground interference, GPR antennas generally need to be designed to limit radiation to a single radiating hemisphere. Though high-gain antennas with high front-to-back ratios seem to fit this constraint,

such antennas are unsuitable for GPR due to limited beamwidths, which may not be able to measure over sufficient angles required to generate the hyperbolic arc shapes necessary to identify an underground target. Additionally, high-gain antennas are often large, and may be limited in terms of wide-band pulse characteristics. Rather, simple dipole antennas, with some variety of shielding are much more common, with the most common shielding being some variety of cavity [10, 11]. Cavities however, have been known to introduce late-time ringing into the antenna system [9]. As a result, there has also been some interest in absorbing materials to try and limit the impact of the cavity on the time-domain response of the antenna [1, 12].

1.2 Other Applications

This thesis generally considers microwave structures used to shield and reduce interaction between antennas and their external environment. Beyond GPR, the results are useful to a much wider set of applications. For example, many ground antennas for satellite communications have similar requirements for antenna patterns as GPR, with wide hemispherical coverage, but isolated to a single hemisphere of radiation [13, 14]. Similarly, many of the same structures used to reduce coupling in antenna arrays are similarly applicable to the reduction in coupling between Tx and Rx GPR antennas.

1.3 Scope & Organization

Chap. 2 and 3 both look at the state of the art of shielding structures, and contain a large review of the literature. Chap. 2 in particular looks at microwave absorbing materials, with attention paid to trade offs in thickness and bandwidth, while Chap. 3 considers finite ground plane and related structures, such as cavities and electromagnetic band-gap (EBG) surfaces, with a focus on

diffraction effects for finite shields. Chap. 4 looks at surface wave solutions, and how surface waves are excited by dipoles, dependent on the polarization of the dipole fields. This also includes an exact solution method for dipoles above various ground-plane, high-impedance, or absorber surfaces. Chap. 5 and Chap. 6 focus on a choke-ring shield design, with Chap. 5 studying the effects of particular design parameters on choke ring performance, and Chap. 6 discussing fabrication and measurement of choke-ring shields, along with comparable cavity shields. Additional material on signal processing and time-domain signals included in Appendix A. Though this material is important to the interpretation and analysis of time-domain signals for pulsed antennas, the material is somewhat peripheral to the discussion of antennas themselves, and is thus left for an appendix.

1.4 Simulation Details

Two different numerical EM solvers were used to produce data in this thesis. HFSS using the finite-element method was used for all frequency-domain data. Adaptive meshing was used, with a convergence criteria of S-parameter variation below 0.005, with a minimum of two converged passes. Second order (quadratic) basis functions were used. Time-domain data was produced using CST microwave studio's finite-difference time-domain (FDTD) solver, with a variable mesh size of maximum $\lambda/10$ at the highest frequency.

Chapter 2

Absorbers

This chapter will consider a variety of microwave absorbing structures, with a thorough review of the literature. A typical application of absorbers is microwave measurements, where undesired reflections from the environment can introduce error into the measurement. By covering reflectors with absorbers, these multipath effects can be reduced. Absorbers can also be incorporated into an antenna design, such as by using them to coat unwanted radiating surfaces.

Microwave absorbers are often designed using circuit principles, as applied to a normally incident plane wave. Absorber design is closely related to the design of filters or matching networks, and share many of the same theoretical principles. Absorbers can often be classified as either resonant, or non-resonant [15]. Resonant absorbers typically achieve good matching close to a single frequency, often through a destructive interference mechanism. In contrast, non-resonant absorbers work by creating a tapered match to free space, and have a more broadband response. This is usually at the cost of size, where a longer electrical length is necessary to create the smooth taper.

2.1 Salisbury Screen

The Salisbury screen, pictured in 2.1, is a classic microwave absorber, developed for microwave and radio frequencies during WWII, and named after its inventor [16]. This absorber modifies a metallic surface, preventing reflection by absorbing incident radiation at a single frequency. It achieves this through a $\lambda/4$ resonance, and is thus usually considered somewhat impractical due its large thickness and narrow bandwidth [15, 17]. Nevertheless, it is one of the simplest, and most fundamental absorber designs, from which other designs can be understood, and well worth studying.

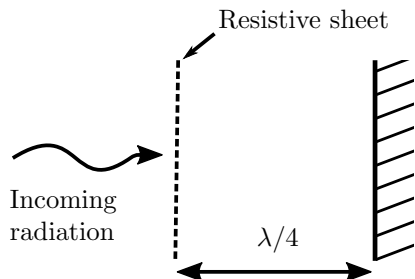


Figure 2.1: Geometry of the classic Salisbury screen, which achieves absorption by spacing the resistive sheet a resonant length away from the backing metallic plane.

The Salisbury screen absorbs radiation through ohmic loss in a resistive sheet, which is placed a distance of $\lambda/4$ from the backing metallic plane. For an incoming plane wave at normal incidence, the $\lambda/4$ separation of the resistive sheet from the metallic surface can be modeled as a transmission line, which transforms the short-circuited metallic surface into an effective open circuit. The resistive sheet enforces a ratio between the tangential electric and magnetic field components, which is termed the surface impedance. For an isotropic surface in the x - y plane, the surface impedance (sometimes referred to as the sheet impedance) is defined by the relations:

$$Z_s = \frac{E_x}{H_y} = -\frac{E_y}{H_x} \quad (2.1)$$

For electrically thin sheets, the surface impedance depends on both the thickness and bulk conductivity. For sheets where the resistive loss dominates, the surface impedance is given by the equation [16]:

$$Z_s = \frac{1}{\sigma t} \quad (2.2)$$

where t is the surface's thickness. In parallel to the open circuit created by the $\lambda/4$ separation, the plane wave sees an effective input impedance equal to Z_s . By setting Z_s equal to the free-space wave impedance $\eta = 377\Omega$, the plane becomes perfectly matched, and all incident energy is absorbed.

The above presents a basic analysis of the Salisbury screen, for which there are further practical considerations. Realizability of the resistive sheet is of great importance. Such sheets are commonly fabricated using carbon compounds embedded in a plastic or polymer substrate [18, 19, 20]. Furthermore, resistive sheets can also have a significant capacitive component, depending on the dielectric constant and thickness of the sheet [17, 21], which tends to reduce the resonant size. Finally, a common variation is to miniaturize the structure by increasing the dielectric permittivity value between the resistive sheet and the metal surface, reducing the size by altering the wavelength inside the dielectric. This comes at the cost of bandwidth, with higher values of dielectric constant reducing both size and bandwidth [22].

2.2 Jaumann Absorber

The Jaumann absorber attempts to improve upon the small bandwidth of the Salisbury screen through the inclusion of multiple resistive layers, shown in Fig. 2.2. For each additional layer, the number of design parameters increases significantly, along with design complexity. One common design strategy is to choose a constant $\lambda/4$ spacing between all the sheets, making the response around this frequency flatter, and thus improving bandwidth [21]. To achieve a

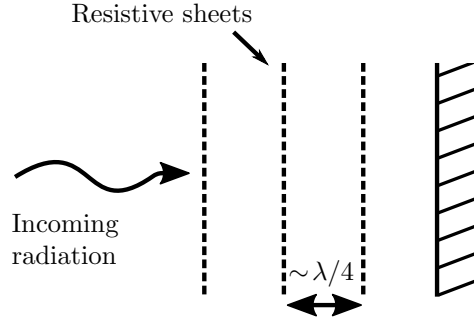


Figure 2.2: Example of a three-layer Jaumann absorber, which uses multiple resistive sheets spaced at lengths that are approximately resonant.

broader response however, a more optimal design is to slightly detune the spacing away from $\lambda/4$. Since each additional layer potentially adds another zero in the reflection coefficient as a function of frequency, this has the effect of spreading out the zeros over a wider bandwidth [23], thus improving the bandwidth for a given reflection level. This approximately produces a maximum bandwidth response, which is a common design goal for Jaumann absorbers. There are alternative design optimizations however, including Chebyshev or Butterworth responses [24, 25]. Another prominent Jaumann design methodology is to use a non-resonant spacing between resistive layers, choosing a smooth taper of surface impedance values [25, 26]. This has the effect of creating a smooth transition into free space, providing broadband matching, especially at higher frequencies.

Jaumann absorbers suffer from many of the same practical issues and non-idealities discussed for the Salisbury screen. Sheets with some thickness and dielectric constant will have a capacitive component, which needs to be taken into account when designing such an absorber [23, 27]. Due to the large number of design variables necessary to consider when optimizing a multilayer Jaumann absorber, there has been a large focus in the literature on computational methods for design, with a particular focus on genetic algorithms [27, 28, 29]. In addition to their ability to optimize the reflection coefficient over some band-

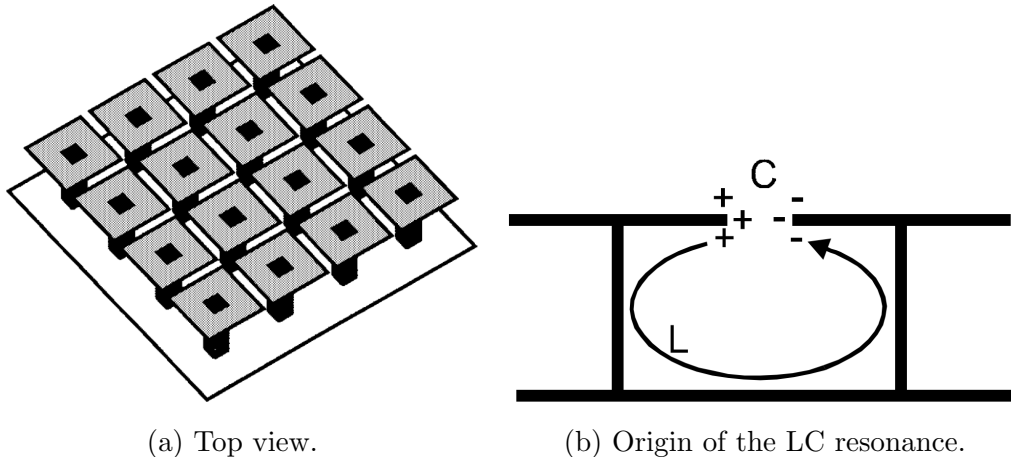


Figure 2.3: The Sievenpiper high-impedance surface [3].

width, genetic algorithms have the advantage of being able take material considerations such as weight and mechanical stability into account, while selecting from a discrete library of available materials [30, 31]. It is also possible to design Jaumann absorbers that work at oblique angles, which is a topic of some interest [32, 33].

2.3 High-Impedance Surface Absorbers

In recent years, there have been a huge variety of absorbers based on high-impedance metasurfaces, or similar metamaterial inspired surfaces. Even though they are inspired by metasurfaces more generally, these structures developed out of the literature on frequency selective surfaces (FSS), and similar absorbers based on FSS design are also commonly referred to as high impedance surfaces [34, 35, 36]. These are also referred to as EBG surfaces. We shall start by considering one of the simplest, which is an absorber related to the high-impedance Sievenpiper surface [3, 34], shown in Fig. 2.3. The Sievenpiper surface can be understood as achieving an LC resonance, with the resonant portion contributed by inductive vias, and the capacitance through the gap

capacitance between patches. In this capacitive gap, electric field magnitudes are enhanced, and a high degree of loss can be achieved by loading it with a resistive material, or lumped resistor. Conceptually, this absorber works on a very similar principle to the Salisbury screen, in that it uses an open-circuit resonance to achieve a purely resistive surface impedance at the design frequency. Compared to the Salisbury screen however, this design is greatly miniaturized, as a result of the LC resonance. Ideally, the lumped-element resistance between patches should be 377Ω . In practice, due to additional metallic and dielectric losses, it will need a resistance value of somewhat higher than 377Ω [37].

For the Sievenpiper surface, the via is thought to contribute to the inductance in the LC resonance. For a normally incident plane wave however, the electrical length through the metal-backed dielectric provides a similar inductance regardless of the via [38]. It has thus been noted that while the via increases the performance of a high-impedance absorber at oblique angles, they are not generally required [39, 40]. A large variety of such via-less absorbers have been developed, usually by backing a lossy FSS design with a ground plane, separated by a dielectric. Though there exist designs using lumped-element resistors as the loss mechanism [41], many more form the entire FSS out of a single material layer that can be described by its surface resistance [35, 36, 42, 43]. There also exist some designs that use a purely metallic FSS structure, incorporating loss instead into the dielectric layer [44, 45].

In terms of FSS design, there exist a large variety of geometries, such as patch, cross, Jerusalem cross, ring, concentric rings, etc. [46, 47] that can potentially be incorporated into an absorber. Despite the vast range of available shapes however, most can be understood in terms of simpler circuit models. Capacitive structures are common, with elements such as the patch being describable by a pure capacitance at asymptotically low frequencies. Since the ground plane as separated by the dielectric spacer is inductive at lower frequencies (up to the $\lambda/4$ resonant length), the FSS element needs to have an effective

capacitive impedance to achieve the LC resonant condition necessary for absorption. Hence, all of the most efficient high-impedance absorber designs use FSS elements which are capacitive at low frequencies [48]. This also provides a connection to the Salisbury screen and Jaumann absorbers discussed above, which see miniaturization when using resistive layers with an additional capacitive reactance. At higher frequencies, such FSS elements are often described in terms of series RLC networks, or even more complex multi-resonant networks [49]. These multi-resonant networks have a role similar to the additional layers of a Jaumann absorber, in that they add additional zeroes to the reflection coefficient, and allow for a reflection coefficient optimized over a wider bandwidth. There are also examples of multi-layer FSS designs which achieve a similar result, with the advantage of a simplified FSS unit cell geometry compared to single-layer designs [48, 49].

2.4 Dielectric Absorbers

Some of the most common microwave absorbers in use today are tapered dielectric absorbers. Their invention goes back to the 1950s, and the concurrent development of anechoic chambers [26]. The basic design philosophy was to create a tapered loss profile, to create a broadband match to free space [50, 51, 52]. This loss profile can be made by varying conductive inclusions, such as carbon black, within a dielectric matrix. Often, the matrix is chosen to have a dielectric constant close to free space, to reduce reflection. Another common method is to taper the geometry to achieve matching, such as in the case of pyramidal absorbers [53]. Since it is not practical to continuously taper material properties, multilayer structures that approximate a smooth taper are much more common. There are also examples of multiband, or thin resonant absorbers, which take advantage of destructive interference to achieve absorption [52, 54].

Multilayer dielectric absorbers share many of the same advantages and diffi-

culties as Jaumann absorbers. In particular, due to the large number of design parameters with each additional layer, optimization can be extremely difficult. Much of the modern literature thus focuses on numerical optimization, particularly genetic or similar algorithms that are capable of designing from a library of available materials [55, 56]. There is also a lot of interest in material design and characterization, especially of carbon nano-composite materials [57, 58, 59].

2.5 Ferrite & Magnetic Absorbers

Ferrites, or more generally any material with a magnetic response, have been found to enhance absorption and reduce thickness in a variety of designs [21, 26, 52, 60]. One way to understand this is that a plane wave reflecting off a metal plane has an enhanced magnetic field. Any material with magnetic loss placed close to a metallic reflector will thus see enhanced absorption. In analogy to designs like the Salisbury screen or high impedance surfaces, which place a resistive layer where an open-circuit response is achieved, a magnetically lossy sheet in front of a short-circuit will see enhanced loss. Such a single layer absorber, or the multi-layer extension, is sometimes referred to as a Dallenbach layer [61, 62].

Much of the literature on multilayer dielectric structures discussed earlier is similarly applicable to multilayer absorbers with magnetic properties; much of it considers both electrical and magnetic materials in a general framework. Since the major drawback of ferrite absorbers are usually weight and reduced permeability at high frequencies [63], most of the literature has focused on ferrite compounds or composites that address these issues. For example, so-called M-type ferrites have been successful at increasing the magnetic response at higher frequencies, with thin absorbers demonstrated up to X-band frequencies [64, 65]. A wide variety of nanocomposites composed of variously carbon, ferrite, or iron compounds have been considered, with the advantages of being

both lightweight, and having tunable properties, depending on the inclusion concentrations [66, 67, 68]

2.6 Metamaterial Absorbers

Metamaterial absorbers take a very different design approach compared to more traditional absorber designs, through the direct engineering of effective material parameters using artificial periodic structures. Much of the original interest in metamaterials was spurred by the promise of the exotic properties of negative refractive index materials [69], and then finally the experimental realization of such a material [70]. In the context of a negative refractive index, a common method was to design for $\epsilon_r = -1$ and $\mu_r = -1$, such that the wave impedance $\eta = \sqrt{\mu/\epsilon}$ inside the material was matched to free space. Achieving these negative values however, typically requires a resonant condition that tends to enhance loss, and contributes an additional imaginary portion to the material parameters. Though undesirable for applications requiring the negative refractive index, this was used to design an effective medium with a high degree of loss, and perfectly matched to free space [71]. Notably, unlike designs considered previously, this one does not rely on the presence of a backing conductor.

In designing an effective medium, mechanisms to modify both the magnetic and electric response need to be considered. The thin wire medium is a commonly cited example of an electric plasma at microwave frequencies, which exhibits a plasma resonance [72], and has been used in many metamaterial designs. A magnetic response can be had using split ring resonators, or spiral resonators [73, 74]. There are also designs that achieve both a magnetic and electric response in a single element, or take advantage of coupling between electric element layers to achieve the magnetic response [71, 75, 76].

Since metamaterial absorbers rely on typically narrowband resonances, there have been efforts to create more broadband designs. This can be done, for

example, by stacking metamaterial layers tuned for multiple closely-space frequencies [77], or using elements with a multiresonant response [78]. A similar approach has been used to design multi-band absorbers as well [79, 80].

One problem that has hampered the development of metamaterial absorbers is the difficulty of design. Given the difficulty of engineering frequency-dependent ϵ and μ directly, it is not immediately clear what the advantage of metamaterial designs are compared to similar FSS designs. There is also an ambiguity of terminology, in that many designs which use periodic unit cells are variously referred to as metamaterial, even when effective material parameters are not considered in the design. It has also been suggested that multilayer metamaterial absorber designs fit generally within the framework of FSS absorber design [81]. Nevertheless, metamaterial research has been incredibly influential on absorber design, and is another paradigm in which absorbers employing periodic unit cells can be understood.

2.7 Thickness-Bandwidth Limitations

In the above-considered designs, there has been a general pattern where resonant structures were capable of producing thin, narrowband absorbers, in contrast to tapered or multiresonant absorbers, which were capable of greater bandwidths, at the expense of thickness. This has been shown to be a constraint of causality, limited by the inequality [82]:

$$-\int_0^\infty \ln |\Gamma(\lambda)| d\lambda \leq 2\pi^2 \mu_s d \quad (2.3)$$

where Γ is the reflection coefficient, d is the total absorber thickness, and μ_s is the average static relative permeability of the absorber. Since $\ln |\Gamma|$ is essentially the reflection coefficient as measured on a logarithmic or decibel scale, the integral in Eq. 2.3 can be understood as representing the total bandwidth of an absorber. In this sense, Eq. 2.3 shows how the absorption

over all frequencies is limited by the thickness of the absorber, together with its permeability. This is comparable to similar limits on broadband matching networks [83, 84]

One important implication is that all non-magnetic absorber designs have fundamentally the same bandwidth limitations, and that the only way to meaningfully increase bandwidth is to use a thicker absorber, or include magnetic materials. It is also insightful to recast the integral of Eq. 2.3 as an integral over frequency.

$$-\int_0^\infty \frac{\ln |\Gamma(f)|}{f^2} df \leq \frac{2\pi^2 \mu_s d}{c} \quad (2.4)$$

The $1/f^2$ factor in this form shows us that low-frequency bandwidth is more “expensive” compared to at higher frequencies, and that there is no general limit on absorption at arbitrarily high frequencies. If we use some given reflection level, such as reflection below -20 dB, as our criteria for bandwidth, then this equation has a simpler interpretation.

$$-\ln |\Gamma| \frac{\Delta f}{f_{\text{av}}} < 2\pi^2 \mu_s \frac{d}{\lambda_{\text{av}}} \quad (2.5)$$

In this form, $\ln |\Gamma|$ is now our chosen level of acceptable reflection, λ_{av} is the average wavelength over the bandwidth, $f_{\text{av}} = c/\lambda_{\text{av}}$ is the corresponding average frequency, and $\Delta f/f_{\text{av}}$ is the fractional bandwidth about this frequency. This form of the equation directly relates a given reflection level to both the fractional bandwidth, as well as the absorber thickness as a fraction of a wavelength. There are some non-magnetic absorber designs that have gotten very close to this limit [85].

As a note of caution, f_{av} is not the arithmetic average of the upper and lower frequencies of the band, but rather the geometric average. For narrow bandwidths however, the two are approximately equal.

As an example, given a non-magnetic absorber that achieves uniform -20 dB matching over its bandwidth, with a bandwidth between 0.5 GHz and 2.5 GHz,

what is the minimum thickness of this absorber? For easier calculation, we can use an alternate form of Eq. 2.5.

$$-\ln |\Gamma| \left(\frac{1}{f_{\text{low.}}} - \frac{1}{f_{\text{upp.}}} \right) < \frac{2\pi^2 \mu_s d}{c} \quad (2.6)$$

Given the above constraints, we find that a minimum thickness of 5.6 cm is required. This is a hopeful result, in that absorbers operating over a realistic GPR bandwidth of 2.3 octaves are possible using thicknesses of roughly $\lambda/10$ at the lower frequency. With the additional use magnetic materials, which tend to perform well at lower RF frequencies, it seems likely that absorbers that work over large bandwidths at GPR frequencies could reasonably be developed.

Chapter 3

Ground-Plane Shields

The previous chapter considered absorbing materials, which are a common way of isolating reflecting structures from an exciting antenna. An example application might be to coat nearby scattering structures to reduce clutter in a radar measurement. A complimentary approach, however, is to use antenna pattern-shaping structures such that the radiation is reduced in the direction of scattering structures. This is applicable in situations for example where the antenna needs to operate in variable environmental conditions, where the user does not have strict control over the surrounding environment. While there are array designs that achieve this goal [86], such structures are often very large, expensive, and often require complex feed networks. Instead we will consider simpler ground plane and similar structures. We will also consider high impedance surfaces, which fulfill a similar role, and solve some of the issues seen in conventional, finite ground planes.

3.1 Finite Ground Planes

Ground planes are integral to a large number of antenna designs, and are used in applications where it is desirable to isolate radiation to a single hemisphere. While this is true for ideally infinite ground planes, the finite truncation of a

ground plane can significantly affect an antenna's properties. For example, in the case of vertical monopole antennas mounted above a ground plane, variations in input impedance between 5% and 20% were seen for ground planes up to 6.1λ in size [87, 88]. This variation tended to oscillate as a function of both ground plane size and frequency, suggesting a resonant interference effect, which was attributed to scattering from the ground plane's edges. Interestingly, this effect has been used to tune the input impedance of an ultra-wideband (UWB) vertical monopole at the lower-frequency edge of its bandwidth, with enhanced matching for a 1λ diameter ground plane [89]. Ground plane size has similarly been found to affect impedance characteristics of ground-plane-backed spiral antennas, where similar oscillatory behaviour with frequency tends to obstruct their wide-band impedance properties [90, 91, 92, 93].

Finite ground planes can also significantly alter an antenna's radiation characteristics. This has been most widely studied in the context of microstrip patch antennas. Similar to the periodic effect on input impedance, gain was found to have a periodic dependence on ground plane size, with gain enhancement for planes of around 1.2λ in size. Patch antennas also saw increasing back lobe for smaller ground plane sizes, but especially for ground planes 0.5λ and smaller [94, 95]. Similar results exist for slot antennas as well [96, 97], with input impedance effects generally also applying to these antennas.

3.1.1 Diffraction Effects

A common interpretation of these effects is that they are due to the excitation of surface wave modes, which are supported on a metal-backed dielectric substrate. These surface waves, as they encounter discontinuities, tend to scatter, resulting in a radiated as well as reflected component. This is especially the case at the edge of a finite ground plane, and surface wave suppression thus has the effect of reducing diffraction around the ground plane [96, 98, 99]. Resistive tapers or absorbers at the edge of the ground plane are a common design

method to reduce these diffraction effects [90, 91, 92, 93, 100, 101].

Edge diffraction effects are often modeled by treating the edge as an additional source, with the most common model of this variety being the geometrical theory of diffraction (GTD) [88, 102, 103, 104]. It is worth noting that these models tend to be asymptotic, and do not work for smaller ground planes, a guideline being that the ground plane edge should be at least $\lambda/4$ from the antenna.

Though this discussion has focused on surface waves, these models do not necessarily rely on the existence of closely bound surface-wave modes, and predict similar diffraction effects when no dielectric is used. Note however that surface-wave modes are generally non radiative except at discontinuities. As a result, surface waves tend to travel along a ground plane with much lower path loss compared to usual spherical wave fronts, which results in enhanced field magnitude and diffraction at the ground plane edge for a surface wave. Without a dielectric, no bound surface-wave modes exist, and currents on a ground plane will experience radiation loss as they travel to the edge, reducing the diffraction effect.

3.1.2 Small Ground Planes

For smaller ground planes, the radiation pattern can depart even more radically from the infinite case. In some cases, a small ground plane backing an antenna may enhance radiation in the back direction, rather than suppress it. Antennas of this variety are referred to as backfire antennas [105]. Backfire antennas were originally developed from Yagi-Uda designs. In a typical Yagi-Uda design, there are thin-wire director and reflector elements. The original backfire antenna placed a large reflecting ground plane at the endfire direction of a Yagi-Uda antenna. The result was that typical Yagi-Uda endfire radiation would reflect off the ground plane, and be forced to travel down the antenna structure, but in the opposite direction, eventually radiating out of the direction usually

considered backfire [106]. This resulted in a gain enhancement in the range of 4–6 dB.

This was conceptualized as being effectively a leaky cavity antenna, with energy trapped between two reflector elements, and leaking out the direction of the smaller of the two reflectors. As the design evolved, the thin-wire reflector element was replaced with a circular plane reflector, and the director elements were removed entirely. This new design was referred to as the short backfire antenna [107, 108]. The smaller of the two reflecting discs however, required a diameter of around 0.5λ or less, and could be conceived as acting like a traditional Yagi-Uda director element, but in a planar disc geometry. There is also an example of a backfire helix antenna, which switches from endfire radiation to backfire as the radius of its ground plane is decreased [109]. This design uses a 0.29λ diameter ground plane, and achieves a 10 dB gain in its backfire direction, while having otherwise typical dimensions for a helix antenna.

3.1.3 Cavities

Cavity shields are a typical shield variation, fulfilling the same role as a ground plane in most applications. Cavity shields are often perturbations on a similar ground plane shield, where a small rim is added to the ground plane, with the effect of improving gain as well as reducing back and side radiation [94, 110]. Larger cavity walls up to a height of $\lambda/4$ are also common [108, 111]. These cavities can roughly be thought of blocking line-of-sight radiation, making them an attractive choice for reducing coupling of side-by-side antennas, such as for GPR antennas [11, 12].

Analytical models for cavity shields are relatively sparse. What models do exist tend to consider the fields inside the cavity as waveguide modes, treating the aperture fields as an equivalent source [112, 113]. There is however, a rich literature on plane-wave scattering from open-ended cavities. A variety of analysis techniques have been used for the scattering problem, including but not

limited to ray tracing, waveguide-modal models, GTD, and numerical models [114, 115, 116, 117, 118]. Some of the results of this literature include the cavities acting similarly to metallic cylinders below the cutoff frequency of the lowest-frequency mode, as well as enhanced scattering at angles corresponding to waveguide mode angles at that frequency. It is suspected that similar results should hold for an exciting antenna closely spaced to a cavity shield.

3.1.4 Electromagnetic Band-Gap Structures

Designs using EBG surfaces have been successfully used to reduce diffraction effects on finite ground planes, and reduce coupling to nearby structures. The EBG property specifically refers to the lack of propagating modes along the surface within particular frequency bands. As a result, EBG structures prevent the propagation of currents and radiation along their surface. As an alternate mechanism, surfaces that re-radiate currents excited on them as leaky waves may also be considered EBG structures. In this case, the re-radiation tends to attenuate currents along the surface. EBG surfaces are typically realized using periodic structures. Influential EBG structures include the Sievenpiper surface [3], the uniplanar compact EBG [119], and corrugated surfaces. Corrugated surfaces are notable in particular for their anisotropy, which has been used to design the so-called soft surface, capable of blocking radiation of different polarizations in different directions [120]. This is described in greater detail in Chap. 4.

Typical applications for EBG surfaces include the reduction of coupling between nearby antennas [121, 122, 123], or antennas and their surround environment (e.g. lossy dielectrics for cellular antennas) [124]. By reducing currents at the edge of an EBG ground plane, EBG surfaces reduce diffraction effects, and thus backlobes compared to similarly sized plain ground planes [13, 125]. This mechanism is also used in the context of corrugated horn antennas to increase beam efficiency and reduce sidelobes or spillover [126]. Diffraction models used

for ground planes can similarly be used for EBG structures. UTD for example, was used to model diffraction effects at the edge of choke ring planes [127].

3.2 Diffraction Formulations

Since the effects of a finite ground plane structure can largely be understood within the context of diffraction effects, here we go into a bit more detail about a variety of diffraction models, and consider their applicability to shielding structures backing antennas.

3.2.1 Scattering Solutions

The case of scattering of a plane wave from a spherical structure is referred to as Mie scattering. Though a spherical shield is not a useful structure in antenna design per se, Mie scattering shows some of the effects that a scattering structure can have at different size regimes, and is extremely well understood. The characteristic feature of Mie scattering is that for metallic or dielectric spheres with size comparable to the wavelength of the impinging radiation, the reflectors undergo a resonant condition. Near this resonant size, the scattered power tends to have strong fluctuations as a function of both size and frequency, and can also show enhanced dielectric or ohmic loss. This effect has been used to enhance the radar cross sections of scatterers, and is important in atmospheric studies [128, 129, 130, 131, 132], as well as optical biomedical applications [133, 134, 135, 136].

Mie scattering provides a good example of the kinds of behaviour a reflector can have at different size regimes. For small sizes or low frequencies, the sphere scatters according to Rayleigh scattering, where its response is dominated by its dipole moment. In this regime, the scatterer is a fairly poor reflector relative to its size, and most of the incident energy tends to diffract around the particle. As the size of the sphere approaches that of a wavelength, resonant modes are

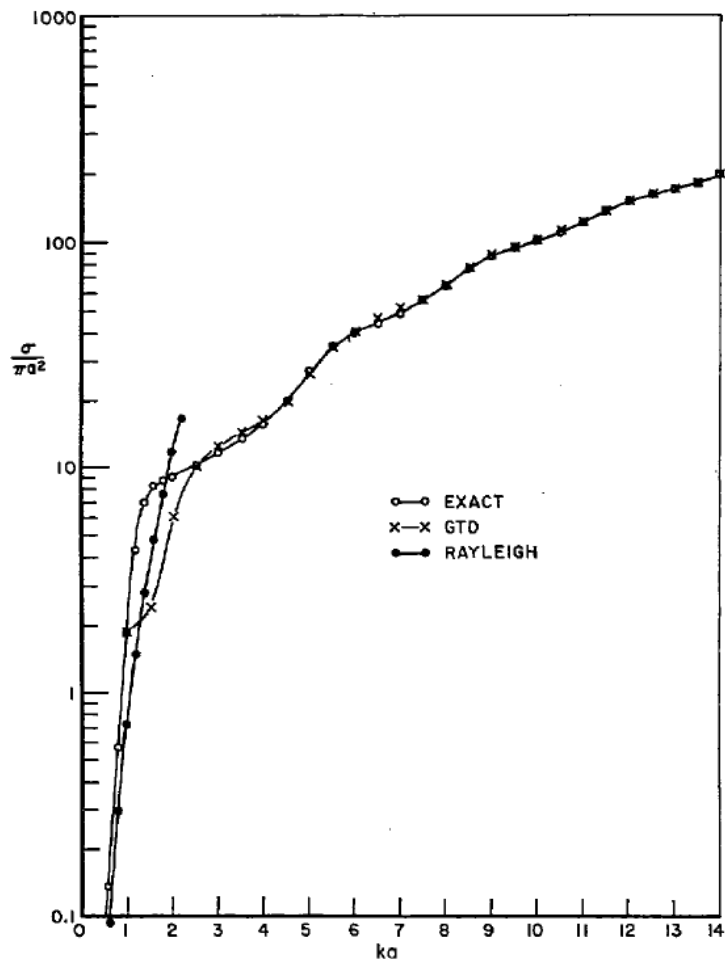


Figure 3.1: Normalized scattering cross section of a disc versus its electrical size [4]. Disc radius is given by a , wave number by k , and scattering cross section by σ . Comparison to GTD and Rayleigh scattering is shown.

excited near the sphere's surface, and the sphere shows enhanced scattering. These resonances are essentially spherical harmonics on the sphere's surface, and occur approximately when the circumference of the sphere is a multiple of a wavelength [137]. This is often described in terms of surface-wave modes on the sphere. The term creeping waves is also used, which emphasizes how waves seemingly "creep" around the sphere by continuously diffracting along the curved surface, and thus traveling all the way around the sphere [50, 138, 139]. At higher frequencies, the sphere's scattering approaches that of optical

diffraction, and is well approximated by GTD or similar methods.

Though not nearly as well studied as the case for a spherical scatterer, there is strong evidence that a disc reflector undergoes similar kinds of phenomena as seen in the Mie solution. Since the disc can be seen as the limiting case of a spheroidal surface, a solution akin to the Mie scattering solution exists by solving the boundary value problem in spheroidal coordinates [4]. Fig. 3.1 shows how the disc has the same asymptotic limits, with low frequencies agreeing with Rayleigh scattering, and high frequencies with GTD, with an intermediate frequency range where neither theory is accurate. This range is approximately given by $1 < ka < 2$, where a is the radius of the disc.

3.2.2 Edge Diffraction

Methods describing diffraction in terms of discrete contribution from edge sources have been very successful in predicting the behaviour of ground planes, or other scattering structures. We shall start by describing the exact solution to an infinite edge, before relating this to other formulations.

The exact solution to diffraction by an infinite edge is referred to as the half-plane problem, originally solved by Sommerfeld [140]. This is a special case of knife-edge or wedge diffraction, when the angle of the wedge approaches zero. Using an asymptotic approximation, the Sommerfeld solution is often decomposed into a combination of a geometric optics solution and a diffracted cylindrical wave emanating from the diffracting edge [5, 141]. This forms the basis of treating the edge as an equivalent source term, which forms the basis of the GTD formulation [142], as well as the updated version, the uniform theory of diffraction (UTD), which improves smoothness between shadow and plane-wave regions [143].

This treatment of edges as equivalent sources works well with an interpretation in terms of Huygens wavelet sources at the edges. This interpretation is useful in understanding the impulse response of diffracting structures

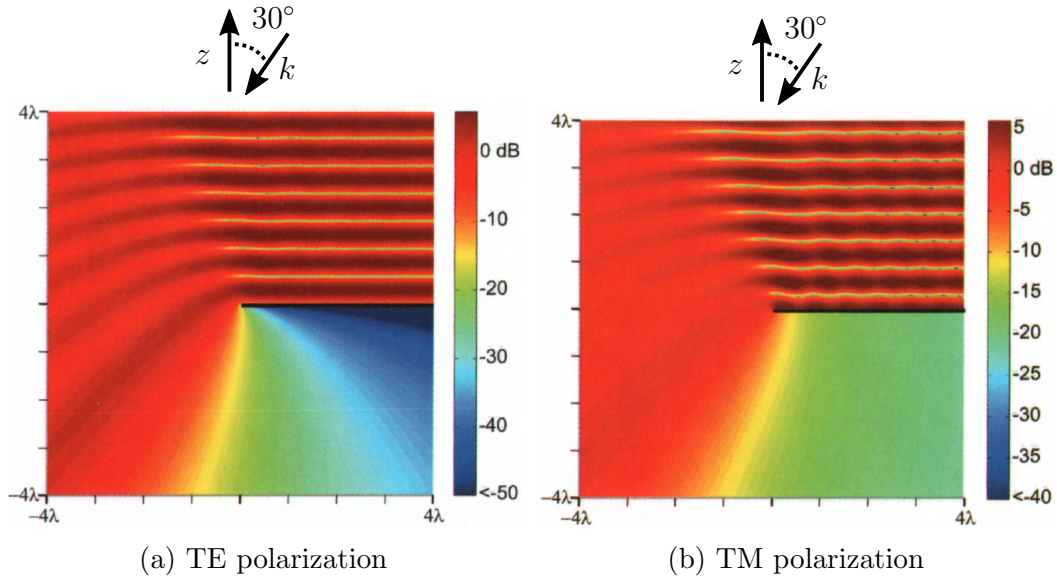


Figure 3.2: Field magnitudes for plane waves incident at 30° from the z axis, diffracted by a PEC half plane. The two perpendicular field polarizations are shown [5].

[118, 144, 145, 146]. In this perspective, the Huygen source from an edge can then propagate and be diffracted a second time, and so forth. The resulting time-domain response is thus a combination of multiply diffracted wavefronts, with a time delay related to the propagation time across the scattering surface.

The Sommerfeld solution to the half-plane problem also reveals how the polarization of the incident wave affects the diffraction around an edge, as shown in Fig. 3.2. For the case where the incident E field lies tangent to the plane (Fig. 3.2a, TE polarization), diffraction around the edge is greatly reduced. In contrast, the TM polarization shown in Fig. 3.2b has significant diffracted fields along the backside of the plane. Hence, diffraction effects should primarily be seen along edges where the excited field has a TM polarization.

3.3 Shielded Dipole

In the previous section, we considered a variety of effects seen in ground plane shields, and some of the models used to analyze them. Some of these effects were studied in the context of scattering formulations considering a plane wave source. Here, we introduce a practical dipole source, and consider its response as backed by either disc or cavity structures. The dipole used in these studies is a small resistively loaded dipole, with a length of $\lambda/4$ at 1 GHz (7.5 cm), and loaded with four equally-spaced $50\ \Omega$ resistors on each arm (eight resistors in total). The dipole was fed with an input impedance of $200\ \Omega$ in all cases. This dipole model was chosen for its low dispersion and time-domain response when fed by a wideband input pulse. This is a reasonably practical antenna in the context of GPR, and as a short dipole, is generalizable to other dipolar source antennas.

3.3.1 Disc

When discussing the exact solution for an incident plane wave on a scattering disc, a major theme was the different behaviour in different frequency regimes. At low frequencies, the disc should act like a parasitic dipole, and at high frequencies, should behave similarly to asymptotic or optical formulations. In between these two regimes, it seems reasonable that there should be an intermediate resonant frequency regime. The idea of a disc resonant frequency is, for example, supported by the enhanced transmission at resonant frequencies for the complementary circular aperture (related via Babinet's principle), either for single apertures, or periodic arrays [147, 148, 149]. In the case of the single aperture, the transmission frequency is very closely predicted by the fundamental cutoff frequency of the corresponding waveguide problem. For a

circular aperture, this is the TE_{11} mode with a cutoff frequency given by:

$$f_{c,TE_{11}} = \frac{1.84c}{2\pi a} \quad (3.1)$$

corresponding to a wavenumber of $ka = 1.84$.

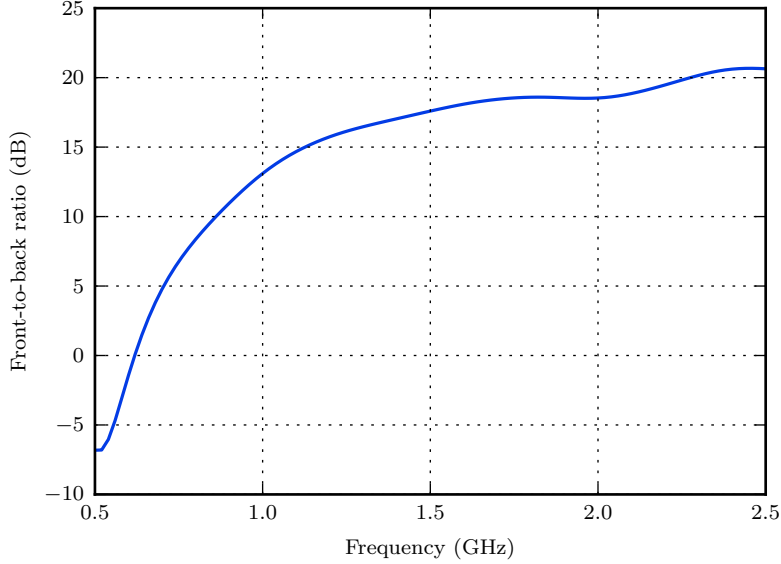


Figure 3.3: Front-to-back ratio for a horizontal dipole spaced 4 cm above a disc of radius 11.72 cm.

To study this, the small lossy dipole closely spaced to a disc reflector is simulated, and the resultant front-to-back ratio measured, shown in Fig. 3.3. The disc was designed to have a resonant frequency at 0.75 GHz, resulting in a 11.72 cm radius. The dipole was spaced 4cm above the disc.

The front-to-back ratio for the disc shield shows an extremely large increase from 0.5 to 1 GHz, then a much more gradual improvement at higher frequencies, which roughly parallels the expected behaviour for a disc in response to a plane wave at different sizes. At 0.5 GHz, the front-to-back ratio has a negative peak; the disc enhances gain, but in the *opposite* direction. This is similar to the backfire antenna concept. This behaviour is also consistent with the disc as a coupled parasitic dipole. Eq. 3.1 thus serves as an estimate of a min-

imum frequency for a ground plane, above which the ground plane performs reasonably well at isolating the antenna.

To study the time-domain response of the antenna, the antenna was excited with a wideband pulse with frequency components from 0.75 GHz to 2.5 GHz, and the resulting radiated pulse was measured in the antenna’s far field at boresight. To ensure no frequency components outside this bandwidth, and to avoid excessive ripple in the time domain due to windowing, the time-domain pulse was generated by applying a Kaiser window [150, 151]. The Kaiser window is parameterized by a value β , which can be chosen to adjust the pulse width, with a trade off in ripple level. The value of $\beta = 6$ is chosen, which was found to result in acceptable ripple levels. Further, the radius of the plane was parametrically varied from 5 cm to 34 cm.

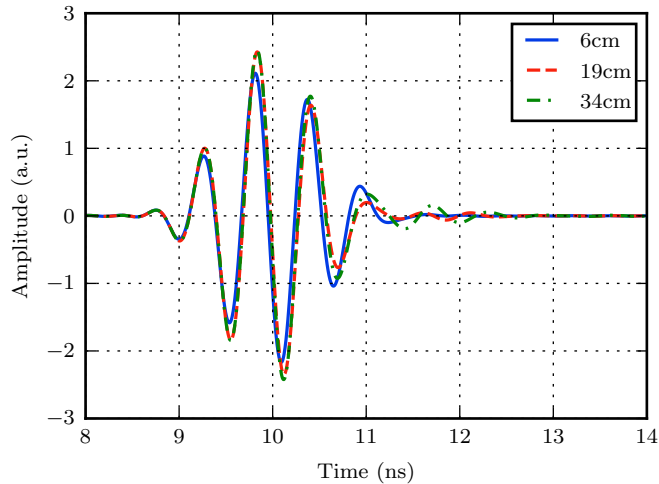


Figure 3.4: Radiated pulse amplitude for a dipole above a circular ground plane with parametrically varied radius.

The general observation was that signal components apart from the primary signal and reflection were observed, occurring at later times as the ground plane size increased. This is shown for selected radius values in Fig. 3.4. To more easily compare pulse shapes, the envelopes of the pulses are taken using a Hilbert transform, normalized, and plotted on a decibel scale. Details on the

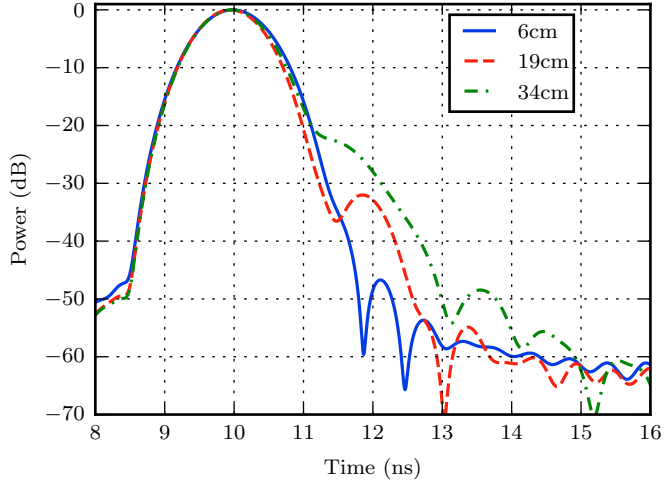


Figure 3.5: Normalized radiated pulse envelope for a dipole above a circular ground plane with a parametrically varied radius.

Kaiser pulse and Hilbert transform can be found in App. A. These results are shown in Fig. 3.5, and show very discernibly the increase in pulse width and clutter as the ground plane size is increased. This is suspected to be due to additional diffracted pulse components at the ground plane edge, which occur later in time as the ground plane size is increased. To test this, the maximum of the envelope is taken as a function of size, and plotted in Fig. 3.6. Evidently, the ground plane shows an additional signal component that interferes constructively and destructively with the primary signal, approaching the infinite ground plane case as the size increases. This is further evidence of a diffracted pulse component that is delayed in time as the ground plane size increases, and suggests that the ground plane radius can be optimized for maximum radiated pulse amplitude.

3.3.2 Cavity

Much of the cavity's behaviour can be understood by interpreting its effects in terms of circular waveguide modes within the cavity. Of these, the TE_{11} and

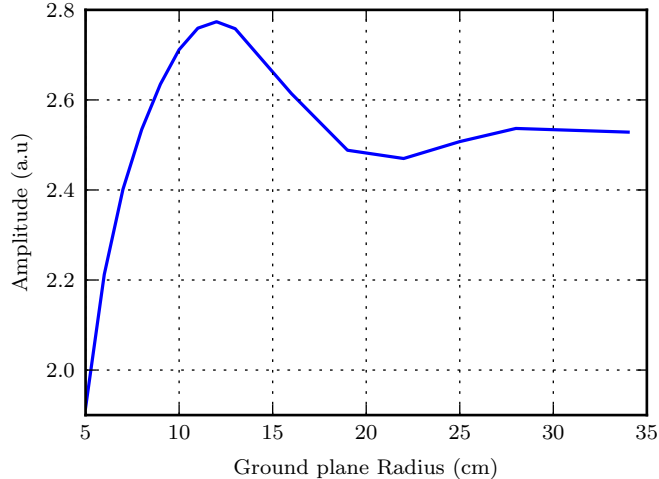


Figure 3.6: Maximum amplitude of the radiated pulse envelope as a function of ground plane radius, for a dipole above the ground plane.

TM₁₁ modes are both the lowest in frequency (taking symmetry into account), as well as the most significant theoretically. The TE₁₁ and TM₁₁ have fields as shown in Fig. 3.7. The cutoff frequency for the TE₁₁ mode is given by Eq. 3.1, while the TM₁₁ mode has a cutoff frequency given by the following equation:

$$f_{c, TM_{11}} = \frac{3.83c}{2\pi a} \quad (3.2)$$

In typical operation, the TE₁₁ is likely to be the dominant mode. For frequencies below $f_{c, TE_{11}}$, no significant energy penetrates into the cavity, and the cavity then acts similarly to a PEC ground closely backing the antenna. Hence, a sufficiently large cavity radius a is desirable, such that the lowest frequency in the operating bandwidth is above this cutoff frequency. For radiated pulses somewhat above $f_{c, TE_{11}}$, the dispersive properties of the TE₁₁ are minor, and energy can be assumed to propagate and reflect in a plane-wave-like manner. The cavity accepts and radiates the TE₁₁ mode efficiently, such that reflection of the TE₁₁ mode at the cavity opening is fairly insignificant. The TE₁₁ mode shows constructive and destructive phase interference at approximately

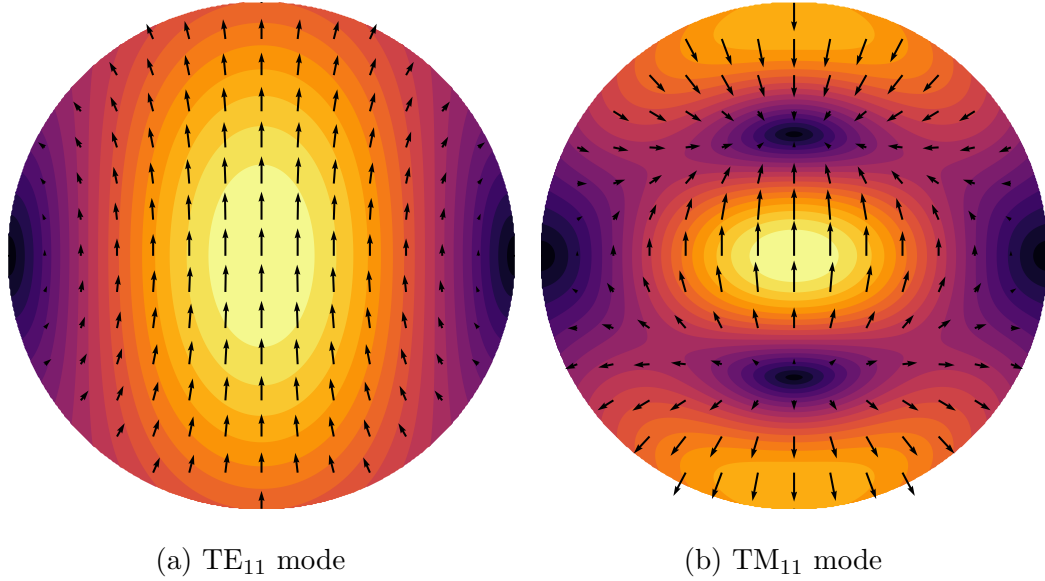


Figure 3.7: Transverse electric fields of the two lowest-order cylindrical waveguide modes, given a symmetrical excitation.

$\lambda/4$ and $\lambda/2$ depths respectively, comparable to a ground plane at a similar distance from the exciting antenna.

In contrast, the TM₁₁ mode radiates less effectively at the cavity opening, trapping energy in the cavity. As a result, the cavity shows resonance when the mode achieves a phase of $\pi/2$ along the cavity's depth, calculated as follows:

$$\beta_z d = \frac{2\pi d}{c} \sqrt{f^2 - f_c^2} = \frac{\pi}{2}$$

$$f = \sqrt{f_c^2 + \left(\frac{c}{4d}\right)^2}$$

Practically, near-fields above the cavity opening tend to increase the effective length of the cavity, such that the cavity shows a resonance very close to f_c , even when the depth d is small.

As a metric to evaluate the cavity's performance in shielding the antenna, the front-to-back ratio was found to be insufficient. One reason is that the cavity shows additional broad side lobes, due to radiation from the cavity

walls, that are not captured in a front-to-back ratio. Additionally, optimizing the cavity for high front-to-back ratio tended to produce very directive designs, which is not ideal for applications that require radiation over broad angles. Hence, in this work, a new metric termed the relative forward power (RFP) was devised. This new metric is the ratio of power radiated in the forward direction, as integrated over a hemisphere, to power radiated through the back hemisphere, taken in the far field. This can be calculated by integrating gain over all solid angles in each hemisphere, and taking the ratio.

$$\text{RFP} = \frac{\int_{\text{forward}} G(\theta, \phi) d\Omega}{\int_{\text{back}} G(\theta, \phi) d\Omega} \quad (3.3)$$

For an antenna with boresight along the positive z axis, these integrals can also be written explicitly as a double integrals.

$$\text{RFP} = \frac{\int_0^{2\pi} \int_0^{\pi/2} G(\theta, \phi) \sin \theta d\theta d\phi}{\int_0^{2\pi} \int_{\pi/2}^{\pi} G(\theta, \phi) \sin \theta d\theta d\phi} \quad (3.4)$$

RFP can similarly be calculated using directivity.

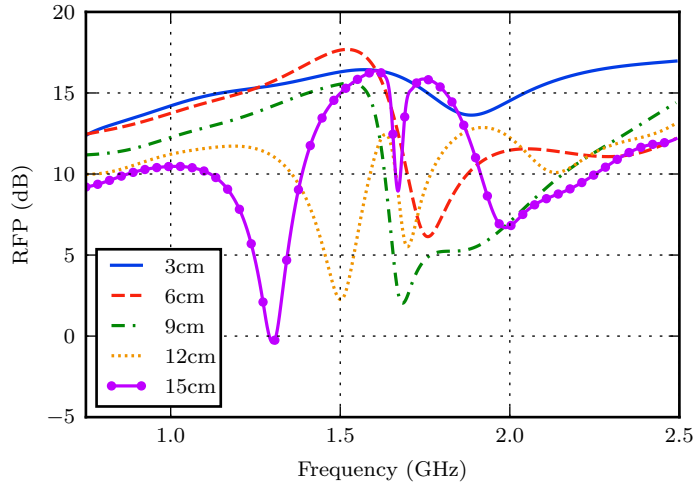


Figure 3.8: RFP vs frequency for different cavity depths.

To study the effects of particular waveguide modes on the cavity's perfor-

| Depth (cm) | TM ₁₁ $\lambda/4$ frequency (GHz) | | TE ₁₁ $\lambda/2$ frequency (GHz) | |
|------------|--|----------|--|----------|
| | Calculated | Observed | Calculated | Observed |
| 3 | 2.98 | 1.89 | 5.06 | - |
| 6 | 2.05 | 1.75 | 2.62 | 2.29 |
| 9 | 1.83 | 1.68 | 1.84 | 1.86 |
| 12 | 1.74 | 1.70 | 1.47 | 1.51 |
| 15 | 1.70 | 1.67 | 1.27 | 1.31 |

Table 3.1: Comparison of calculated resonant frequencies and frequencies for observed (simulated) resonant dips in RFP, for the two lowest order waveguide modes in the cavity.

mance, RFP was evaluated as a function of frequency as the cavity’s depth was parametrically varied from 3 cm to 15 cm. In all cases, a cavity with a radius of 11.25 cm, corresponding to a diameter of 0.75λ at 1 GHz was used. The cavity was excited at its open end by the small lossy dipole antenna. Fig. 3.8 shows these results. We can see a variety of dips that shift as the depth is increased. These are compared to the calculated resonant frequencies for the TM₁₁ and TE₁₁ modes, as shown in Tab. 3.1. For the TE₁₁ mode, the calculated frequency compares closely to the observed simulation frequency for most depths, though it starts to slightly diverge for shallower cavities. This can be inferred to be essentially a destructive phase interference effect, which is expected to cause a dip in the RFP. Deviation for shallower cavities is likely due to the increased contribution of evanescent near fields in the cavity for shallow cavities. Though the TM₁₁ calculated frequency also diverges for shallow cavities, the agreement is much worse. Rather, the observed TM₁₁ resonance is roughly constant around 1.7 GHz, and only starts to shift upward for extremely shallow depths. This is believed to be due to some combination of loading effects of the exciting antenna, as well as significant fields just above the cavity opening, adding effective length to the cavity. Instead, the observed resonant frequency is close to, but slightly higher than the cutoff frequency f_c , which is 1.6 GHz in this case.

The cavity’s time-domain response is also investigated. For this structure,

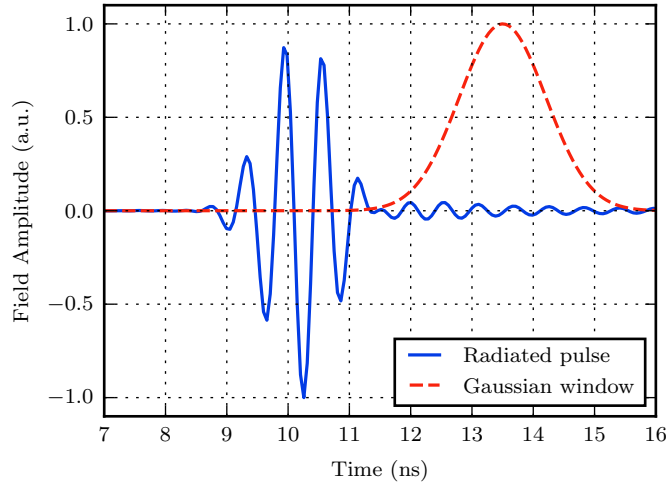


Figure 3.9: Radiated pulse for a cavity excited by a lossy dipole, and the Gaussian window that is used to find the spectrum of the pulse’s ringing.

the depth is set to 7.5 cm, and the structure is excited with the 0.75 GHz–2.5 GHz Kaiser pulse, with the resulting radiated pulse measured in the bore-sight direction. The resulting pulse is shown in Fig. 3.9, which can be seen to have a high degree of ringing after the initial pulse. To determine whether this is related to the TM_{11} mode resonance seen in the RFP, a Gaussian window is constructed, also shown in Fig. 3.9. This Gaussian has a width parameter of $\sigma = 0.5$ ns, and is centered around 13.5 ns, which was found to encapsulate the ringing without covering the main pulse. Multiplying the Gaussian window with the radiated pulse amplitude, the Fourier transform of the signal was then taken, with the normalized magnitude plotted on a decibel scale, shown in Fig. 3.10. This shows that ringing has a dominant frequency component at 1.74 GHz, which is the same frequency as the resonant effect seen in the RFP. This confirms that the TM_{11} mode produces a resonant phenomenon, which produces a high degree of late-time ringing in the time domain, and also worsens the cavity’s shielding at this frequency.

If we take the TE_{11} and TM_{11} cutoff frequencies as estimates of the minimum and maximum operating frequencies of a cylindrical cavity shield, we can

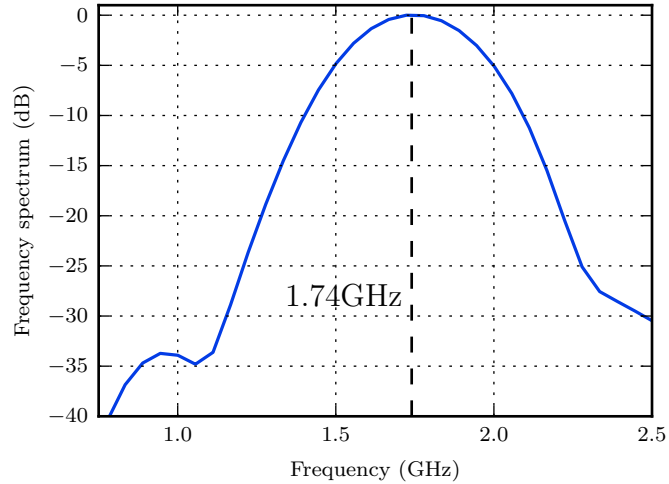


Figure 3.10: Frequency spectrum of the cavity's ringing.

use Eq. 3.1 and 3.2 together to get an estimate of the bandwidth of a cavity shield.

$$\frac{f_{c, \text{TM}_{11}}}{f_{c, \text{TE}_{11}}} = 2.08 \quad (3.5)$$

The result is that cavity shields have a bandwidth limit of roughly one octave. This is limited at high frequencies by the TM_{11} resonance, which is detrimental to both the time-domain pulsed response and shielding performance of the cavity. At the lower frequency end, any antenna is going to be increasingly inefficient due to destructive interference from the cavity, which acts like a closely spaced ground plane, as well as having increasingly worse shielding performance below this frequency.

Chapter 4

Surface Waves and Impedance

Surfaces

Surface waves were first described in the early 1900's by Zenneck, who described the first surface-wave solution to Maxwell's equations, as well as Sommerfeld, who related these solutions to the waves excited by a dipole antenna above a conducting half-space [152, 153, 154]. Surface waves saw renewed interest as a result of corrugated structures developed during the course of WWII that manipulated these waves [155], and were a major topic of publication in the decade that followed [156, 157, 158]. This led to the development of devices such as the cigar antenna [159] and corrugated horns [126, 160, 161], which were influential in the eventual development of choke rings used in GPS [162]. More recently, surface waves have been influential in optical research under the name of surface plasmons [163].

For our purposes, surface waves are a straightforward method to understand the operation of choke rings and similar high-impedance surfaces. This chapter will start by looking at canonical surface wave solutions to Maxwell's equations in a half-space terminated by an impedance boundary. Of particular interest is how the surface impedance values relate to the surface wave excitation, and how a surface wave may not exist for certain impedance values. This is followed

with an analysis of impedance surfaces in response to point dipole excitations, showing more rigorously how surface waves are excited, as well as how fields from a source behave when the surface does not support surface wave modes. This method of analysis also generalizes to dipoles above absorbers, and is used to find the field solution for a dipole above an absorber matched to free space at normal incidence. As a convention, this chapter assumes a time dependence of $e^{j\omega t}$.

4.1 Surface Wave Solutions

Surface waves can be thought of as the simplest wave solution to Maxwell's equations in a half space terminated by an impedance boundary [164]. Often, this is an approximate boundary condition, used to simplify the analysis by replacing a known field solution in part of the domain with this equivalent boundary condition. Inside metals with large finite conductivities for example, fields have a well-known form, related to the skin depth of the metal. Rather than solving the fields at an air-metal interface for any given problem, the metallic surface can be terminated in an equivalent impedance boundary condition.

Many natural surfaces have an inductive reactive component, with generally low impedance values. Examples include metal surfaces with some surface roughness, or metals covered by thin dielectrics. Capacitive, or high-impedance surfaces tend to be artificial surfaces.

Mathematically, the problem of solving for the fields above an impedance surface is very similar to that of the higher-order modes of a parallel plate waveguide, and is similarly composed of both TM and TE solutions, pictured in Fig. 4.1. The solutions are also analogous to plane wave solutions, but extended to include evanescent decay. For waves propagating in the x direction,

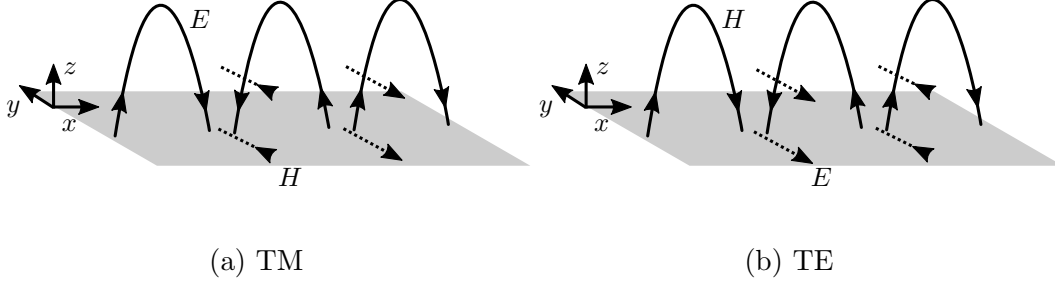


Figure 4.1: Fields of the TM and TE surface waves.

with z normal to the plane, we assume a solution of the form:

$$e^{-j\beta x - \alpha z} \quad (4.1)$$

with the usual relation:

$$k^2 = \frac{\omega^2}{c^2} = \beta^2 - \alpha^2 \quad (4.2)$$

By choosing solutions with positive exponential decay α away from the surface, we ensure that the solutions are bound waves. Large α implies a closely bound wave, while waves with small α values have fields that extend far away from the surface, and start to approach plane-wave-like behaviour. Eq. 4.2 also implies $\beta > k$, meaning these can be considered “slow-wave” solutions, and behave similarly to waves in a variety of slow-wave devices [165].

Various methods for solving this and similar waveguide problems are well-known. Here, a conjugate matching method is used, based on the wave impedance. For TM waves, in the z -direction, the wave impedance takes the form:

$$Z_{TM} = -j \frac{\alpha}{\omega \epsilon} \quad (4.3)$$

Assuming a purely reactive surface with no real component, solutions must satisfy the following equation:

$$Z_s = Z_{TM}^* \quad (4.4)$$

This implies the following form of dispersion for the TM surface wave:

$$j \frac{\alpha}{\omega \epsilon} = Z_s \quad (4.5)$$

with similar results holding for TE surface waves:

$$Z_{TE} = j \frac{\omega \mu}{\alpha} \quad (4.6)$$

$$-j \frac{\omega \mu}{\alpha} = Z_s \quad (4.7)$$

Notably, Eq. 4.5 and 4.7 suggest that α is determined by the surface impedance. For real and positive α , this requires Z_s to be inductive in the case of TM surface waves, and capacitive for TE waves. Since most naturally occurring surfaces are inductive, only TM surface waves tend to exist naturally.

4.1.1 Field Components

Additional insight can be had by examining the field components of the surface wave solutions. Again, the solution method is analogous to that of a rectangular waveguide. Note that since the fields can be interpreted as being transverse with respect to either the x or z directions, equations formulated for either propagation in the x or z direction should be valid (with the equations modified evanescent modes as appropriate). For the TM surface wave, the fields are given by the following equations:

$$H_y = \frac{-j\omega\epsilon}{\beta^2} \frac{\partial E_z}{\partial x} \quad (4.8a)$$

$$E_x = \frac{-\alpha}{\beta^2} \frac{\partial E_z}{\partial x} \quad (4.8b)$$

$$H_x = 0 \quad (4.8c)$$

$$E_y = 0 \quad (4.8d)$$

Substituting in the form from Eq. 4.1, this gives solutions for the TM field components:

$$E_z = e^{-j\beta x - \alpha z} \quad (4.9a)$$

$$E_x = \frac{j\alpha}{\beta} E_z \quad (4.9b)$$

$$H_y = \frac{-\omega\epsilon}{\beta} E_z \quad (4.9c)$$

For TE surface waves, the same solution process holds:

$$H_x = \frac{-\alpha}{\beta^2} \frac{\partial H_z}{\partial x} \quad (4.10a)$$

$$E_y = \frac{-j\omega\mu}{\beta^2} \frac{\partial H_z}{\partial x} \quad (4.10b)$$

$$H_y = 0 \quad (4.10c)$$

$$E_x = 0 \quad (4.10d)$$

$$H_z = e^{-j\beta x - \alpha z} \quad (4.11a)$$

$$H_x = \frac{j\alpha}{\beta} H_z \quad (4.11b)$$

$$E_y = \frac{-\omega\mu}{\beta} H_z \quad (4.11c)$$

Looking at the TM field components in Eq. 4.9, consider the polarization of this wave. From Eq. 4.2, we can infer that $\alpha < \beta$, and that the dominant electric field component is E_z . Hence, the TM surface wave is associated with an electric field polarization normal to the surface, especially for loosely bound waves when α is small. For TE waves, Eq. 4.11 suggests that TE waves have the perpendicular polarization, with the electric field component being entirely within the surface plane. These differing polarizations for the two surface wave solutions are illustrated in Fig. 4.1.

4.1.2 PEC and PMC Surfaces

PEC and PMC boundaries are two particularly important instances to consider for understanding TM versus TE surface wave behaviour. Based on the surface impedance definition given by 2.1, a PEC boundary implies $Z_s = 0$, while for a PMC $Z_s = \infty$. Considering first the PEC surface, Eq. 4.5 suggests $\alpha = 0$ for the TM surface wave. In this case, the TM surface wave again approaches a plane wave. For a TE surface wave however, Eq. 4.7 implies that $\alpha = \infty$, causing the field components to be ideally zero. Thus, TE surface waves cannot propagate along a PEC surface. This result can also be inferred by appealing to the field components in Eq. 4.11. The PEC surface can be thought of as shorting out the E_y field component tangential to the surface. This also supports the conclusion that TE surface waves do not exist for typical metallic surfaces.

Similar results hold for the PMC surface, along which a TE surface wave, but not a TM wave, may propagate. The PMC surface can also be thought of as shorting out the tangential H components of the TM wave. Since EM radiation and the associated surface currents that travel along typical metallic structures are comparable to the TM surface wave, being able to realize a PMC surface would allow the suppression of such radiation and currents.

4.2 Corrugated Surface

As an example, consider the corrugated surface. The impedance of the surface can be modeled by assuming TEM parallel plate modes between the corrugations. The surface may thus be assumed to behave similarly to a homogenized surface with an anisotropic impedance

$$Z_{s1} = j\eta \frac{g}{g+t} \tan kd \quad (4.12)$$

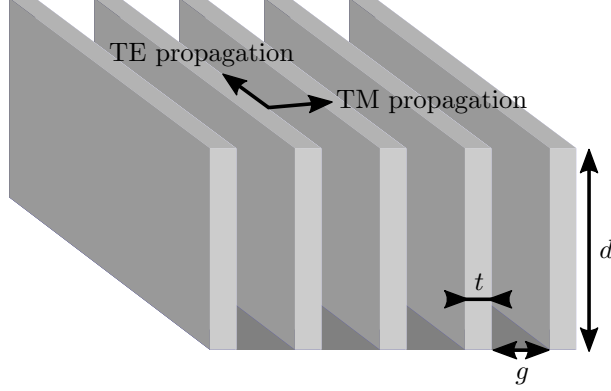


Figure 4.2: Corrugated surface, where d is the corrugation height, g the corrugation width, and t the metallic thickness. Directions of propagation for TM and TE surface waves are marked.

$$Z_{s2} = 0 \quad (4.13)$$

where Z_{s1} and Z_{s2} are the surface impedances as seen by a wave with electric field components respectively perpendicular and parallel to the corrugations, with dimensions as shown in Fig. 4.2, and where k and η are the wave number and wave impedance respectively inside the corrugation. The factor $g/(g+t)$ is a filling factor accounting for the non-zero width t of the metallic walls.

At low frequencies, the surface is inductive and supports a TM surface wave, traveling perpendicular to the corrugations. As the depth approaches $\lambda/4$ however, Z_{s1} approaches infinity, and TM waves are suppressed. Then from the $\lambda/4$ to $\lambda/2$ frequency, the surface is capacitive, and the surface supports only a TE surface wave. The polarization of the TE wave however, is such that the supported TE wave can only propagate parallel to the corrugations, as shown in Fig. 4.2.

4.2.1 Dispersion Diagram

Together, Eq. 4.2, 4.5, and 4.12, predict the propagation constant β for a TM surface wave as a function of frequency (assuming $t = 0$, for ideally thin

metallic walls).

$$\beta = |k \sec kd| \quad (4.14)$$

Though this equation yields solutions between the $\lambda/4$ and $\lambda/2$ frequencies, the field solutions are divergent, and the calculated β values in this range cannot be expected to be physical. Additionally, β approaches infinity as the depth approaches $\lambda/4$. Since this model assumes a homogenized surface, this equation is unphysical for phase beyond 180° per corrugation, and the surface impedance model cannot accurately predict the behaviour of the surface at frequencies sufficiently close to the $\lambda/4$ open-circuit frequency.

The dispersion as predicted from the surface impedance model in Eq. 4.14 is plotted in Fig. 4.3 against eigenmode simulation frequencies for the same structure, designed for a 1 GHz open-circuit frequency, for a corrugation with depth 7.5 cm. The corrugation period was chosen to be 3 cm. The surface impedance model agrees closely with simulation up to where the phase per unit cell approaches 180° . From this frequency up to 1 GHz, the surface impedance model becomes inaccurate, and the corrugation shows a bandgap not predicted for a homogenized surface. In the capacitive surface region from 1 GHz to 2 GHz, the surface becomes a leaky-wave structure, with a phase per unit cell less than that of free space. Inside this frequency band, currents on the surface are expected to be attenuated as they radiate power away from the surface. Above 2 GHz, the surface becomes inductive, and again supports a TM surface wave.

4.2.2 Soft Surface Property

One unique property of the corrugated surface compared to similar high-impedance surfaces is its anisotropy. Though the surface supports TE waves in the capacitive region above resonance, these may only be excited in the direction parallel to the corrugations. Perpendicular to the corrugations, the TE wave is

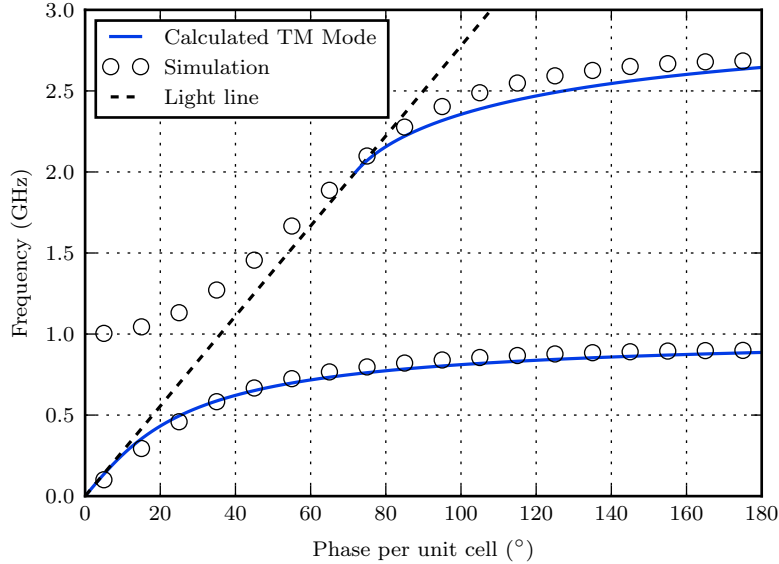


Figure 4.3: Dispersion diagram of the corrugated surface with depth of 7.5 cm, with a period of 3 cm.

polarized such that it sees the effective impedance $Z_{s2} = 0$ (i.e. a short circuit), and is effectively cutoff. At the open-circuit frequency, for TM waves traveling perpendicular to the corrugation, the effective surface impedance is $Z_{s1} = \infty$, TM waves are similarly cutoff. Hence, as a result of the surface anisotropy, both TM- and TE-polarized waves are cutoff perpendicular to the excitation. This is the so-called “soft” surface property, a key modern insight by the late Per-Simon Kildal [120]. For a source at the origin, the soft surface is realized by ensuring that radiation from the source always travels perpendicularly to the corrugations, suggesting a concentric cylindrical arrangement. This arrangement is the choke-ring shield, which is a common structure for GPS antennas. This structure is explored in more depth in Chap. 5, and results for a measured choke ring antenna are shown in Chap. 6.

4.3 Dipole Above an Impedance Surface

The previous section discussed the properties of surface wave solutions, and their interaction with different reactive surfaces. A major limitation however, is that this fails to show how surface waves may be excited or suppressed in a problem involving a realistic source. To solve this, we consider the problem of a dipole source above an impedance surface. This problem follows the same general method as the Sommerfeld problem for a dipole above a half-space. The process is to decompose a dipole source into a basis of cylindrical wave components. These are the same cylindrical wave solutions as a cylindrical waveguide, and form a complete orthonormal basis in which the fields of a source may be decomposed. In contrast to the cylindrical waveguide problem however, in the absence of PEC boundaries, the cylindrical waves form a continuous spectrum of modes, rather than a discrete set. Though discussion in the previous section was limited to reactive impedance surfaces, this solution method generalizes to surfaces with real impedances, and can be used to analyze a dipole above high-impedance surface absorbers, or generally any multi-layer absorber that has an equivalent circuit representation.

4.3.1 Vertical Dipole

We start by considering an infinitesimal point current source $\mathbf{J}(\mathbf{r}) = \hat{z}\delta(\mathbf{r})$ centered at the origin. This current results in a z -directed magnetic field of identically zero, and a z -directed electric field as given by the expression [166]:

$$E_z(\mathbf{r}) = -j\omega\mu_0 \left(1 + \frac{1}{k^2} \frac{\partial^2}{\partial z^2} \right) \frac{e^{-jkr}}{4\pi r} \quad (4.15)$$

suggesting that this is a TM wave, relative to the z direction. Since the tangential field components can be derived from the z -directed fields, it is sufficient to find a solution in terms of the E_z component for now. To rewrite this in

terms of cylindrical wave components propagating in the z direction, we can use the Sommerfeld identity

$$\frac{e^{-jk|\mathbf{r}-\mathbf{r}'|}}{|\mathbf{r}-\mathbf{r}'|} = \int_0^\infty \frac{k_\rho}{jk_z} J_0(k_\rho|\rho-\rho'|) e^{-jk|z-z'|} dk_\rho \quad (4.16)$$

resulting in the following expression:

$$E_z(\mathbf{r}) = -\frac{1}{4\pi\omega\epsilon_0} \int_0^\infty \frac{k_\rho^3}{k_z} J_0(k_\rho\rho) e^{-jk_z|z|} dk_\rho \quad (4.17)$$

The preceding analysis is for a vertical dipole in free space. To satisfy the impedance boundary condition, it is necessary to include additional scattered field terms. For an incident TM cylindrical wave at the plane of the impedance boundary, these take the form of a reflected wave with the reflection coefficient:

$$R_{TM} = \frac{Z_s - Z_{TM}}{Z_s + Z_{TM}} \quad (4.18)$$

where Z_{TM} is the wave impedance for a TM wave.

$$Z_{TM} = \frac{k_z}{\omega\epsilon} \quad (4.19)$$

For a dipole at a length l above the surface, this reflection coefficient is transformed by an effective propagation length.

$$R_{TM} = \frac{Z_s - Z_{TM}}{Z_s + Z_{TM}} e^{-2jk_z l} \quad (4.20)$$

Using this, we arrive at an expression for the scattered field.

$$E_z^{\text{ref}}(\mathbf{r}) = \frac{1}{4\pi\omega\epsilon_0} \int_0^\infty \frac{k_\rho^3}{k_z} J_0(k_\rho\rho) R_{TM} e^{-jk_z z} dk_\rho \quad (4.21)$$

Note that due to the reversed direction of propagation, $E_z^{\text{ref}}(\mathbf{r})$ gains an additional negative sign not accounted for in the usual reflection coefficient R_{TM} .

For $k_\rho > k$, k_z becomes imaginary, and the cylindrical wave becomes evanescent. Let us represent the attenuation constant as α .

$$\alpha = jk_z = \sqrt{k_\rho^2 - k^2} \quad , \quad k_\rho > k \quad (4.22)$$

Consider R_{TM} from Eq. 4.20. Combining it with Eq. 4.19 and 4.22, we arrive at an expression for the R_{TM} in terms of α .

$$R_{TM} = \frac{Z_s + \frac{j\alpha}{\omega\epsilon}}{Z_s - \frac{j\alpha}{\omega\epsilon}} e^{-2jk_z l} \quad (4.23)$$

This form of R_{TM} has a pole at $Z_s = j\alpha/\omega\epsilon$, which is the same as Eq. 4.5 for TM surface waves. This pole is the connection between the earlier surface wave solutions and the more general solution presented here. Sommerfeld's original analysis of the problem included an approximate evaluation of an integral of this type, which showed a decomposition of the fields into a radiating component, a near-field component, as well an outgoing surface wave [167, 168]. Note that while this analysis uses the term TM to refer to fields transverse to the z direction, this is consistent with the earlier usage of TM for surface wave solutions.

For a TM cylindrical mode propagating in the positive z direction, the field components are given by the following equations:

$$E_\rho = \frac{-jk_z}{k_\rho^2} \frac{\partial E_z}{\partial \rho} \quad (4.24a)$$

$$E_\phi = \frac{-jk_z}{k_\rho^2 \rho} \frac{\partial E_z}{\partial \phi} \quad (4.24b)$$

$$H_\rho = \frac{j\omega\epsilon}{k_\rho^2 \rho} \frac{\partial E_z}{\partial \phi} \quad (4.24c)$$

$$H_\phi = \frac{-j\omega\epsilon}{k_\rho^2} \frac{\partial E_z}{\partial \rho} \quad (4.24d)$$

which when evaluated using E_z^{ref} according to Eq. 4.21, gives the complete scattered field components as integral expressions:

$$E_\rho^{\text{ref}} = \frac{j}{4\pi\omega\epsilon} \int_0^\infty k_\rho^2 J_1(k_\rho\rho) R_{TM} e^{-jk_z z} dk_\rho \quad (4.25a)$$

$$E_\phi^{\text{ref}} = 0 \quad (4.25b)$$

$$H_\rho^{\text{ref}} = 0 \quad (4.25c)$$

$$H_\phi^{\text{ref}} = \frac{j}{4\pi} \int_0^\infty \frac{k_\rho^2}{k_z} J_1(k_\rho\rho) R_{TM} e^{-jk_z z} dk_\rho \quad (4.25d)$$

Using Eq. 4.21 and 4.25a, electric fields for a vertical dipole above various surfaces were computed. These are shown in Fig. 4.4, and confirm many of the results from the discussion on surface waves. For a dipole above a matched absorber, a resistive surface is also considered. In particular, we see the excitation of a closely-bound surface wave for an inductive surface, as well as the mitigation of radiation along the surface for PMC, capacitive, and resistive surfaces. For the capacitive and resistive surfaces, the reduction of radiation is controlled by the magnitude of the impedance, with higher impedances approaching the PMC case. Comparing the resistive and capacitive surfaces, the capacitive surface tends to redirect power away from the surface, while the resistive surface instead absorbs power through ohmic loss, resulting in a lower field magnitude.

4.3.2 Horizontal Dipole

The method for solving a horizontal dipole above an impedance surface tends to be very similar to that of a vertical dipole. For brevity, the full solution will not be explored. A key difference however, is that the horizontal dipole has both E_z and H_z components, and thus both TM and TE components. For an

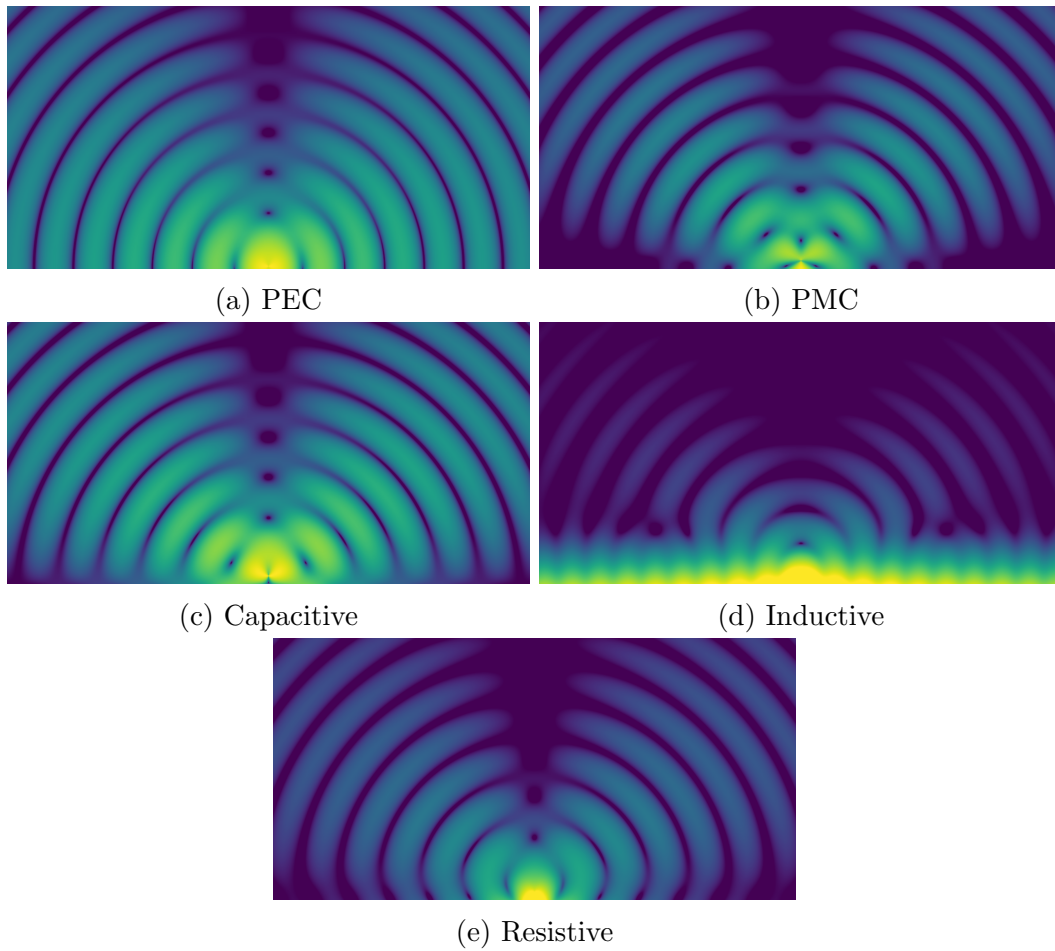


Figure 4.4: Electric field magnitudes for an infinitesimal dipole above various surfaces. The dipole is $\lambda/10$ above the surface in each case. For the capacitive, inductive, and resistive surfaces, a surface impedance of magnitude $377\ \Omega$ was used.

x -directed dipole, these are given by the expressions [166]

$$E_z(\mathbf{r}) = \frac{1}{j\omega\epsilon} \frac{\partial^2}{\partial x \partial z} \frac{e^{-jk_r r}}{4\pi r} \quad (4.26)$$

$$H_z(\mathbf{r}) = -\frac{\partial}{\partial y} \frac{e^{-jk_r r}}{4\pi r} \quad (4.27)$$

Evaluating these using the Sommerfeld identity (Eq. 4.16), we get expressions in terms of cylindrical waves:

$$E_z(\mathbf{r}) = \pm \frac{j}{4\pi\omega\epsilon} \cos \phi \int_0^\infty k_\rho^2 J_1(k_\rho \rho) e^{-jk_z |z|} dk_\rho \quad (4.28)$$

$$H_z(\mathbf{r}) = -\frac{j}{4\pi} \sin \phi \int_0^\infty \frac{k_\rho^2}{k_z} J_1(k_\rho \rho) e^{-jk_z |z|} dk_\rho \quad (4.29)$$

where the \pm evaluates as $-$ for $z > 0$, and $+$ for $z < 0$.

One important aspect of this decomposition is the angular variation of excitation for the TE compared to TM components. In the x - z plane—the antenna’s E plane—only TM modes are excited, and a PMC surface is ideal for suppressing radiation along the surface. Similarly, a PEC surface is ideal for suppressing the TE radiation in the antenna’s H plane. This supports the use of an anisotropic soft surface to achieve both conditions simultaneously. Though we came to this conclusion earlier by appealing to analogy with surface waves, here we show that the same conclusion holds for more realistic dipole sources.

Chapter 5

Choke Ring Simulation and Analysis

In the previous chapters, we have considered theory and methods applicable to a large variety of shielding structures. In this chapter, these concepts are put together to analyze a choke-ring shield. From this, design guidelines are developed, and these results tested parametrically via simulation.

Choke rings are a type of shielding structure, common in GPS. In GPS, the major source of multipath signals is scattering off of ground obstacles such as buildings. As a result, multipath GPS signals tend to be received at low angle, near the horizon. By altering the propagation of waves along or near their corrugated surface, choke rings achieve patterns with a sharp roll-off near the horizon, reducing the reception of these signals, and hence mitigating multipath [13, 162, 169, 170, 171]. To do this, choke rings use a radially periodic set of concentric rings, creating a corrugated surface in a cylindrical geometry. As discussed in Chap. 4, the corrugated surface achieves an open-circuit condition through its $\lambda/4$ resonant depth. Above this frequency however, the surface acts like a leaky-wave structure, and effectively attenuates currents that travel along the surface, up to the $\lambda/2$ resonance. It is this octave of bandwidth makes choke rings an attractive shielding structure for consideration in GPR or other

pulsed time-domain applications. Due to its anisotropy, the corrugated surface is able to effectively block both TM- and TE- polarized waves along the surface, in all directions. As a result of this, choke ring radiation patterns also tend to be circularly symmetric [126], which is advantageous for RHCP vs. LHCP discrimination.

5.1 Choke Ring Design

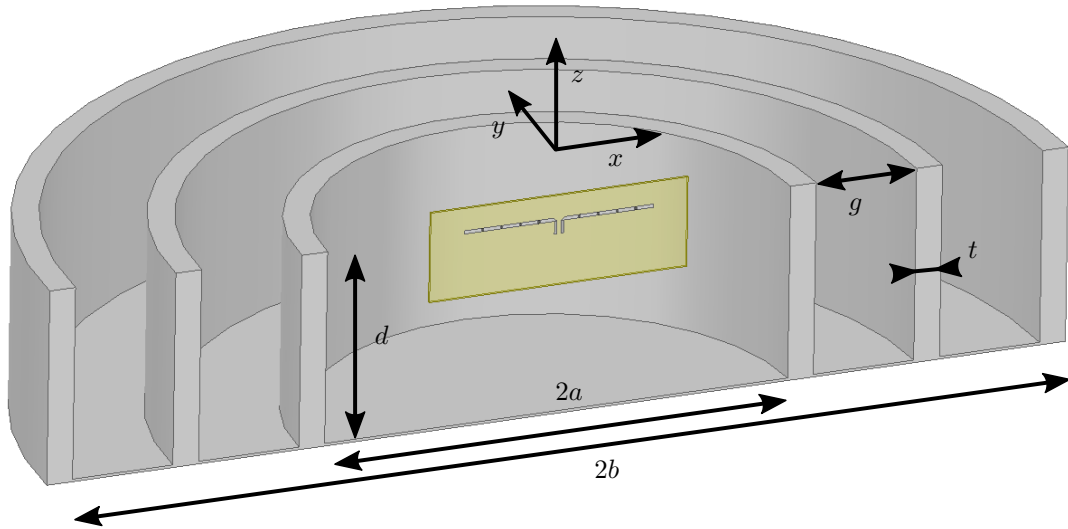


Figure 5.1: Cross-section of a typical choke-ring structure backing a printed dipole antenna, where d is the choke-ring height, g the corrugation width, t the ring thickness, a the cavity radius, and b the total radius.

The mechanisms governing choke-ring operation are well-established, with patents on choke-ring antenna structures filed as early as 1961 [160], and clear precursors in corrugated structures studied as early as the 1940's. As discussed previously, the corrugated surface may be assumed to behave similarly to a homogenized surface with an anisotropic impedance

$$Z_{s1} = j\eta \frac{g}{g+t} \tan kd \quad (5.1)$$

$$Z_{s2} = 0 \tag{5.2}$$

where Z_{s1} and Z_{s2} are the surface impedances as seen by a wave with polarization respectively perpendicular and parallel to the corrugations, k and η are the wave number and wave impedance respectively inside the corrugation, d is the corrugation height, t is the width of the metallic wall, and g is the width of the corrugation itself. These are shown in Fig. 5.1. The factor $g/(g + t)$ is a filling factor accounting for the non-zero width t of the metallic walls. As shown in Chap. 4, the surface impedance Z_{s1} is related to the rate of decay of currents along the surface. Near the $\lambda/4$ resonance, the impedance is ideally infinite, and the filling factor is fairly irrelevant to the design. Away from $\lambda/4$ frequency up to $\lambda/2$, however, the filling factor has a significant effect on the radiation properties of the choke ring. Hence, it is desirable to maximize the filling factor, with as small a wall width t as mechanically feasible.

Notice that in this homogenized impedance view, neither the periodicity of the corrugations nor the number of rings affects the performance of the structure. Rather, the overall radial size of the structure b is the relevant design variable, with a trade-off between compactness and pattern-shaping ability of the choke-ring shield. This is subject to the constraint that the periodicity of the corrugations is sufficiently small, such that the homogenized impedance accurately represents the surface. Nevertheless, previously presented designs with fairly large corrugations work well (as wide as around $\lambda/5$ at the open-circuit frequency), even if the homogenized impedance view does not strictly hold over the entire bandwidth [13, 125].

5.1.1 Coaxial Modes

The surface impedance view is an approximation that replaces the fields inside the corrugation with an equivalent boundary condition, assuming a parallel plate mode between the metallic corrugations. In the case of the choke-ring

structure, the fields are more accurately described as coaxial modes. Though the lowest frequency coaxial mode is usually the TEM mode, due to the symmetrical excitation, this mode is not excited. Rather, the lowest relevant mode is the TE₁₁ coaxial mode, which exhibits a cutoff frequency. Though this can be computed analytically in terms of Bessel function solutions by solving the boundary-value problem, a reasonable approximation is made by instead using parallel plate modes subject to periodic boundary conditions. For a corrugation with average radius r , this cutoff frequency is given by the equation [172]:

$$f_c = \frac{c}{2\pi r}$$

and achieves the open-circuit resonance at the frequency given by the equation:

$$f = c\sqrt{\left(\frac{1}{2\pi r}\right)^2 + \left(\frac{1}{4d}\right)^2}$$

This cutoff has the effect of shifting the resonance upward in frequency compared to rectangular corrugations, especially so as the radius r decreases. For example, a shift of 10% or more is seen by corrugations with r less than $1.39d$.

5.2 Cavity Absorber

As a result of the increasing cutoff frequency of the coaxial TE₁₁ mode as radius decreases, corrugations near the origin of the choke-ring shield are impractical. Instead, choke-ring corrugations are applied around a central cavity, which backs the antenna. Since choke-ring shields can be understood as an alteration of this simpler cavity shield, cavity effects play a critical role in the choke-ring shield's performance. For the purpose of studying the effects of the choke ring corrugation, it can be desirable to isolate its effects from the cavity itself. For this, we consider absorber-loaded cavities. To reduce reflection, we use an

absorber that is perfectly matched at normal incidence in free space, with equal relative permeability and permittivity of 3.5, and equal loss tangents of 1. This is very similar to a PML, and we refer to it as a quasi-PML. Compared to a PML, the quasi-PML has some reflection at angles away from normal incidence, but has the advantage of being isotropic, and is more comparable to realistic fabricable absorbers.

5.3 Parametric Studies

To confirm the results of Sec. 5.1, and establish particular design guidelines, a number of parametric studies are performed. For this, we establish base designs for the cavity and choke-ring shields, with cross-sectional dimensions as shown in Fig. 5.2. The following parametric studies are all variations of these designs, and use these dimensions unless otherwise stated. For studies considering the effects of the choke ring in absence of cavity effects, the quasi-PML is loaded into the central cavity. These designs are based on a previously published choke ring design[125], and are scaled for a 1 GHz design frequency. The choke-ring shield is backing a $\lambda/4$ small printed dipole, loaded with eight equally-spaced 50Ω resistors.

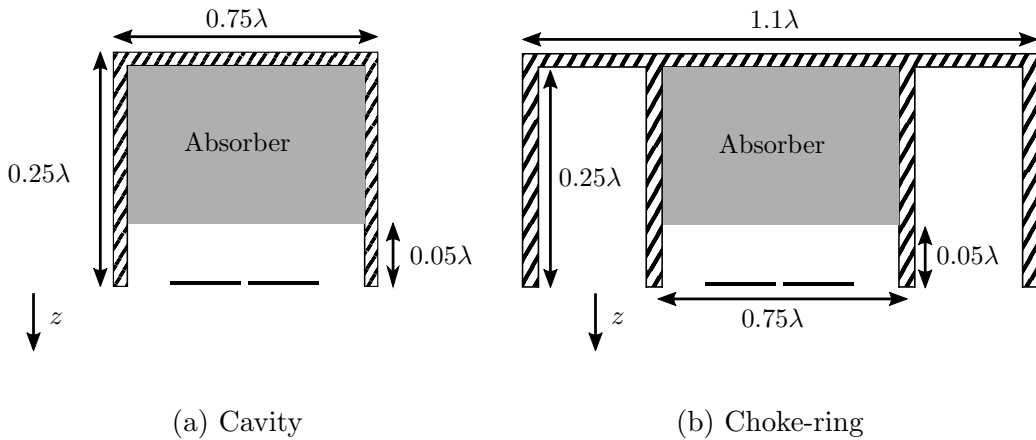


Figure 5.2: Cross sections of the cylindrical cavity and choke-ring structures, where λ is the free-space wavelength at the $\lambda/4$ design frequency [1].

5.3.1 Number of Rings

In the surface impedance view, different structures with the same surface impedance should behave identically. As a result, the particular number of rings used in the choke-ring shield should not affect its performance, given that the structures are otherwise identical. To confirm this, the RFP of choke-ring shields with 2 to 5 rings are compared, with constant cavity radius a and total radius b . In all cases, ideally thin metallic sheets with thickness $t = 0$ were used. These results are shown in Fig. 5.3. Except for some variation around 1 GHz, the RFP responses of these different choke rings are virtually identical. From the dispersion diagram of corrugated surfaces in Chapter 4, we know that below the open circuit frequency, the phase per unit cell approaches 180° , and the surface impedance approximation fails. Additionally, due to the varying corrugation radii when multiple corrugations are present, the open-circuit frequency resonance is shifted by varying amounts for each corrugation, significantly increasing the complexity of the response. Thus both performance-wise and practically, for moderately sized choke-ring shields, there is very little reason to use more than a single corrugation (two rings).

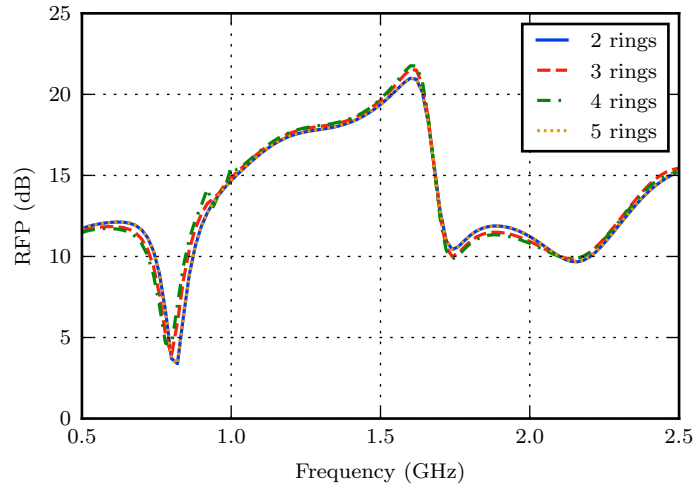


Figure 5.3: RFP for different numbers of choke rings.

5.3.2 Total Size

To show the effect of the overall size on shielding, as well as the benefit of choking shielding, RFP as a function of size at a single frequency is compared for choke and cavity shields, both with and without absorbers. To increase the choke ring's size while keeping the central cavity radius a constant, the choke ring was varied by adding additional rings, with a corrugation width g of 1 cm. Though this could also be achieved by varying the corrugation width g , it is suspected that for very large corrugation widths, the choke ring would start deviating from its expected behaviour under the surface impedance model. Since these rings have an open-circuit frequency somewhat above 1 GHz as a result of the cutoff frequency of the coaxial TE_{11} mode in the corrugations, the different structures are compared at 1.1 GHz, ensuring a comparison above the open-circuit frequency of any particular corrugation.

These results are shown in Fig. 5.4. Generally, all the examined structures show a fairly linear trend in RFP. The cavity without the absorber is the main exception, as a result of the TM_{11} mode effect. The TM_{11} resonance varies with $f_{c, TM_{11}}$ as a function of radial size, showing a resonance depending on both size and frequency. Though the TM_{11} resonance is also present for the choke ring, since the cavity radius a is kept constant, it is not visible in Fig. 5.4. At this particular frequency, both the TM_{11} resonance and choke ring corrugation enhance shielding, and the unloaded choke ring has the best shielding over most sizes. To assess the choke ring shielding in absence of the TM_{11} mode, consider the choke ring versus cavity with the absorber. The absorber-loaded choke shield shows a substantial improvement over the similar absorber-loaded cavity, with the difference growing more prominent for larger radial sizes.

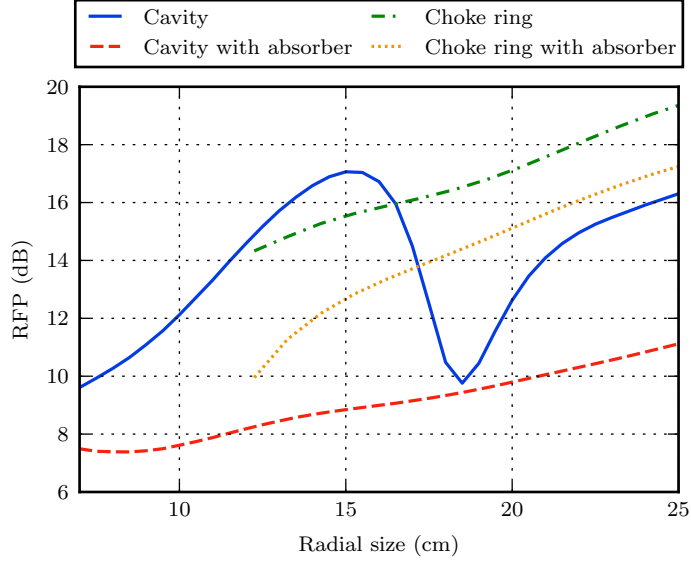


Figure 5.4: RFP versus radial size, for the different choke or cavity shields with or without absorber

5.3.3 Corrugation Width

From the results of Chap. 4, it is expected that the surface impedance Z_{s1} controls the shielding ability of the choke ring for waves possessing a TM polarization, excited primarily in the E plane of the antenna, while leaving the TE polarization unaffected. At the open circuit frequency, Z_{s1} approaches infinity, and is expected to have ideal performance. Away from the open-circuit frequency however, the shielding ability is affected by the filling factor $g/(g+t)$. In this study, radiation patterns at 1.4 GHz—a frequency sufficiently above the 1 GHz open-circuit frequency—are compared for the absorber-loaded choke ring as the filling factor $g/(g+t)$ is modified. The metallic thickness t is kept equal between the inner and outer ring, and the overall size and cavity radius are kept constant. These results are shown in Fig. 5.5.

It can be seen that modifying the filling factor has a significant in the E plane, while leaving the H plane relatively unchanged. As the filling factor increases, radiation is reduced at all angles, but especially to the back of the

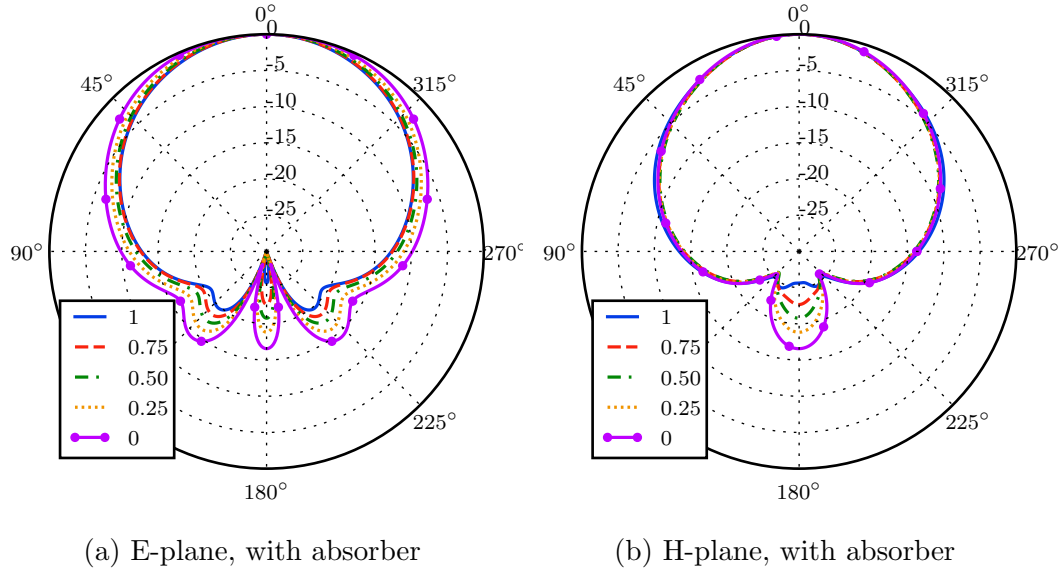


Figure 5.5: Normalized E- and H-plane patterns of the choke ring with absorber at 1.4 GHz, for various filling factors.

E plane. This is consistent with the interpretation of currents on the back and sides of the choke shield as TM-polarized waves, excited primarily in the E plane, and affected by Z_{s1} rather than Z_{s2} . In contrast, radiation along the H plane effectively sees the Z_{s2} impedance, which is perfectly cutoff for the TE polarization excited in the H plane. Since the backlobe is produced primarily by TM-polarized waves, and the backlobe is common to both planes, we similarly see the backlobe reduction in the H plane. This reduction in backlobe and E-plane radiation supports the conclusion that the filling factor should be maximized if possible, suggesting ideally thin metallic thickness t is preferable.

Chapter 6

Choke-Ring Shield for GPR

In the previous chapter, we applied the theory of soft surfaces, impedance surfaces, and cavity modes to establish design guidelines for choke-ring shields. Here, we look at the fabrication and measurement of a choke-ring shield backing a small dipole. The choke-ring shield is intriguing as a shield for GPR largely due to its octave bandwidth, which is larger than other comparable EBG bandwidths. To reduce effects such as ringing in the cavity, we consider absorber-loaded cavities. Thus, a total of four designs—cavity and choke ring shields with and without absorbers—are fabricated and measured.

In the context of GPR, we are primarily interested in the performance of the shield in response to a pulsed excitation, and this chapter also considers issues surrounding time-domain metrics for choke ring assessment. Due to the band-limited frequency-domain measurements used when characterizing the choke ring, we consider the recreation of broadband time-domain metrics from frequency domain measurements.

When considering practical GPR antenna design, the antenna is operated in close proximity to the ground, and the additional complexities of ground-coupling and near-field interactions must be taken into account. These considerations however, are beyond the scope of this work. Hence, only the far-field response of the antenna structure as embedded in an air dielectric is consid-

ered, which is the first phase towards developing a design suitable for real deployments.

6.1 Design

6.1.1 Choke Rings

We start by establishing the design bandwidth from 1 GHz to 2 GHz. This choice is motivated by measurement constraints as well as prototype size, and could in general be scaled to any frequency. Hence, we establish the $\lambda/4$ and $\lambda/2$ resonance frequencies, respectively, fixing the height of the choke-ring structure d at 7.5 cm. From the results of Chap. 5, we know that for moderately sized designs, it is usually preferable to use fewer rings. Thus, we consider a two ring design. To set the cavity radius, the primary constraint is a value large enough such that the TE_{11} cavity mode cutoff frequency is low enough for energy to penetrate into the cavity over the operation bandwidth. Though the overall choke ring size is a trade-off between shielding ability and compactness, the choke ring sees a larger benefit compared to simpler shield structures for somewhat larger sizes. With these considerations in mind, we find the design established in Chap. 5, as shown in Fig. 5.2 to be sufficient. This design also works reasonably well somewhat outside the design bandwidth of 1 GHz to 2 GHz, and we can reasonably excite the choke-ring shield with a pulse in the range of 0.75 GHz to 2.5 GHz, for a somewhat larger bandwidth of 1.7 octaves.

6.1.2 Small Dipole Antenna

Small dipole antennas are common in impulse GPR thanks to their simplicity, low-profile construction, and favorable dispersion. Here we use the same small $\lambda/4$ resistively loaded dipole introduced in Chap. 3. For design around 1 GHz, this dipole is 7.5 cm long. For practical fabrication using a dielectric, a

strip dipole of width 4 mm is chosen. Though resistive-loading profiles for GPR antennas are a well-studied topic [173, 174], for such a small dipole, the particular resistive loading profile chosen has minimal effect on its performance, and the earlier choice of four equally-spaced 50- Ω resistors on each antenna arm is reasonable. Such a small dipole radiates primarily through its dipole moment, with a second-derivative response in time [175]. The result of this second-derivative radiated response is that given an input pulse in the chosen bandwidth, the radiated pulse tends to be slightly broader, and with additional zero crossings, but otherwise very similar in shape to the input pulse.

6.1.3 Absorber

To model the absorber in the cavity and choke structures, a three-layer model of 6 cm total thickness with conductive loss is used. This is intended to mimic the absorber ultimately used in experiment, which is the Eccosorb AN-77 manufactured by Emerson and Cuming. Because material parameters of the Eccosorb AN-77 are unknown, the simulation absorber model uses a dielectric constant of $\epsilon_r = 1.6$ based on previous characterization of the similar AN-74 absorber [93], while otherwise choosing conductivity values to achieve wideband matching in the given frequency range. The chosen electrical properties are given in Table 6.1. Fig. 6.1 compares the excited and radiated pulses for the cavity structures with and without this absorber. The additional reflection and ringing introduced by the cavity shield are evidently suppressed through the inclusion of the absorber.

6.2 Simulation & Analysis

In order to establish the values of both the cavity absorber and choke ring, four cases were simulated: the choke-ring and cavity structures, each both with and without the absorber. By comparing these four cases, effects partic-

ular to either the central cavity or the choke-ring corrugation can be identified separately. Time-domain simulations were done using CST Microwave Studio, while frequency-domain simulations were performed in Ansys HFSS. To evaluate the time-domain performance, we consider the radiated electric-field intensity at boresight versus time, in the far-field, 200 cm (6.6λ at 1 GHz) away from the antenna. Over the design bandwidth, the antenna impedance varies from around 200Ω to 400Ω . The port impedance was chosen to be 200Ω in all cases. This particular choice of port impedance was motivated by the availability of 4:1 transformers that can match the antennas to a $50\text{-}\Omega$ generator.

As a result of the limited frequency range of the measured time-domain response, the measurement process acts like an effective band-pass filter on the input pulse. For input pulses that have power outside of the measurement bandwidth, this will introduce ringing or time side-lobes that can obscure the properties of the antenna system itself. To mitigate this effect, we choose an input pulse based on the band-limited Kaiser window function in the stated frequency range of 0.75 GHz to 2.5 GHz. The Kaiser window is commonly used in digital-signal applications, for its optimized side-lobe-level reduction for a given main-lobe width (equivalently, ringing and pulse width), which is controlled by the parameter β . We find $\beta = 6$ to be a reasonable choice, and the corresponding Kaiser pulse is shown in Fig. 6.1. To more easily compare the different degrees of ringing and clutter in the late time, this work also generally presents the envelope of the radiated pulse, calculated using a Hilbert transform. The Kaiser pulse other signal processing details are further discussed in App. A.

To more easily assess the shielding ability of the cavity and choke-ring structures over the wide bandwidth, we use the RFP metric introduced in Chap. 3, which summarizes the antennas' performance as a function of frequency. As a function of frequency, the RFP is useful for diagnosing effects that occur at a single frequency. Looking at the RFP for the unloaded cavity structure (green

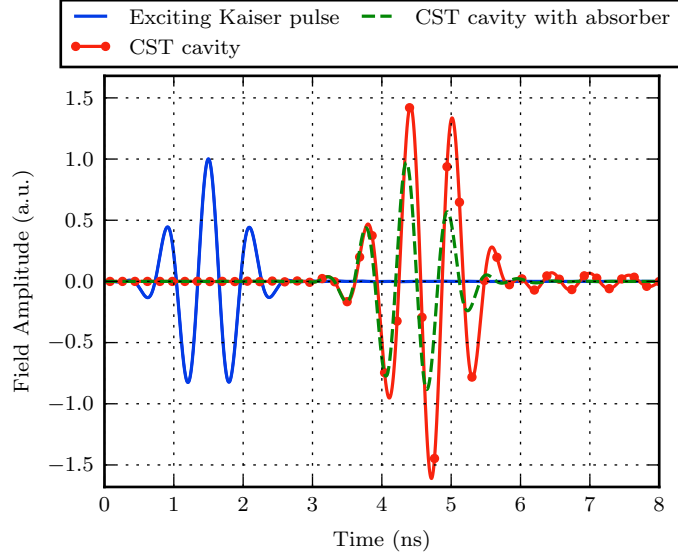


Figure 6.1: Exciting Kaiser pulse and simulated far-field radiated response of the cavity-backed antenna, with and without the absorber. The two radiated pulses use the same normalization factor such that amplitudes can be meaningfully compared.

| Layer | Conductivity (S/m) | Real Relative Permittivity |
|-------|--------------------|----------------------------|
| 1 | 0.025 | 1.6 |
| 2 | 0.16 | 1.6 |
| 3 | 0.26 | 1.6 |

Table 6.1: Conductivity and permittivity values for each of the layers in the absorber simulation model. Each layer is 2 cm thick.

dash-dot curve) in Fig. 6.2, a dip in RFP at 1.74 GHz can be observed where the cavity’s shielding ability is dramatically impaired, due to the excitation of the TM_{11} mode in the cavity. Inclusion of the absorber in the cavity (blue solid curve) has a corresponding effect on the RFP, suppressing the resonant dip and smoothing out the shielding ability of the cavity, while retaining a substantial RFP over the entire frequency range.

The other major visible feature in the RFP is a large resonant dip at roughly 0.8 GHz introduced by the choke ring (yellow dotted and red dashed curves). Though the choke ring improves the pattern over the majority of the frequency

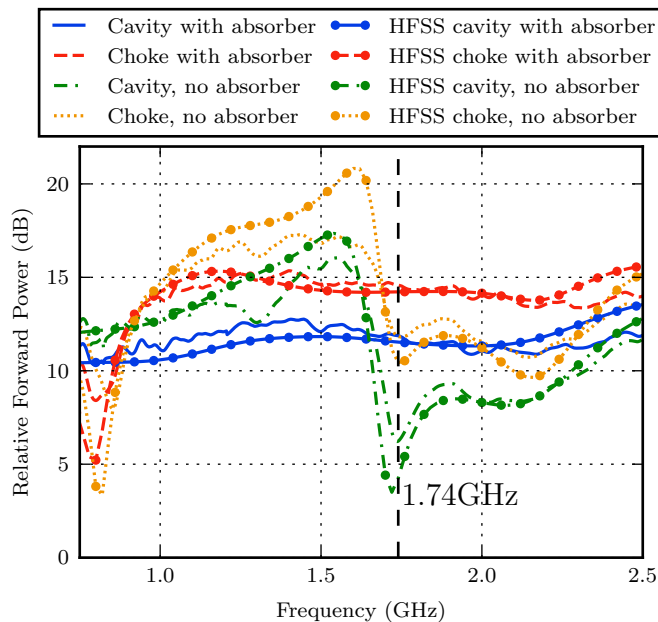


Figure 6.2: Measured vs. simulated RFP, comparing the simple cavity to choke-ring shields, with and without the absorber.

band, it has an adverse effect on the antenna pattern at 0.8 GHz compared to the cavity shields. At this frequency, the choke ring is strongly inductive and supports a closely bound surface-wave mode, excitation of which enhances transmission to the back of the structure. This enhancement to back-radiation for choke-ring designs operating inductively has been noted in previous work [13]. However, the band-limited Kaiser pulse used in this work has low power at this frequency, and so the choke-ring resonance is not visible in the time-domain response. This resonant dip is both a function of the choke-ring height d and width g . Increasing the width tends to shift this frequency downward, enhancing the effective bandwidth of the choke-ring structure to be slightly below the 1 GHz design frequency.

Due to the wideband impulses used to feed GPR antennas, and the prevalence of measurements in the time rather than frequency domain, single-frequency radiation patterns are often of little practical use for evaluating GPR antennas.

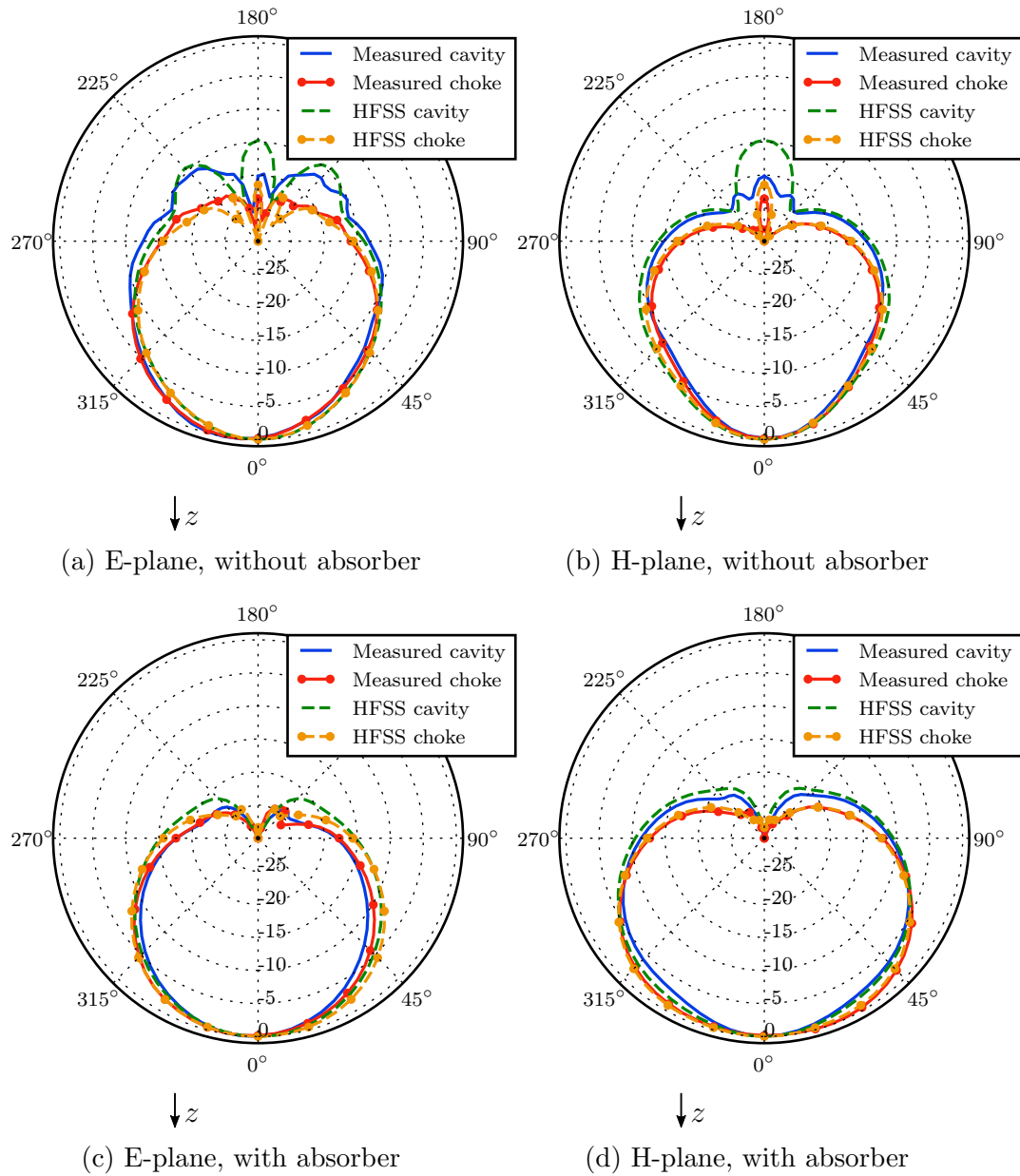


Figure 6.3: Normalized measured and simulated averaged E- and H-plane patterns of cavity and choke structures for a Kaiser exciting pulse, as determined by (6.2).

One way of evaluating a wideband antenna is using its time-averaged radiation patterns. In contrast to the RFP, which summarizes a pattern at a particular frequency, time-averaged patterns consider the entire frequency spectrum, and may be defined as follows [10]:

$$\overline{G}(\theta, \phi) = \frac{4\pi \int U(\theta, \phi, t) dt}{\int P_{acc}(t) dt} \quad (6.1)$$

where U is the time-dependent radiation intensity [W/sr], and P_{acc} is the power as accepted by the antenna. This definition is similar to previously defined energy patterns [176, 177], but normalized to the energy of the input pulse. It can be easily shown that, reformulated in the frequency domain, (6.1) is equivalent to a frequency-averaged radiation pattern, as weighted by the frequency content of the input pulse

$$\overline{G}(\theta, \phi) = \frac{\int G(\theta, \phi, \omega) P_{acc}(\omega) d\omega}{\int P_{acc}(\omega) d\omega} \quad (6.2)$$

where G is the usual gain. Note that this averaged pattern is a function of the input pulse spectrum accepted by the antenna. The averaged patterns calculated using the Kaiser pulse for the various studied cases are shown in Fig. 6.3, from which it is evident that the choke rings have the desired pattern-shaping effect over the design bandwidth. Inclusion of the choke ring either with or without the absorber has the effect of reducing back-lobes, as well as radiation along the horizon, and to the back of the structure at other angles, resulting in an RFP enhancement of 3–5 dB over the cavity alone. The inclusion of the absorber has a more significant effect on pattern shape than the choke ring, though their combination has the greatest pattern-shaping ability, eliminating the back-lobe entirely.

These averaged patterns tend to reflect prominent features that are visible in the RFP over the chosen frequency range. For example, the large back-lobes for the cavity with neither absorber nor choke ring are largely due to the TM_{11}

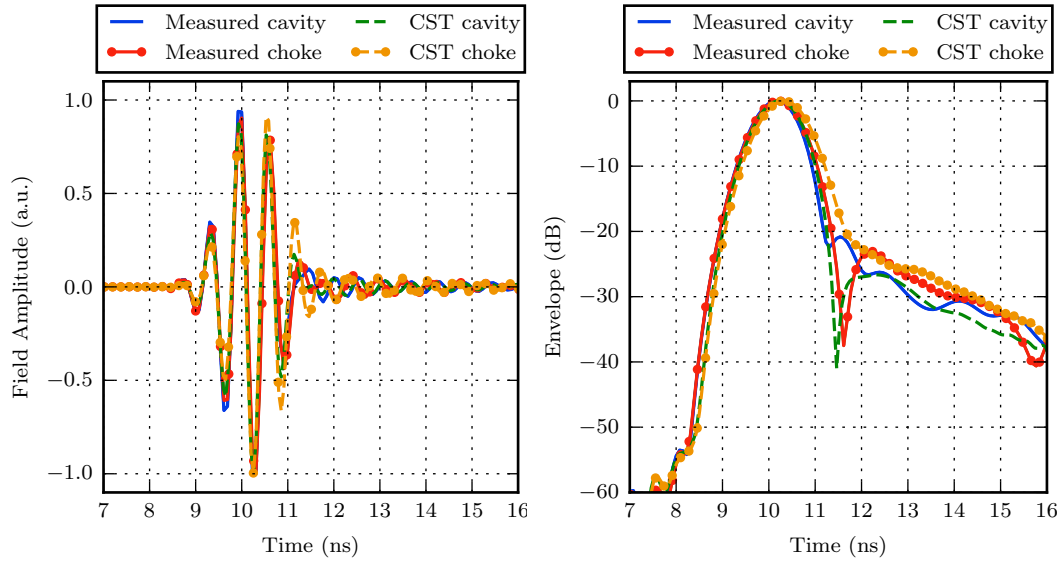
resonance present at 1.74 GHz, which is a major mechanism for radiation to the back in this bandwidth. We also notice contributions of a $\lambda/2$ resonance in the cavity TE_{11} mode to the H-plane pattern, visible in Fig. 6.3b for the case without the absorber. At this frequency, unloaded cavity produces a high-gain main-lobe and multiple side-lobes, resulting in a spade-like shape in the averaged pattern.

Fig. 6.4 compares the radiated pulses of all four simulated structures. The late-time ringing due to the unloaded cavity, shown in Fig. 6.4b, has an exponential decay of 3 dB/ns, suggesting a cavity resonance at 1.74 GHz with quality factor $Q = 15.6$. Notice also from Figs. 6.4b and 6.4d that inclusion of the choke ring has a minor impact on the time-domain performance.

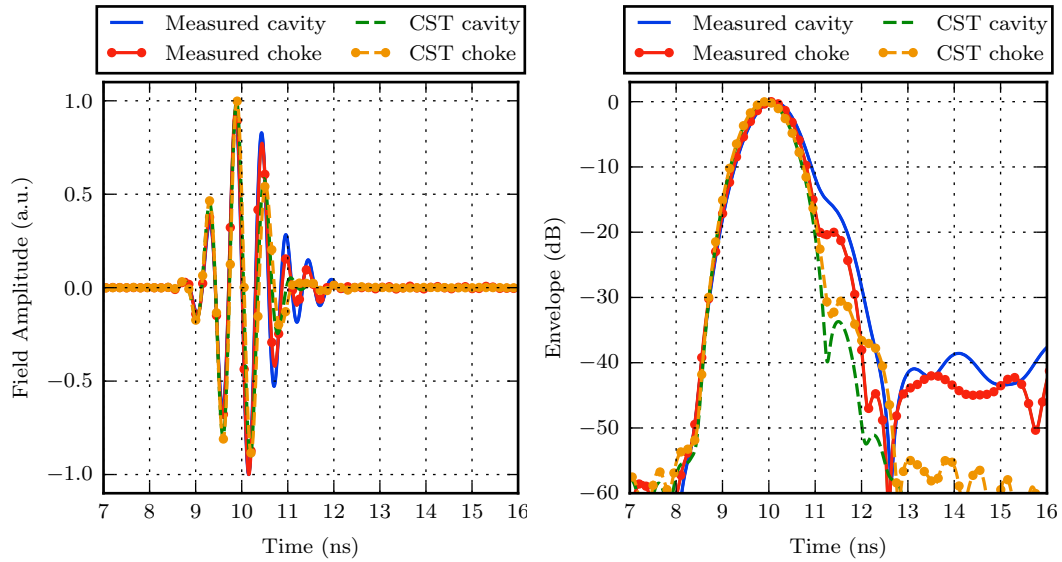
6.3 Fabrication

The four different cavity and choke-ring structures, with or without the absorber, were fabricated for testing. The walls of the structures were made of copper tape, with a solid aluminum disc as the back-plane for mechanical support. For the central cavity absorber, the commercially available Eccosorb AN-77 absorber was used. The Eccosorb is a simple three-layer absorber designed for free-space absorption, with good low-frequency performance, and a thickness less than the choke ring height d . To mechanically support the walls of the choke ring and cavity, as well as hold the antenna in place, the volumes of the choke-ring corrugation and the central cavity were cut from an extruded polystyrene foam possessing a vacuum response. The antenna was fed with a coaxial cable through the center of the aluminum plane and absorber. The cable was also affixed with a ferrite bead, placed behind the aluminum plane, to suppress unbalanced currents.

To reduce cost and simplify construction, the outer choke ring was constructed as a removable cylindrical structure that surrounds the central cavity,



(a) Linear scale, without absorber (b) Decibel scale (envelope), without absorber



(c) Linear scale, with absorber (d) Decibel scale (envelope), with absorber

Figure 6.4: Normalized measured and simulated pulse shapes (left) and their envelopes (right).

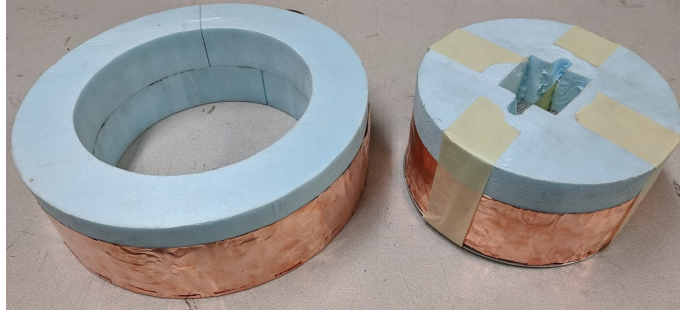


Figure 6.5: The fabricated cavity shield with the antenna inside, and the outer ring used to convert it into a choke-ring shield.

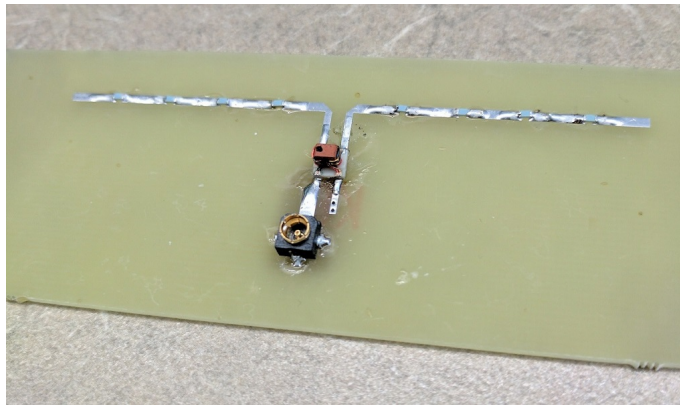


Figure 6.6: The fabricated antenna, consisting of a resistively loaded strip dipole, balun, feed network and MMCX connector.

such that the cavity shield could be converted to the choke-ring structure by swapping the back-plane with a larger sized disc, and placing the cylindrical structure around the central cavity. The cavity and choke ring were affixed to the backplane using masking tape. An image of the cavity and (separated) choke ring cylinder is shown in Fig. 6.5.

The antenna was printed on a 1.57-mm-thick FR-4 substrate and fed using a 50- Ω coaxial cable through the back-plane of the central cavity. The coaxial cable was connected to the substrate using an MMCX surface-mount connector, followed by a short 50- Ω microstrip section with a narrow, truncated ground-plane. To achieve a balanced signal and 200- Ω impedance at the antenna feed,

a Mini-Circuits 0.5 GHz–2.5 GHz TC4-25+ transformer was used. The ground plane was transitioned to the top layer using three via interconnects. An image of the fabricated antenna is shown in Fig. 6.6. A small length of MMCX to SMA cable was used to feed the antenna.

6.4 Measurement

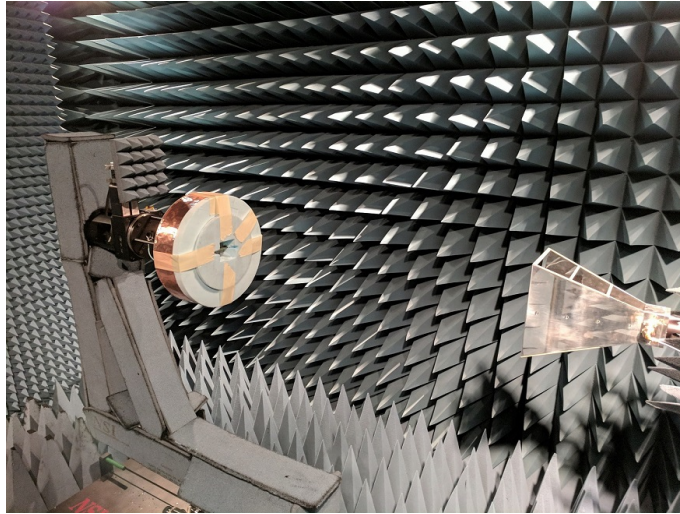


Figure 6.7: The choke-ring antenna mounted in the anechoic chamber.

To confirm the simulation results and design performance, antenna patterns of the fabricated prototypes were measured. Antenna pattern measurements were performed in an anechoic chamber equipped with an NSI near-field measurement system, using a double-ridged horn probe with a bandwidth of 0.75 GHz to 10 GHz as the receiving antenna. The cavity or choke-ring antennas were mounted on a spherical positioner, as shown in Fig. 6.7. Using the same setup, the S_{21} response between the horn and dipole antenna was measured in the 0.75 GHz to 2.5 GHz range in the boresight direction, using a vector network analyzer (VNA), for a reconstructed time-domain measurement. Similar measurements have been described previously in the literature, and are a popular way to measure an antenna’s response in the time domain

[178, 179, 180, 181, 182]. The receiving double-ridged horn is assumed to be sufficiently low-dispersion that any dispersion or ringing can generally be attributed to the small antenna and cavity or choke-ring shield. For completeness, and to see the effects of the choke and cavity structures on matching, S_{11} data was also measured.

The data were measured in steps of 2 MHz between 0.75 GHz and 2.5 GHz, for a total of 876 frequency points. This large number of data points was necessary to avoid aliasing effects in time. The data were further zero-padded to more easily distinguish the measured pulse shape and dispersion.

6.5 Results

The measured data are compared with simulation in Figs. 6.2, 6.3, and 6.4, and are generally in excellent agreement. The largest discrepancies are in the pulse response of the cavity and choke structures that include the absorber in the central cavity, seen in Figs. 6.4c and 6.4d. Agreement in the primary pulse is good up to 11 ns, after which there is a discrepancy in the predicted pulse power in the range of 10–15 dB, between 11 ns and 12 ns. This is the interval during which power would be expected to reflect from the cavity, and this additional measured power could be evidence the the AN-77 absorber does not behave as ideally as the simulation model. This can also be seen in the pulse dispersion, where the measured pulse shapes in Fig. 6.4c seem to mimic those without the absorber, as seen in Fig. 6.4a.

Beyond the 12 ns mark, the measured results also show clutter around -40 dB not accounted for in simulation. This clutter does not show the exponential decay expected of damped resonant phenomena. Rather, it is suspected to be due to multipath in the anechoic chamber, or difficult-to-model reflections in the antenna system, such as in the antenna feed network, balun, connectors or small cable lengths that could not be removed through calibration.

Note that GPR systems generally minimize the impact of cables by placing the active transmitter and receiver components directly at the feed point of the antenna, and such strategies are expected to reduce late-time clutter well below the -40 dB level observed in the measured data. Otherwise, the pulse shape is very similar between simulation and measurement. Note that without the absorber, the time-domain responses of the cavity and choke-ring shields are quite consistent between simulated and measured data, seen in Fig. 6.4a and 6.4b.

The agreement of the measured and simulated averaged radiation patterns is similarly good, with the worst agreement at the backlobe in the structures without the absorber, visible in Fig. 6.3a and 6.3b. This may, at least partly, be attributed to the blockage due to the metallic antenna mount, visible in Fig. 6.7. Dispersive characteristics of the feed network that alter the power spectra of the averaged patterns could be a contributing factor to the small differences at other angles.

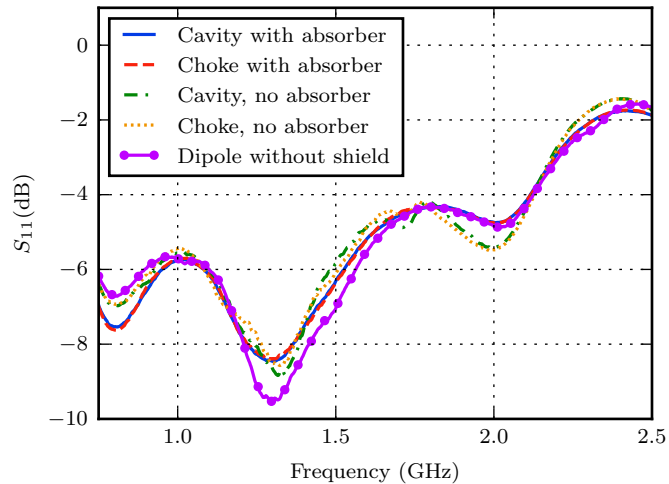


Figure 6.8: Measured S_{11} of the dipole backed by the different cavity/choke shields, compared to the unshielded dipole.

As for the RFP shown in Fig. 6.2, agreement between measurement and simulation tends to be worst around resonant features, likely due to minor

losses damping the response around resonance. Otherwise, there is some ripple and small variation with frequency present in the measured data compared to simulation. In general, small variations in the power distribution of the pattern can have relatively large effects on the RFP, as a result of the integration over all angles. This is especially the case when the power to the back of the structure is extremely low, such that small variations have a proportionally larger effect. The agreement is particularly good in the cases where absorbers are present in the cavity and choke ring.

Fig. 6.8 compares S_{11} of the cavity and shield structures to the dipole antenna without any shield; due to the difficulty in accurately modeling the balun structure, only measured data are presented. The antenna alone shows moderate matching performance over much of the 0.75 GHz to 2.5 GHz band, which is sufficient in a GPR context. The data are very consistent between the different structures, and suggest that the presence of the shield does not significantly affect the antenna's return-loss characteristics.

Chapter 7

Conclusion

7.1 Summary

This work has examined a variety of devices that can be used to shield antennas, and prevent their interaction with their surrounding environment, with particular focus on issues relevant to GPR. Due to the high degree of attenuation for signals propagating underground, GPR systems are sensitive to extraneous coupling or multipath signals between their Tx and Rx antennas, which may generally obscure weaker signals of underground origin. This can be due to above-ground reflectors, which can be a significant source of clutter, or due to coupling between Tx and Rx antennas such as along cables.

Cavity shield structures are a common method used to isolate GPR antennas. These cavities however, are not perfect; radiation diffracts around the cavity opening, which adds additional backlobes to the antenna pattern, and can be a source of clutter. Currents induced on the shield can also be a source of coupling between antennas. To address these issues, this work looked at two varieties of structure. The first was microwave absorbers, which are used to reduce reflection off of metallic structures, and can be used to dampen metallic shields. The second was finite, typically metallic ground plane structures, and related surfaces used to reduce diffraction at the ground plane's edges.

Despite the variety of absorber designs in the literature, most were found to be understandable through a common set of circuit methods. Resonant designs achieved good matching around a single frequency, or small number of frequencies, while designs using a tapered response to achieve smooth matching to free space generally had larger bandwidths, but at the cost of thickness. Regardless of the design method, these absorbers were found to be subject to the same bandwidth-thickness constraints. Available bandwidth was found to be proportional to the thickness of the absorber, and generally limited in its low-frequency performance. Maximum bandwidth for a given absorption level was generally achieved with designs that used a multi-resonant design to achieve moderate matching over a wider bandwidth, which can be realized using multi-layer designs such as the Jaumann absorber, or FSS-based designs. Such an absorber could achieve matching over a typical GPR bandwidth of 0.5 GHz to 2.5 GHz for a thickness of roughly 6 cm, and is a promising method to reduce the influence of surrounding metallic surfaces on the response of a GPR antenna. Magnetic materials were found to be an exception, capable of achieving wider bandwidths for a given absorber thickness, and are promising for lower-frequency absorbers for which large thicknesses would make otherwise prohibitive.

For the purpose of antenna shielding, a variety of finite ground plane structures were examined. Though the infinite ground plane is often studied as an ideal structure, the finite size of real ground planes can have important effects on the response of an antenna. This especially the case for ground planes with dimensions on the order of a wavelength. At the edge of a ground plane, impinging fields will generally re-radiate and diffract according to a Huygen's wavelet principle. This effect is enhanced when a ground plane is covered by a dielectric, which can support bound surface-wave modes. The reflected component of this diffracted signal for example, perturbs the input impedance of the exciting antenna, which will oscillate as a function of both ground plane

size and frequency. A portion of the diffracted signal will also reach the back of the ground plane, contributing to additional back and side lobes. For asymptotically large sizes, GTD or UTD were the most common techniques used to analyze diffraction effects. To reduce diffraction, designs which impede the propagation of currents to the edge of the ground plane, such as resistively tapered ground planes, or EBG surfaces that suppress currents, were considered effective.

Particular studies were done for a short resistively loaded dipole backed by either a metallic ground plane or cavity. For a ground plane, back-lobe radiation due to the finite size was found to exhibit something like a “transition frequency”, above which the ground plane had generally reduced back lobe. This transition frequency occurred for ground plane diameters of around $\lambda/2$. Edge diffraction on the ground plane was also found to be a source of late-time clutter in the radiated time-domain signal. The ground plane could also be designed such that this diffracted field either constructively or destructively interfered with the primary radiated signal.

For typical cavity shields, resonant effects were found to have strongly influence the shielding ability of the cavity. To summarize a shield’s ability to direct power forward, the RFP metric was developed. It was found that resonance of the TM_{11} circular waveguide mode within the cavity was detrimental to the RFP. For cavities of moderate depth, this occurred at frequencies near the TM_{11} cutoff frequency. The TM_{11} mode had a similarly detrimental effect on the pulsed time-domain response, with a large degree of ringing from energy stored in the cavity at the TM_{11} resonant frequency.

Due to the importance of surface waves when understanding diffraction around a shielding structure, we considered the excitation of surface wave modes above impedance surfaces. Inductive and PEC boundaries were found to support TM surface waves (plane waves in the limit), while capacitive and PMC or high-impedance surfaces supported TE surface waves. The TM and

TE surface wave solutions were found to correspond to two perpendicular polarizations. These ideas were shown to hold more formally by considering the Sommerfeld problem for a dipole above an impedance surface. This method also generalizes to lossy multilayer structures, and can be used to analyze absorbers in the vicinity of a dipole excitation. By choosing a surface impedance value that did not support the type of surface wave excited by the antenna, radiation near the surface would be suppressed. Vertical dipoles were found to excite TM surface waves at all polar angles, while horizontal dipoles excited TM surface waves in their E plane, and TE waves in the H plane.

Special attention was paid to corrugated surfaces, and related choke-ring shields. Due to the anisotropic impedance of the corrugated surface, waves see different surface impedances depending on the polarization and direction of propagation. As a result, above the $\lambda/4$ depth frequency up to a $\lambda/2$ depth, TM waves traveling perpendicularly to the corrugation see a capacitive surface, and are cut off. Similarly, TE waves in this same direction see a metallic surface, and are also cutoff. As a result, neither type of wave can propagate along the surface, and all radiation is suppressed. This is the soft surface property of corrugations and choke rings. Due to operation between the $\lambda/4$ and $\lambda/2$ depth frequencies, the choke ring shows an octave of bandwidth, making it one of the most wideband EBG surfaces, and an appealing choice for use as a GPR shield. To understand the effect of different design parameters on choke ring performance, a variety of parametric studies were performed. It was found that minimally thin metallic walls had the best shielding, and that overall size was the largest determinant of the RFP of a choke-ring shield. The number of rings was fairly inconsequential to choke ring performance in its capacitive impedance region. For moderately size designs, only a single corrugation (two metallic rings) was preferable for its simplicity.

Based on these guidelines, a choke ring design was fabricated and measured. To reduce ringing effects due to energy stored in the cavity, the choke-ring shield

was modified to include a dielectric absorber within its cavity. Comparable cavity shields with and without the absorber were also measured, for a total of four different designs. These shields were used to back a short lossy printed dipole antenna. To assess the time-domain performance of the shields, a time-domain pulsed response at boresight was reconstructed from frequency-domain transmission data. For this measurement, the antenna was effectively excited by a pulse with frequency components between 0.75 GHz and 2.5 GHz. These measurements showed the successful suppression of ringing effects due to the cavity, and a reduction in reflected power from the cavity. Antenna patterns of the different shield structures were also measured. Since single-frequency antenna patterns are not very representative of radiation from a wideband pulse, time-averaged patterns and their frequency-domain equivalent were considered instead. The choke ring was shown to provide a 3–5-dB redirection of radiated power from the back to the front of the shield, while the inclusion of the absorber ensured less than -40 dB of late-time clutter.

7.2 Future Work

While this work has considered the far-field performance of the choke-ring antenna shield in an air dielectric, GPR antennas function close to the ground and operate in the antenna’s near-field, both of which add further complexity. Subsequent work would establish the value of choke-ring shielding under these conditions. It is also necessary to explore shielding structures which incorporate both Tx and Rx antennas, as well as ways to reduce coupling between them. Finally, the choke-ring shield suffers from its relatively large size; it will be necessary to consider strategies for reducing choke-ring sizes. In this section, we shall briefly consider some further possible designs that use principles developed in this work, and address some of these issues.

7.2.1 Multiple Disc Reflectors

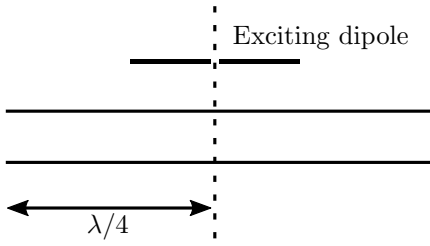


Figure 7.1: Horizontal choke structure. The symmetry plane is marked as the dashed line.

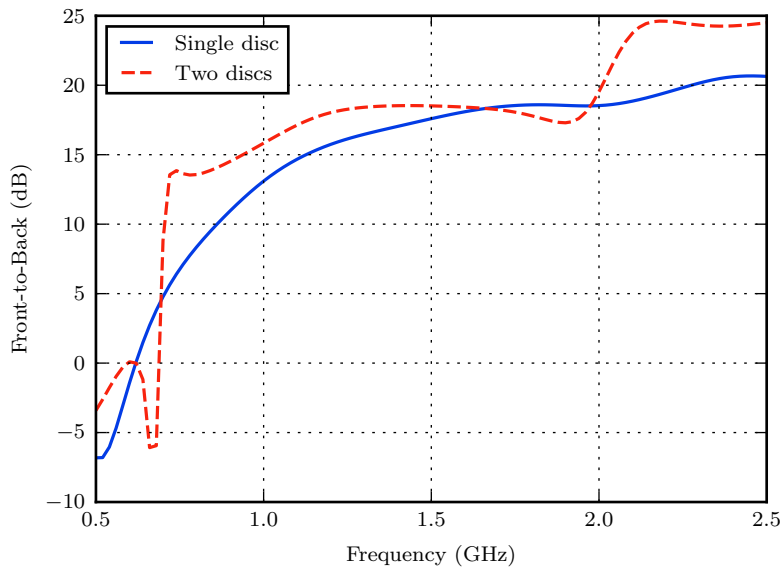


Figure 7.2: Front-to-back ratio of a single disc versus the two-disc choke design.

One of the difficulties of the choke-ring shield was its large size. In addition to the minimum $\lambda/4$ depth, the choke ring corrugations surround a central cavity, which has a minimum size due to the cutoff frequency of its fundamental TE_{11} mode. One way to reduce this size is to take advantage of horizontal rather than vertical length to achieve the $\lambda/4$ condition. This is shown in Fig. 7.1. Due to the symmetry condition, the symmetry plane acts like a PEC termination to the horizontal corrugation, and the total length of the structure is $\lambda/2$. This

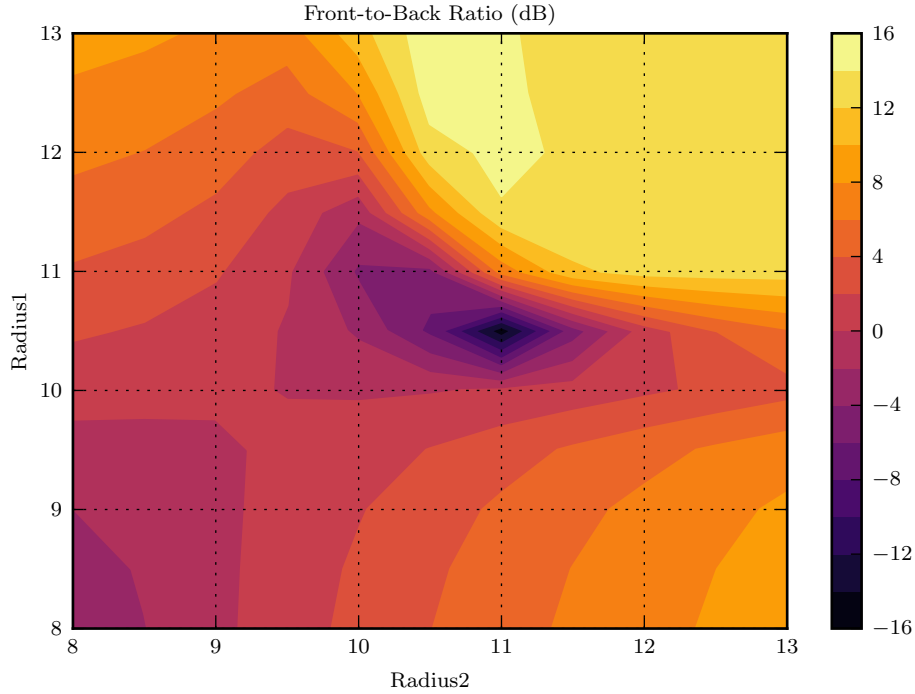


Figure 7.3: Front-to-back ratio at 0.75 GHz as the radii of the two discs backing a dipole are varied. Radius1 is for the disc closer to the dipole.

could be fabricated for example, by using two closely spaced ground planes, with either rectangular or circular geometry. Preliminary studies using two discs suggest that most of the properties associated with the choke ring plane also hold for this two-disc reflector geometry. For this structure, the energy between the discs can be modeled as a parallel plate mode, which predicts the choke resonant frequency. The front-to-back ratio of a single versus two-disc shield designed for 0.75 GHz is shown in Fig. 7.2, based off of the ground-plane-backed dipole model discussed in Chap. 3, with the additional disc spaced 3 cm from the first. This design is limited at the upper frequency by a higher-order parallel plate mode, for roughly an octave of bandwidth. Fig. 7.3 shows how the front-to-back ratio depends on the radii of the two discs. The front-to-back ratio evidently depends on the dimension of the second disc in addition to the disc closer to the dipole, and also potentially shows backfire characteristics,

depending on the values chosen.

7.2.2 Anisotropic Resistive Ground Planes

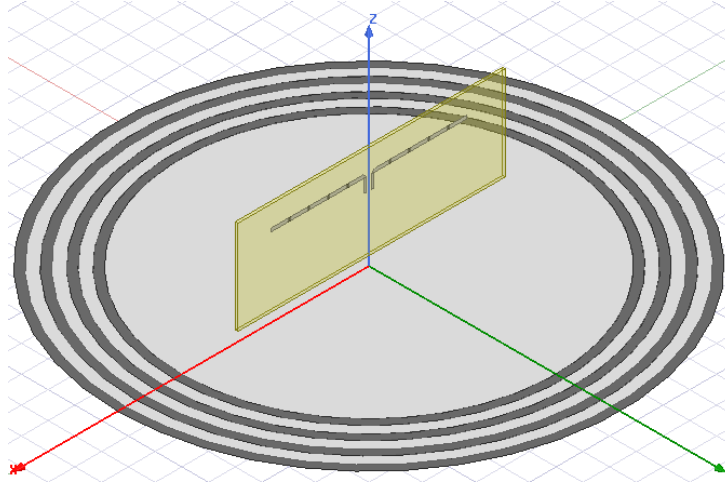


Figure 7.4: Depiction of an anisotropic resistive surface inspired by the soft-surface principle used in choke ring designs.

One of the methods discussed in Chap. 3 to reduce ground plane diffraction on a ground plane is using a resistive surface at its edge. These are expected to reduce diffraction from TM-polarized waves, which are the major source of diffraction for most ground plane structures. Resistive surfaces however, are not as ideal as PEC surfaces for the reduction of diffraction for TE-polarized waves. The same design method used to realize a soft surface using an anisotropic surface can be used to create ground planes which act similarly to a metallic surface for TE-polarized radiation, while being otherwise resistive for TM-polarized radiation. Such a surface could be realized by a set of planar, concentric rings, electrically connected by a set of annular resistive strips, or lumped-element resistors. The effective surface impedance seen for TM-polarized radiation could be controlled both by the choice of resistive material, as well as the radial length of resistive and metallic elements, which could be used to realize a tapered surface impedance, for example. Such a

ground plane structure is pictured in Fig. 7.4.

7.2.3 Absorber-Loaded Choke Rings

In Chap. 4, the Sommerfeld half-space problem for a dipole over a resistive surface showed that a resistive surface has a similar effect to a capacitive surface in its ability to suppress radiation along its surface. This model, however, used a constant surface impedance. For most of the absorbers discussed in Chap. 2, the effective surface impedance changes as a function of angle of the incoming radiation. By forcing energy into a parallel plate mode, a corrugated surface achieves a constant surface impedance for all impinging angles. Choke rings loaded with an absorber would similarly have a constant surface impedance for all angles. By loading a choke ring with a broadband absorber, this would create a broadband resistive surface for all angles of impinging radiation. This surface impedance would also be anisotropic, and would act to the ideal PEC surface for TE-polarized radiation. Due to the loss within the choke ring, this design would be expected to have minimal influence on the time-domain performance of an antenna.

Appendix A

Signal Processing & Time-Domain Properties

The vast majority of signal characteristics for antennas and microwave systems are based on Fourier transform properties. Here, we use a definition for the Fourier transform and its inverse common in engineering applications:

$$X(\omega) = \mathcal{F}\{x(t)\} = \int_{-\infty}^{\infty} x(t)e^{-j\omega t} dt \quad (\text{A.1})$$

$$x(t) = \mathcal{F}^{-1}\{X(\omega)\} = \frac{1}{2\pi} \int_{-\infty}^{\infty} X(\omega)e^{j\omega t} d\omega \quad (\text{A.2})$$

Signals in the time domain are taken to be purely real valued.

A.1 Antenna Transfer Function Approach

Antenna systems are typically linear time-invariant systems, and can be characterized by a composition of transfer functions in the frequency domain (equivalently, impulse responses in the time domain). For a Tx and Rx antenna communicating over a channel, such a system is shown in Fig. A.1. An antenna's transfer function $H_{Tx}(f)$ or $H_{Rx}(f)$ will depend on the port impedance

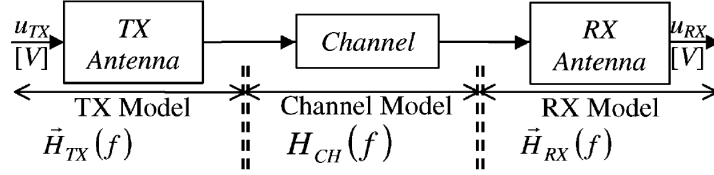


Figure A.1: Block model for different components in an antenna system, with transfer functions labeled [6].

the antenna is terminated in, and reflections due to mismatches in impedance are already accounted for in these transfer functions. The channel's transfer function H_{Ch} for free space will usually take the form of a spherical wave, with [6, 183]:

$$H_{ch} = \frac{e^{-jkr}}{r} \quad (\text{A.3})$$

An important point is that $H_{Tx}(\omega)$ is defined for an antenna radiating a spherical wave, while $H_{Rx}(\omega)$ is defined for an antenna receiving power from a plane-wave-like wave front. As such, $H_{Tx}(\omega) \neq H_{Rx}(\omega)$. The two transfer functions however, are related by reciprocity. For a Tx antenna, H_{Tx} is closely related to the realized gain:

$$G_r = |H_{Tx}|^2 \quad (\text{A.4})$$

or similarly the gain with an additional term for port mismatches:

$$G = \frac{|H_{Tx}|^2}{1 - |\Gamma|^2} \quad (\text{A.5})$$

while $H_{Rx}(\omega)$ corresponds to the effective aperture A_e modified appropriately to account for port mismatch:

$$A_e = \frac{|H_{Rx}|^2}{1 - |\Gamma|^2} \quad (\text{A.6})$$

One of the consequences of Eq. A.5 and A.6 is that antennas that radiate their exciting pulse with no dispersion have a constant realized gain, while the

corresponding dispersion-free receiving antenna has constant effective aperture. Thus when measuring the transfer function of a transmitting antenna, it is desirable to use an antenna with constant effective aperture.

A.2 Short Dipole

A well-known result for a point electric dipole is that it radiates a second derivative in the time domain [175]. Since derivatives in the time domain result in multiplication by ω in the frequency domain, point dipoles act like ω^2 high-pass filters on any exciting pulse. Since all dipoles act like point dipoles at asymptotically low frequencies, they will all have this same characteristic high-pass response at low-frequencies. Through a multi-pole expansion, most large dipoles will also show a second-derivative-like response, especially when excited by a broadband pulse with significant low-frequency components. Early in time, currents will be localized to a smaller volume, and the point dipole response is more accurate, while currents that propagate further outward on a dipole will radiate later in time. As a result, the early-time response of dipoles will resemble the ideal small dipole second derivative response, seemingly perturbed by additional signal components at later times. In response to a broadband pulse, large dipoles will thus typically radiate a broader pulse in comparison to a short dipole. The simplicity, low dispersion, and short pulse width of this second derivative response, together with the small size of the short dipole make it very convenient as a GPR antenna.

A.2.1 Ground-Plane-Backed Dipole

For a dipole closely backed by a ground plane, both the dipole and its image contribute to the radiated signal. The image dipole however, has its currents out of phase with the original dipole. The image will thus interfere with the exciting dipole, but with a phase delay related to the distance d of the dipole

above the plane. For a dipole originally radiating a signal $u(t)$, the modified signal due to the ground plane is given by the equation:

$$u_{\text{total}}(t) = u(t) - u(t - 2d/c) \quad (\text{A.7})$$

When the dipole is closely spaced to the ground plane, or at asymptotically low frequencies, this is closely approximated by a derivative.

$$u_{\text{total}}(t) \approx \frac{d}{c} \frac{\partial u(t)}{\partial t} \quad (\text{A.8})$$

Given the short dipole already radiates a second derivative response, short dipoles closely spaced to a ground plane will resemble a third derivative of the exciting pulse, with the reflecting ground plane acting as an additional high-pass filter on the response.

A.3 Pulse Characteristics

A.3.1 Gaussian Pulse

Gaussian pulses are a common exciting pulse in GPR systems, and are also a good illustration of bandwidth-pulse-width characteristics. In the time domain, a Gaussian pulse has the form:

$$u(t) = A \exp\left(-\frac{t^2}{2\sigma_t^2}\right) \quad (\text{A.9})$$

The parameter σ_t characterizes the pulse width, with larger σ_t corresponding to wider pulse widths. The frequency domain representation of a Gaussian pulse is also a Gaussian:

$$U(\omega) = A \frac{\sqrt{2\pi}}{\sigma_\omega} \exp\left(-\frac{\omega^2}{2\sigma_\omega^2}\right) \quad (\text{A.10})$$

where $\sigma_\omega = 1/\sigma_t$, and similarly characterizes the bandwidth of the pulse. This inverse relationship between pulse width and bandwidth is representative of short pulses in general. Though Gaussian pulses are common in GPR, they have the disadvantage of having frequency components down DC, which are non-radiating. Derivatives of the Gaussian pulse are also commonly used, and have the advantage of having no DC component. The first-order Gaussian derivative is referred to as a monocycle pulse, while the second-order Gaussian derivative is called a Ricker wavelet, both of which are common exciting pulses. Another alternative is a frequency-modulated Gaussian. If the modulation frequency is sufficiently high compared to the bandwidth, then the DC component of the pulse can be approximated as zero.

A.3.2 Hilbert Transform

For a pulse in the time domain with some underlying carrier frequency, the Hilbert transform can be used to calculate the envelope of the pulse. The pulse envelope is useful when comparing pulse widths, or for plotting pulses on a decibel scale. The Hilbert transform is given by the equation [184]:

$$H\{u\}(t) = \frac{1}{\pi} \int_{-\infty}^{\infty} \frac{u(\tau)}{t - \tau} d\tau \quad (\text{A.11})$$

Given an analytic function, the Hilbert transform can be thought of as taking the real part and returning the imaginary part. Hence, for a real-valued time-domain signal $u(t)$, the envelope of the signal can be calculated as $|u + jH\{u}|(t)$. The complex signal $u(t) + jH\{u\}(t)$ can also be calculated by setting all negative-frequency components to zero, and taking the inverse transform.

A.3.3 Windowed Pulses

In the context of antennas, it is often convenient to refer to bandwidths as having specific start and end frequencies. It is not possible however, to excite

pulses in the time domain that have discrete start and end frequencies. Perfectly abrupt transitions in the frequency domain will cause ripple in the time domain, with the ripple level determined by the abruptness of the transition. A transfer function measured over a definite bandwidth can be modeled as taking the total transfer function over all frequencies, and multiplying it by a rectangular window

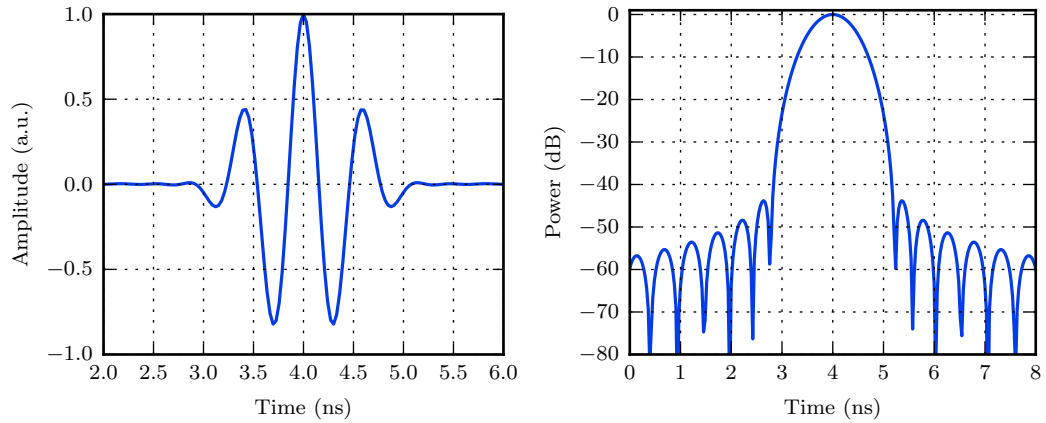
$$H_{\text{measured}}(\omega) = H(\omega)\Pi_{a,b}(|\omega|) \quad (\text{A.12})$$

where $\Pi_{a,b}(|\omega|)$ is the box-car function, which evaluates to 1 inside the interval $|\omega| \in (a, b)$, but is otherwise 0. The absolute value of frequency is used to ensure the resulting time-domain signal is real. In the time domain, the result is that the impulse response is convolved with a sinc function. For a measurement bandwidth of $\Delta\omega = b - a$ and center frequency of $\omega_0 = (a + b)/2$, the measured impulse response is given by:

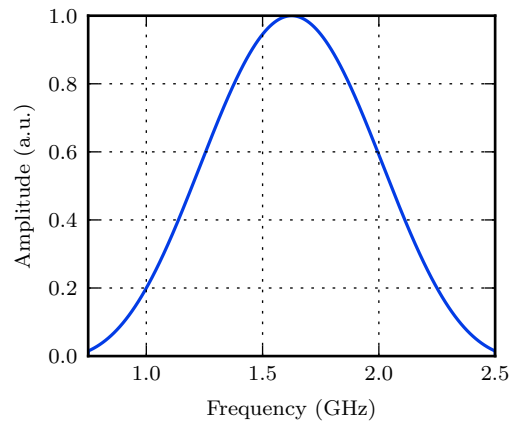
$$h_{\text{measured}}(t) = h(t) * \frac{\Delta\omega \operatorname{sinc}\left(\frac{\Delta\omega}{2}t\right)}{2\pi} \cos(\omega_0 t) \quad (\text{A.13})$$

This measured response is essentially the time domain response if the system were excited with a sinc pulse. This is problematic in that the sinc function is acausal, with a very large degree of ripple extending to infinity in both directions. This is not realizable in a physical system, and the ripple also has the effect of obscuring other relevant time-domain features.

To remedy this issue, we can consider window functions used in the context of digital signal processing, and are well-optimized to have minimal ripple for their main pulse width [185]. Common windows include the Blackman or Hamming window. The particular choice of window will determine the level of ripple relative to main pulse width, with a trade off between the two. One useful window used in this work is the Kaiser window [150, 151], which approximately minimizes ripple energy. The Kaiser window has a parameter β , which modifies the pulse width relative to ripple level. The Kaiser pulse for



(a) Kaiser pulse on an amplitude scale. (b) Kaiser pulse on a decibel scale.



(c) Kaiser window in the frequency domain.

Figure A.2: Different representations of the normalized Kaiser pulse, based on the a Kaiser window in the frequency domain between 0.75 GHz and 2.5 GHz.

$\beta = 6$ and its frequency spectrum are shown in Fig. A.2. When these windows are applied to the frequency-domain measurement of an impulse response, the system can be thought of as being excited by a pulse with a spectrum as given by the corresponding window function.

Bibliography

- [1] David J. Sawyer, Ashwin K. Iyer, A. Peter Annan, and Nectaria Diamanti. Investigation of choke-ring structures for ground-penetrating radar. In *IEEE 2017 Antennas and Propagation Society and URSI USNC International Symposium Digest*, pages 1883–1884, July 2017.
- [2] www.sensoft.ca.
- [3] D. Sievenpiper, L. Zang, R. F. J. Broas, N. G. Alexopolous, and E. Yablonovitch. High-impedance electromagnetic surfaces with a forbidden frequency band. *IEEE Transactions on Microwave Theory and Techniques*, 47(11):2059–2074, November 1999.
- [4] D. B. Hodge. Scattering by circular metallic disks. *IEEE Transactions on Antennas and Propagation*, 28(5):707–712, September 1980.
- [5] Gregory D. Durgin. The practical behavior of various edge-diffraction formulas. *IEEE Antennas and Propagation Magazine*, 51(3):24–35, June 2009.
- [6] Y. Duroc, A. Ghiotto, T. P. Vuong, and S. Tedjini. UWB antennas: systems with transfer function and impulse response. *IEEE Transactions on Antennas and Aropagation*, 5(5):1449–1451, May 2007.
- [7] J. L. Davis and A. P. Annan. Ground-penetrating radar for high-resolution mapping of soil and rock stratigraphy. *Geophysical Prospecting*, 37(5):531–551, July 1989.

- [8] D. J. Daniels, editor. *Ground Penetrating Radar*, page 21. IET Radar, Sonar, Navigation and Avionics Series 15. The Institution of Engineering and Technology, Stevenage, UK, 2004.
- [9] A. P. Annan. Ground-penetrating radar. In D. K. Butler, editor, *Near-Surface Geophysics*, pages 357–438. Society of Exploration Geophysicists, Tulsa, OK, 2005.
- [10] N. Diamanti and A. P. Annan. Characterizing the energy distribution around GPR antennas. *Journal of Applied Geophysics*, 99:83–90, December 2013.
- [11] Disala Uduwawala, Martin Norgren, Peter Fuks, and Aruna W. Gunawardena. A deep parametric study of resistor-loaded bow-tie antennas for ground-penetrating radar using FDTD. *IEEE Transactions on Geoscience and Remote Sensing*, 42(4):732–742, April 2004.
- [12] Uğur Oğuz and Levent Gürel. Modeling of ground-penetrating-radar antennas with shields and simulated absorbers. *IEEE Transactions on Antennas and Propagation*, 49(11):1560–1567, November 2001.
- [13] F. Sciré-Scappuzzo and S. N. Makarov. A low-multipath wideband GPS antenna with cutoff or non-cutoff corrugated ground plane. *IEEE Transactions on Antennas and Propagation*, 57(1):33–46, March 2009.
- [14] P. Bhartia, Inder Bahl, R. Garg, and A. Ittipiboon. *Microstrip Antenna Design Handbook*. Artech House, 1999.
- [15] Claire M. Watts, Xianliang Liu, and Willie J. Padilla. Metamaterial electromagnetic wave absorbers. *Advanced Materials*, 24(23):OP98–OP120, May 2012.
- [16] Winfield W. Salisbury. Absorbent body for electromagnetic waves. U.S. Patent 2 599 944, June 1952.

- [17] P. G. Lederer. Modelling of practical Salisbury screen absorbers. In *IEEE Colloquium on Low Profile Absorbers and Scatterers*, pages 1/1–1/4, May 1992.
- [18] J. A. Menéndez, A. Arenillas, B. Fidalgo, Y. Fernández, L. Zubizarreta, E.G. Calvo, and J.M. Bermúdez. Microwave heating processes involving carbon materials. *Fuel Processing Technology*, 91(1):1–8, January 2010.
- [19] Jin-Bong Kim and Joon-Hyung Byun. Salisbury screen absorbers of dielectric lossy sheets of carbon nanocomposite laminates. *IEEE Transactions on Electromagnetic Compatibility*, 54(1):37–42, February 2012.
- [20] Jeong Min Woo, Min-Sik Kim, Hyun Woong Kin, and Jae-Hyung Jang. Graphene based Salisbury screen for terahertz absorber. *Applied Physics Letters*, 104(8):081106, February 2014.
- [21] Ronald L. Fante and Michael T. McCormack. Reflection properties of the Salisbury screen. *IEEE Transactions on Antennas and Propagation*, 36(10):1443–1454, October 1998.
- [22] B. Chambers. Optimum design of a Salisbury screen radar absorber. *Electronic Letters*, 30(16):1353–1354, August 1994.
- [23] E. F. Knott and C. D. Lunden. The two-sheet capacitive Jaumann absorber. *IEEE Transactions on Antennas and Propagation*, 43(11):1339–1343, November 1995.
- [24] G. C. Temes and J. W. LaPatra. *Circuit Synthesis and Design*. McGraw Hill, Tokyo, 1977.
- [25] Leendert Johannes du Toit. *Analysis and Synthesis Algorithms for the Electric Screen Jauman Electromagnetic Wave Absorber*. PhD thesis, Univ. of Stellenbosch, Stellenbosch, November 1993. URL <http://hdl.handle.net/10019.1/20463>.

- [26] William H. Emerson. electromagnetic wave absorbers and anechoic chambers through the years. *IEEE Transactions on Antennas and Propagation*, 21(4):484–490, July 1973.
- [27] Ahmad Cheldavi and Mahmoud Kamarei. Optimum design of N sheet capacitive Jaumann absorber using genetic algorithm. *IEICE Transactions on Fundamentals of Electronics, Communications and Computer Sciences*, E82-A(4):2296–2299, April 1999.
- [28] Daniel S. Weile and Eric Michelssen. Genetic algorithm optimization applied to electromagnetics: a review. *IEEE Transactions on Antennas and Propagation*, 45(3):343–353, March 1997.
- [29] B. Chambers, A. P. Anderson, and R. J. Mitchell. application of genetic algorithms to the optimisation of adaptive antenna arrays and radar absorbers. In *1st International Conference on Genetic Algorithms in Engineering Systems: Innovations and Applications (GALESIA)*, pages 94–99, September 1995.
- [30] Eric Michelssen, Jean Michel Sajer, S. Ranjithan, and Raj Mittra. Design of lightweight, broad-band microwave absorbers using genetic algorithms. *IEEE Transactions on Microwave Theory and Techniques*, 41(6/7):1024–1031, June 1993.
- [31] B. Chambers and A. Tennant. Optimised design of Jaumann radar absorbing materials using a genetic algorithm. *IEE Proceedings - Radar, Sonar, and Navigation*, 143(1):23–30, February 1996.
- [32] Benedikt A. Munk and Jonothan Pryor Peter Munk. On designing Jaumann and circuit analog absorbers for oblique angle of incidence. *IEEE Transactions on Antennas and Propagation*, 55(1):186–193, January 2007.

- [33] B. Chambers and A. Tennant. Design of wideband Jaumann radar absorbers with optimum oblique incidence performance. *Electronic Letters*, 30(18):1530–1532, September 1996.
- [34] N. Engheta. Thin absorbing screens using metamaterial surfaces. In *IEEE Antennas and Propagation Society International Symposium*, volume 2, pages 392–395, June 2002.
- [35] D. J. Kern and D. H. Werner. A genetic algorithm approach to the design of ultra-thin electromagnetic bandgap absorbers. *Microwave and Optical Technology Letters*, 38(1):61–64, July 2003.
- [36] Filippo Costa, Agostino Monorchio, and Giuliano Manara. Analysis and design of ultra thin electromagnetic absorbers comprising resistively loaded high impedance surfaces. *IEEE Transactions on Antennas and Propagation*, 58(5):1551–1558, May 2010.
- [37] A Munir and V. Fusco. Effect of surface resistor loading on high-impedance surface radar absorber return loss and bandwidth. *Microwave and Optical Technology Letters*, 51(7):1773–1775, July 2009.
- [38] Daniel Sievenpiper. *High-Impedance Electromagnetic Surfaces*. PhD thesis, Univ. of California, Los Angeles, 2000.
- [39] S. A. Tretyakov and S. I. Maslovski. Thin absorbing structure for all incidence angles based on the use of a high-impedance surface. *Microwave and Optical Technology Letters*, 38(3):175–178, August 2003.
- [40] Olli Luukkonen, Filippo Costa, Constantin R. Simovski, Agostino Monorchio, and Sergei A. Tretyakov. A thin electromagnetic absorber for wide incidence angles and both polarizations. *IEEE Transactions on Antennas and Propagation*, 57(10):3119–3125, October 2009.

- [41] H. Mosallaei and K. Sarabandi. A one-layer ultra-thin meta-surface absorber. In *IEEE Antennas and Propagation Society International Symposium*, volume 1B, pages 615–618, July 2005.
- [42] Liu Hai-Tao, Cheng Hai-Feng, Chu Zheng-Yong, and Zhang De-Yong. absorbing properties of frequency selective surface absorbers with cross-shaped resistive patches. *Materials and Design*, 28:2166–2171, March 2007.
- [43] A. Tennant and B. Chambers. A single-layer tuneable microwave absorber using an active FSS. *IEEE Microwave and Wireless Components Letters*, 14:46–47, January 2004.
- [44] Frédéric Terracher, Gérard Berginc, and Rue Guynemer. Thin electromagnetic absorber using frequency selective surfaces. In *IEEE Antennas and Propagation Society International Symposium. Transmitting Waves of Progress to the Next Millennium. 2000 Digest*, volume 2, pages 846–849, July 2000.
- [45] Yanan Sha, K. A. Jose, C. P. Neo, and Vijay K. Varadan. Experimental investigations of microwave absorber with FSS embedded in carbon fiber composite. *Microwave and Optical Technology Letters*, 32(4):245–249, February 2002.
- [46] Raj Mittra, Chi H. Chan, and Tom Cwik. Techniques for analyzing frequency selective surfaces—a review. In *Proceedings of the IEEE*, volume 76, pages 1593–1615, December 1988.
- [47] Te-Kai Wu and Shung-Wu Lee. Tri-band frequency selective surface with circular ring elements. *IEEE Transactions on Antennas and Propagation*, 42(2):166–175, February 1994.
- [48] Alireza Kazem and Anders Karlsson. Capacitive circuit method for fast

and efficient design of wideband radar absorbers. *IEEE Transactions on Antennas and Propagation*, 57(8):2307–2314, August 2009.

- [49] L. K. Sun, H. F. Cheng, Y. J. Zhou, and J. Wang. Broadband metamaterial absorber based on coupling resistive frequency selective surface. *Optics Express*, 20(4):4676–4680, February 2012.
- [50] G. T. Ruck, D. E. Barrick, and W. D. Stuart. *Radar Cross Section Handbook*, volume 2. Plenum, New York, 1970.
- [51] Paul Saville, Trisha Huber, , and Darren Makeiff. Fabrication of organic radar absorbing materials. DRDC Atlantic TR 124, Defense research and development Canada, 2005.
- [52] V. M. Petrov and V. V. Gagulin. Microwave absorbing materials. *Inorganic Materials*, 37(2):93–98, February 2001.
- [53] J. W. Tiley. Radio wave absorption device. U.S. Patent 2 464 006, March 1949.
- [54] Maosheng Cao, Jing Zhu, Jie Yuan, Tiefu Zhang, Zhihui Peng, Zhengjuan Gao, Gang Xiao, and Shiming Qin. Computation design and performance prediction towards a multi-layer microwave absorber. *Materials and Design*, 23(6):557–564, September 2002.
- [55] D.S. Weile, E. Michielssen, and D. E. Goldberg. Genetic algorithm design of Pareto optimal broadband microwave absorbers. *IEEE Transactions on Electromagnetic Compatibility*, 38(3):518–525, August 1996.
- [56] M. J. Asi. Design of multilayer microwave broadband absorbers using central force optimization. *Progress in Electromagnetics research B*, 26: 101–113, 2010.

- [57] Jin Bong Kim, Sang-Kwan Lee, and Chun-Gon Kim. Comparison study on the effect of carbon nanomaterials for single-layer microwave absorbers in X. *Composites Science and Technology*, 68(14):2909–2916, 2008.
- [58] Sang Eui Lee, Oyoung Choi, and H. Thomas Hahn. Microwave properties of graphite nanoplatelet/epoxy composites. *Journal of Applied Physics*, 104(3):033705, August 2008.
- [59] D. Micheli, C. Apollo, R. Pastore, and M. Marchetti. X-band microwave characterization of carbon-based nanocomposite material, absorption capability comparison and RAS design simulation. *Composites and Science Technology*, 70(2):400–409, February 2010.
- [60] John L. Wallace. Broadband magnetic microwave absorbers: Fundamental limitations. *IEEE Transactions on Magnetics*, 29(6):4209–4214, November 1993.
- [61] P. Saville. Optimisation of Dallenbach layers using real materials. DRDC Atlantic TR 12, Defense Research and Development Canada, 2007.
- [62] A. Cheldavi and M. Kamarei. Practical optimum design for a single-layer electromagnetic wave absorber at C and X-band using genetic algorithm. In *IEEE Antennas and Propagation Society International Symposium 1997 Digest*, volume 3, pages 1708–1711, July 1997.
- [63] Igor Maria De Rosa, Adrian Dinescu, Fabrizio Sarasini, Maria Sabrina Sarto, and Alessio Tamburrano. Effect of short carbon fibers and MWCNTs on microwave absorbing properties of polyester composites containing nickel-coated carbon fibers. *Composites Science and Technology*, 70(1):102–109, January 2010.
- [64] S. Sugimoto, S. Kondo, K. Okayama, H. Nakamura, D. Book, T. Kagotani, M. Homma, H. Ota, M. Kimura, and R. Sato. M-type fer-

- rite composite as microwave absorber with wide bandwidth in the GHz range. *IEEE Transactions on Magnetics*, 35(5):3154–3156, September 1999.
- [65] M. R. Meshram, Nawal K. Agrawal, Bharoti Sinha, and P. S. Misra. Characterization of M-type barium hexagonal ferrite-based wide band microwave absorber. *Journal of Magnetism and Magnetic Materials*, 271(2-3):207–214, May 2004.
- [66] Vijutha Sunny, Philip Kurian, P. Mohanan, P. A. Joy, and M. R. Anatharaman. A flexible microwave absorber based on nickenl ferrite nanocomposite. *Journal of Alloys and Compounds*, 489(1):297–303, January 2010.
- [67] Guozhu Shen, Ming Xu, and Zheng Xu. Double-layer microwave absorber based on ferrite and short carbon fiber composites. *Materials Chemistry and Physics*, 150(2-3):268–272, October 2007.
- [68] Yuchang Qing, Wancheng Zhou, Fa Luo, and Dongmei Zhu. Epoxy-silicone filled with multi-walled carbon nanotubes and carbonyl iron particles as a microwave absorber. *Carbon*, 48(14):4074–4080, November 2010.
- [69] Viktor G. Veselago. The electrodynamics of substances with simultaneously negative values of ϵ and μ . *Soviet Physics Uspekhi*, 10(4):509–514, 1968.
- [70] R. A. Shelby, D. R. Smith, and S. Shultz. Experimental verification of a negative index of refraction. *Science*, 292(5514):77–79, April 2001.
- [71] N. I. Landy, J. J. Mock, D. R. Smith, and W. J. Padilla. Perfect metamaterial absorber. *Physical Review Letters*, 100:207402, May 2008.

- [72] J. B. Pendry, A. J. Holden, D. J. Robbins, and W. J. Stewart. Low frequency plasmons in thin-wire structures. *Journal of Physics: Condensed Matter*, 10(22):4785–4809, 1998.
- [73] J. B. Pendry, A. J. Holden, D. J. Robbins, and W. J. Stewart. Magnetism from conductors and enhanced nonlinear phenomena. *IEEE Transactions on Microwave Theory and Techniques*, 47(11):2075–2084, November 1999.
- [74] D. R. Smith, Willie J. Padilla, D. C. Vier, S. C. Nemat-Nasser, and S. Schultz. Composite medium with simultaneously negative permeability and permittivity. *Physical Review Letters*, 84(18):4184–4187, May 2000.
- [75] Hongsheng Chen, Lixin Ran, Jiangtao Huangfu, Xianmin Zhang, and Kangsheng Chen. Left-handed materials composed of only S-shaped resonators. *Physical Review E*, 70(5):057605, November 2004.
- [76] Li Huang, Dibakar Roy Chowdhury, Suchitra Ramani, Matthew T. Reiten, Sheng-Nian Luo, Abul K. Azad, Antoinette J. Taylor, and Hou-Tong Chen. Impact of resonator geometry and its coupling with ground plane on ultrathin metamaterial perfect absorbers. *Applied Physics Letters*, 101(10):102, September 2012.
- [77] Fei Ding, Yanxia Cui, Xiaochen Ge, Yi Jin, and Sailing He. Ultra-broadband microwave metamaterial absorber. *Applied Physics Letters*, 100(10):103506, March 2012.
- [78] Saptarshi Ghosh, Somak Bhattacharyya, Yadunath Kaiprath, and Kumar Vaibhav Srivastava. Bandwidth-enhanced polarization-insensitive microwave metamaterial absorber and its equivalent circuit model. *Journal of Applied Physics*, 115:104503, March 2014.
- [79] Borui Bian, Shaobin Liu, Shenyun Wang, Xiangkun Kong, Haifeng

- Zhang, Ben Ma, and Huan Yang. Novel triple-band polarization-insensitive wide-angle ultra-thin microwave metamaterial absorber. *Journal of Applied Physics*, 114(19):194511, November 2013.
- [80] Wang Guo-Dong, Liu Ming-Hai, Hu Xi-Wei, Kong Ling-Hua, Cheng Li-Li, and Chen Zhao-Quan. Multi-band microwave metamaterial absorber based on coplanar jerusalem crosses. *Chinese Physics B*, 23(1):017802, December 2014.
- [81] Hou-Tong Chen. Interference theory of metamaterial perfect absorbers. *Optics Express*, 20(7):7165–7172, March 2012.
- [82] Konstantin N. Rozanov. Ultimate thickness to bandwidth ratio of radar absorbers. *IEEE Transactions on Antennas and Propagation*, 48(8):1230–2134, August 2000.
- [83] R. M. Fano. Theoretical limitations on the broadband matching of arbitrary impedances. Technical Report 41, Research Laboratory of Electronics, MIT, January 1948.
- [84] Herbert J. Carlin and Pierre Amstutz. On optimum broad-band matching. *IEEE Transactions on Circuits and Systems*, 28(5):401–405, May 1981.
- [85] Alireza Kazemzadeh. Nonmagnetic ultrawideband absorber with optimal thickness. *IEEE Transactions on Antennas and Propagation*, 59(1):135–140, January 2011.
- [86] Robert J. Mailloux. *Phased Array Antenna Handbook*. Artech House, Boston/London, 1994.
- [87] A. S. Meier and W. P. Summers. Measured impedance of vertical antennas over finite ground planes. In *Proceedings of the IRE*, volume 67, pages 609–616, June 1949.

- [88] K. H. Awadalla and T. S. M. Maclean. Input impedance of a monopole antenna at the center of a finite ground plane. *IEEE Transactions on Antennas and Propagation*, 26(2):244–248, March 1978.
- [89] Saou-Wen Su, Kin-Lu Wong, Yuan-Tung Cheng, and Wen-Shyang Chen. Finite-ground-plane effects on the ultra-wideband planar monopole antenna. *Microwave and Optical Technology Letters*, 43(6):535–537, December 2004.
- [90] H. Nakano, S. Sasaki, H. Oyanagi, and J. Yamauchi. Cavity-backed Archimedean spiral antenna with strip absorber. *IET Microwaves, Antennas and Propagation*, 2(7):725–730, October 2008.
- [91] Ting-Yen Shih and Nader Behdad. A compact, broadband spiral antenna with unidirectional circularly polarized radiation patterns. *IEEE Transactions on Antennas and Propagation*, 63(6):2776–2781, June 2008.
- [92] Johnson J. H. Wang and Victor K. Tripp. Design of multioctave spiral-mode microstrip antennas. *IEEE Transactions on Antennas and Propagation*, 39(3):332–335, March 1991.
- [93] N. Rahman, A. Sharma, and M. N. Afsar. Characterization, design and optimization of low-profile cavities for UWB spiral antennas. *International Journal of Electromagnetics and Applications*, 2(3):16–23, 2012.
- [94] L. Shafai S. Noghianian. Control of microstrip antenna radiation characteristics by ground plane size and shape. In *IEE Proceedings - Microwaves, Antennas and Propagation*, volume 145, pages 207–212, June 1998.
- [95] Arun K. Bhattacharyya. Effects of finite ground plane on the radiation characteristics of a circular patch antenna. *IEEE Transactions on Antennas and Propagation*, 38(2):152–159, February 1990.

- [96] B. Stockbroeckx, I. Huynen, and A. Vander Vorst. Effect of surface wave diffraction on radiation pattern of slot antenna etched in finite ground plane. *Electronics Letters*, 36(17):1444–1446, August 2000.
- [97] Boyu Zheng and Zhongxiang Shen. Effect of a finite ground plane on microstrip-fed cavity-backed slot antennas. *IEEE Transactions on Antennas and Propagation*, 53(2):862–865, February 2005.
- [98] D. R. Jackson, J. T. Williams, Arun K. Bhattacharyya, Richard L. Smith, Stephen J. Buchheit, and S. A. Long. Microstrip patch designs that do not excite surface waves. *IEEE Transactions on Antennas and Propagation*, 41(8):1026–1037, August 1993.
- [99] Arun K. Bhattacharyya. Effects of ground plane and dielectric truncations on the efficiency of a printed structure. *IEEE Transactions on Antennas and Propagation*, 39(3):303–308, March 1994.
- [100] Li Du and Yunqi Fu. A small wideband low-multipath GNSS antenna using resistive film. *IEEE Antennas and Wireless Propagation Letters*, 12:1045–1048, February 2013.
- [101] R. G. Rojas, D. Colak, M. F. Otero, and W. D. Burnside. Synthesis of tapered resistive ground plane for a microstrip antenna. In *IEEE Antennas and Propagation Society International Symposium*, volume 2, pages 1224–1227, June 1995.
- [102] Patrick Vaudon, Thierry Aubreton, Philippe Dufrane, and Bernard Jecko. Influence of the ground plane structure on the radiation pattern of microstrip antennas. *Annales Des Télécommunications*, 48(5-6):319–329, 1993.
- [103] John Huang. The finite ground plane effect on the microstrip antenna

- radiation patterns. *IEEE Transactions on Antennas and Propagation*, 31(4):649–653, July 1983.
- [104] R. F. Miller. An approximate theory of the diffraction of an electromagnetic wave by an aperture in a plane screen. In *Proceedings of the IEE - Part C: Monographs*, volume 103, pages 177–185, March 1956.
- [105] G. S. Kirov. Design of short backfire antennas. *IEEE Antennas and Propagation Magazine*, 51(6):110–120, December 2009.
- [106] Hermann W. Ehrenspeck. The backfire antenna, a new type of directional line source. Technical Report ATC-238, Air Force Cambridge Research Laboratories, Bedford, MA, August 1961.
- [107] H. W. Ehrenspeck. The short-backfire antenna. In *Proceedings of the IEEE*, volume 53, pages 1138–1140, August 1965.
- [108] Shingo Ohmori, Shuichi Miura, Kiyonobu Kameyama, and Hiromitsu Yoshimura. An improvement in electrical characteristics of a short backfire antenna. *IEEE Transactions on Antennas and Propagation*, 31(4):644–646, July 1983.
- [109] Hisamatsu Nakano, Junji Yamauchi, and Horaki Mimaki. Backfire radiation from a monofilar helix with a small ground plane. *IEEE Transactions on Antennas and Propagation*, 36(10):1359–1364, October 1988.
- [110] H. Nakano, S. Sasaki, H. Oyanagi, and J. Yamauchi. Cavity-backed Archimedean spiral antenna with strip absorber. *IET Microwaves, Antennas and Propagation*, 2(7):725–730, October 2008.
- [111] A. R. Djordjević, A. G. Zajić, and M. M. Illić. Enhancing the gain of helical antennas by shaping the ground conductor. *IEEE Antennas and Wireless Propagation Letters*, 5:138–140, April 2006.

- [112] Min H. Hong, D. P. Nyquist, and K. M. Chen. Radiation fields of open-cavity radiators and a backfire antenna. *IEEE Transactions on Antennas and Propagation*, 18(6):813–815, November 1970.
- [113] K. S. Kelleher. Dipole antenna mounted in open-face resonant cavity. U.S. Patent 329 838, March 1966.
- [114] Hristos T. Anastassiou. A review of electromagnetic scattering analysis for inlets, cavities, and open ducts. *IEEE Antennas and Propagation magazine*, 40(6):27–40, December 2003.
- [115] Hao Ling, Ri-Chee Chou, and Shung-Wu Lee. Shooting and bouncing rays: calculating RCS of an arbitrarily shaped cavity. *IEEE Transactions on Antennas and Propagation*, 37(2):194–205, February 1989.
- [116] Hao Ling, Shung-Wu Lee, and Ri-Chee Chou. High-frequency RCS of open cavities with rectangular and circular cross sections. *IEEE Transactions on Antennas and Propagation*, 37(5):648–654, May 1989.
- [117] Prabhakar H. Pathak and Robert J. Burkholder. Modal, ray, and beam techniques for analyzing the EM scattering by open-ended waveguide cavities. *IEEE Transactions on antennas and Propagation*, 37(5):635–647, May 1989.
- [118] D. L. Moffatt, C.Y. Lai, and T. Lee. Time-domain electromagnetic scattering by open ended circular waveguide and related structure. *Wave Motion*, 6(4):363–387, July 1984.
- [119] Fei-Ran Yang, Kuang-Ping Ma, Yongxi Qian, and Tatsuo Itoh. A uniplanar compact photonic-bandgap (UC-PBG) structure and its applications for microwave circuits. *IEEE Transactions on Microwave Theory and Techniques*, 47(8):1509–1514, August 1999.

- [120] Pierre-Simon Kildal. Artificially soft and hard surfaces in electromagnetics. *IEEE Transactions on Antennas and Propagation*, 38(10):1537–1544, October 1990.
- [121] Hossein Sarbandi Farahani, Mehdi Veysi, Manouchehr Kamyab, and Alireza Tadjalli. Mutual coupling reduction in patch antenna arrays using a UC-EBG superstrate. *IEEE Antennas and Wireless Propagation Letters*, 9:57–59, February 2010.
- [122] Fan Yang and Yahya Rahmat-Samii. Microstrip antennas integrated with electromagnetic band-gap (EBG) structures: a low mutual coupling design for array applications. *IEEE Antennas and Wireless Propagation Letters*, 51(10):2936–2945, October 2003.
- [123] Zeev Iluz, Reuven Shavit, and Reuven Bauer. Microstrip antenna phased array with electromagnetic bandgap substrate. *IEEE Transactions Antennas and Propagation*, 52(6):1446–1453, June 2004.
- [124] Romulo F. Jimenez Broas, Daniel F. Sievenpiper, and Eli Yablonovitch. A high-impedance ground plane applied to a cellphone handset geometry. *IEEE Transactions on Microwave Theory and Techniques*, 49(7):1262–1265, July 2001.
- [125] Z. Ying and Pierre-Simon Kildal. Improvements of dipole, helix, spiral, microstrip patch and aperture antennas with ground planes by using corrugated soft surfaces. In *IEE Proceedings - Microwaves, Antennas and Propagation*, volume 143, pages 244–248, June 1996.
- [126] James C. Fletcher. Highly efficient antenna system using a corrugated horn and scanning hyperbolic reflector. U.S. Patent 3 949 404, April 1976.
- [127] Zhinong Ying, Per-Simon Kildal, and Ahmed A. Kishk. Study of different realizations and calculation models for soft surfaces by using a vertical

- monopole on a soft disk as a test bed. *IEEE Transactions on Antennas and Propagation*, 44(11):1474–1481, November 1996.
- [128] Akira Ishimaru. Backscattering enhancement: from radar cross sections to electron and light localizations to rough surface scattering. *IEEE Antennas and Propagation Magazine*, 33(5):7–11, October 1991.
- [129] Jérôme I. Glaser. Bistatic RCS of complex objects near forward scatter. *IEEE Transactions on Aerospace and Electronic Systems*, 21(1):70–78, January 1985.
- [130] Leslie R. Lemon. The radar “three-body scatter spike”: an operational large-hail signature. *American Meteorological Society*, 13(4):327–340, June 1998.
- [131] Roger M. Lhermitte. Observation of rain at vertical incidence with a 94 GHz doppler radar: an insight on Mie scattering. *Geophysical Research Letters*, 15(10):1125–1128, September 1988.
- [132] Raymond Wexler and David Atlas. Radar reflectivity and attenuation of rain. *Journal of Applied Meteorology*, 2(2):276–280, April 1963.
- [133] Xin Wang, Brian W. Pogue, Shudong Jiang, Xiaomei Song, Keith D. Paulsen, Christine Kogel, Steven P. Poplack, and Wendy A. Wells. Approximation of Mie scattering parameters in near-infrared tomography of normal breast tissue in vivo. *Journal of Biomedical Optics*, 10(5):051704–1–8, September 2005.
- [134] Iyad S. Saidi, Steven L. Jacques, and Frank K. Tittel. Mie and Rayleigh modeling of visible-light scattering in neonatal skin. *Applied Optics*, 34(31):7410–7418, November 1995.
- [135] Paul Bassan, Achim Kohler, Harald Martens, Joe Lee, Hugh J. Byrne, Paul Dumas, Michael Brown Ehsan Gazi, Noel Clarke, and Peter Gard-

- ner. Resonant Mie scattering (RMieS) correction of infrared spectra from highly scattering biological samples. *Analyst*, 135(2):268–277, February 2010.
- [136] Susie Eustis and Mostafa A. El-Sayed. Why gold nanoparticles are more precious than pretty gold: noble metal surface plasmon resonance and its enhancement of the radiative and nonradiative properties of nanocrystals of different shapes. *Chemical Society Reviews*, 35(3):268–277, 2006.
- [137] C. C. Lam, P. T. Leung, and K. Young. Explicit asymptotic formulas for the positions, widths, and strengths of resonances in Mie scattering. *Journal of the Optical Society of America B*, 9(9):1585–1592, September 1992.
- [138] Robert Paknys and Nan Wang. Creeping wave propagation constants and modal impedance for a dielectric coated cylinder. *IEEE Transactions on Antennas and Propagation*, 34(5):674–680, May 1986.
- [139] G. C. Gaunaurd, H. Überall, and A. Nagl. Complex-frequency poles and creeping-wave transients in electromagnetic-wave scattering. *Proceedings of the IEEE*, 71(1):172–174, January 1983.
- [140] Arnold Sommerfeld. Trans. Raymond J. Nagem, Mario Zampolli, and Guido Sandri. *Mathematical Theory of Diffraction*, volume 35 of *Progress in Mathematical Physics*. Birkhäuser, Boston, 2004 (1896).
- [141] Salvatore Ganci. Analytical and experimental remarks on the Sommerfeld’s half plane solution. *Optik - International Journal for Light and Electron Optics*, 121(11):993–996, June 2010.
- [142] Joseph B. Keller. Geometrical theory of diffraction. *Journal of the Optical Society of America*, 52(2):116–130, February 1962.

- [143] Prabhakar H. Pathak, Giorgio Carluccio, and Matteo Albani. The uniform geometrical theory of diffraction and some of its applications. *IEEE Antennas and Propagation Magazine*, 55(4):41–68, August 2013.
- [144] U. Peter Svensson, Roger I. Fred, and John Vanterkooy. An analytic secondary source model of edge diffraction impulse responses. *The Journal of the Acoustical Society of America*, 106(5):2331–2344, November 1999.
- [145] Daniel B. Hodge. Spectral and transient response of a circular disk to plane electromagnetics. *IEEE Transactions on Antennas and Propagation*, 19(4):558–561, July 1997.
- [146] Herman Medwin, Emily Childs, and Gary M. Jebsen. Impulse studies of double diffraction: a discrete Huygens interpretation. *The Journal of the Acoustical Society of America*, 72(3):1005–1013, September 1982.
- [147] F. J. García-Vilda, Esteban Moreno, J. A. Porto, and L. Martín-Moreno. Transmission of light through a single rectangular hole. *Physical Review Letters*, 95(10):103901–1–4, September 2005.
- [148] A. Roberts. Electromagnetic theory of diffraction by a circular aperture in a thick, perfectly conducting screen. *Journal of the Optical Society of America A*, 4(10):1970–1983, October 1987.
- [149] Francisco Medina, Francisco Mesa, and Ricardo Marqués. Extraordinary transmission through arrays of electrically small holes from a circuit theory perspective. *IEEE Transactions on Microwave Theory and Techniques*, 56(12):3108–3120, December 2008.
- [150] J. F. Kaiser. Digital filters. In F. F. Kuo and J. F. Kaiser, editors, *System Analysis by Digital Computer*, pages 218–285. Wiley, New York, 1966.
- [151] Nezh C. Geçkinli and Davras Yavuz. Some novel windows and a concise

- tutorial comparison of window families. *IEEE Transactions on Acoustics, Speech, and Signal Processing*, 26(6):501–507, December 1978.
- [152] James R. Wait. Excitation of surface waves on conducting, stratified, dielectric-clad, and corrugated surfaces. *Journal of Research of the National Bureau of Standards*, 59(6):365–377, December 1957.
- [153] H. M. Barlow. Surface waves. In *Proceedings of the IEE - Part III: Radio and Communication Engineering*, volume 100, pages 329–341, November 1953.
- [154] K. A. Michalski and J. R. Mosig. The Sommerfeld half-space problem revisited: from radio frequencies and Zenneck waves to visible light and Fano modes. *Journal of Electromagnetic Waves and Applications*, 30(1):1–42, December 2016.
- [155] C. C. Cutler. Genesis of the corrugated electromagnetic surface. In *Proceedings of IEEE Antennas and Propagation Society International Symposium and URSI National Radio Science Meeting*, volume 3, pages 1456–1459, June 1994.
- [156] B. Friedman and W. Elwyn Williams. Excitation of surface waves. In *Proceedings of the IEE - Part C: Monographs*, volume 105, pages 252–258, March 1958.
- [157] R. A. Hurd. The propagation of an electromagnetic wave along an infinite corrugated surface. *Canadian Journal of Physics*, 32(12):727–734, December 1954.
- [158] R. Elliot. On the theory of corrugated plane surfaces. *Transactions of the IRE Professional Group on Antennas and Propagation*, 2(2):71–81, April 1954.

- [159] J. C. Simon and G. Weill. A new type of endfire antenna. *Annales de Radioélectricité*, 8:183, 1953.
- [160] D. M. Schuster and D. L. Nixon. Parabolic reflector horn feed with spillover correction. U.S. Patent 3 212 096, October 1965.
- [161] R. F. Thomas and D. A. Bathker. A dual hybrid mode feedhorn for DSN antenna performance enhancement. The Deep Space Network Progress Report 42-22, June 1974.
- [162] J. Tranquilla, J. Carr, and H. Al-Rizzo. Analysis of a choke ring ground-plane for multipath control in Global Positioning System (GPS) applications. *IEEE Transactions on Antennas and Propagation*, 42(7):905–911, July 1994.
- [163] William L. Barnes and Alain Dereux. Surface plasmon subwavelength optics. *Nature*, 424:824–830, 2003.
- [164] H. M. Barlow and J. Brown. *Radio Surface Waves*. Oxford University Press, London, 1962.
- [165] David Lamensdorf and Leon Susman. Design and modeling of spoof surface plasmon modes-based microwave slow-wave transmission line. *IEEE Transactions on Microwave Theory and Techniques*, 63(6):1817–1825, June 2015.
- [166] Jian-Ming Jin. *Theory and computation of electromagnetic fields*. Wiley, Hoboken, New Jersey, 2010.
- [167] A. Ishimaru, J. D. Rockway, and Seong-Woo Lee. Sommerfeld and Zenneck wave propagation for a finitely conducting one-dimensional rough surface. *IEEE Transactions on Antennas and Propagation*, 48(9):1475–1484, September 2000.

- [168] V. N. Datsko and A. A. Kopylov. On surface electromagnetic waves. *Physics-Uspokhi*, 51(1):101–102, 2008.
- [169] Waldemar Kunysz. A three dimensional choke ring ground plane antenna. URL https://www.novatel.com/assets/Documents/Papers/3D_choke_ring.pdf.
- [170] J. Ashjaee, V. S. Filippov, D. V. Tatarnikov, A. V. Astakhov, and I. V. Sutjagin. Dual-frequency choke-ring ground planes. U.S. Patent 6 278 407 B1, August 2001.
- [171] A.-M. Dinius. GPS antenna multipath rejection performance. Technical Report ATC-238, Lincoln Laboratory, Lexington, MA, August 1995.
- [172] David M. Pozar. *Microwave Engineering*. Wiley, Danvers, MA, 2012.
- [173] K. Shlager, G. Smith, and J. Maloney. Optimization of bow-tie antennas for pulse radiation. *IEEE Transactions on Antennas and Propagation*, 42(7):975–982, July 1994.
- [174] B. Lampe and K. Holliger. Resistively loaded antennas for ground-penetrating radar: a modeling approach. *Geophysics*, 70(3):K23–K32, May 2005.
- [175] S. N. Samaddar and E. L. Mokole. Some basic properties of antennas associated with ultrawideband radiation. In Carl E. Baum, Lawrence Carin, and Alexander P. Stone, editors, *Ultra-wideband, Short-Pulse Electromagnetics 3*, pages 147–164. Springer, Boston, MA, 1997.
- [176] David Lamensdorf and Leon Susman. Baseband-pulse-antenna techniques. *IEEE Antennas and Propagation Magazine*, 36(1):20–30, February 1994.

- [177] James S. McLean, Heinrich Foltz, and Robert Sutton. Pattern descriptors for UWB antennas. *IEEE Transactions on Antennas and Propagation*, 53(1):553–559, January 2005.
- [178] Andreas F. Molisch. Ultrawideband propagation channels—theory, measurement, and modeling. *IEEE Transactions on Vehicular Technology*, 54(5):1528–1545, September 2005.
- [179] B. Scheers, M. Acheroy, and A. Vander Vorst. Time-domain simulation and characterisation of TEM horns using a normalized impulse response. In *IEE Proceedings - Microwaves, Antennas and Propagation*, volume 147, pages 463–468, December 2000.
- [180] Werner Sörgel and Werner Wiesbeck. Influence of the antennas on the ultra-wideband transmission. *EURASIP Journal on Advances in Signal Processing*, 3:296–305, December 2005.
- [181] Xianming Qing and Zhi Ning Chen. Transfer functions measurement for UWB antenna. In *IEEE Antennas and Propagation Society Symposium, 2004*, pages 2532–2535, June 2004.
- [182] James S. McLean, Robert Sutton, Armando Medina, Heinrich Foltz, and Junfei Li. The experimental characterization of UWB antennas via frequency-domain measurements. *IEEE Antennas and Propagation Magazine*, 49(6):192–202, December 2007.
- [183] Karl F. Warnick. Characterizing antennas in the time and frequency domains. *IEEE Antennas and Propagation Magazine*, 60(1):106–110, February 2018.
- [184] Yi-Wen Liu. Hilbert transform and applications. In Salih Mohammed Salih, editor, *Fourier Transform Applications*, pages 291–300. IntechOpen, 2012.

- [185] Steven W. Smith. *The Scientist and Engineer's Guide to Digital Signal Processing*. California Technical Publishing, San Diego, second edition, 1999.